Nanomanufacturing
University of Michigan
ME599-002 | Winter 2010

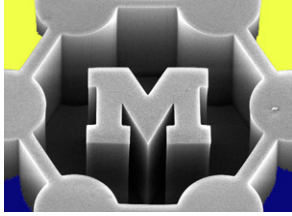

21: **Organization and properties of nanostructure networks**

April 12, 2010

John Hart
ajohnh@umich.edu
http://www.umich.edu/~ajohnh

Announcements

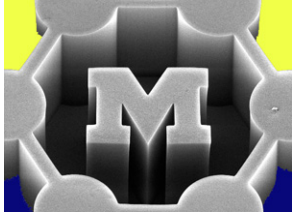

- Project meetings Thursday, please sign up
- Project presentations next M, 6-9pm, 165 CC
- Project reports due Tues (Apr/20) 5pm; may be submitted as late as Fri (Apr/**23**) without penalty
- GCC review late next week?

Configurations

Order = quality, purity, alignment
Quantity = #/volume

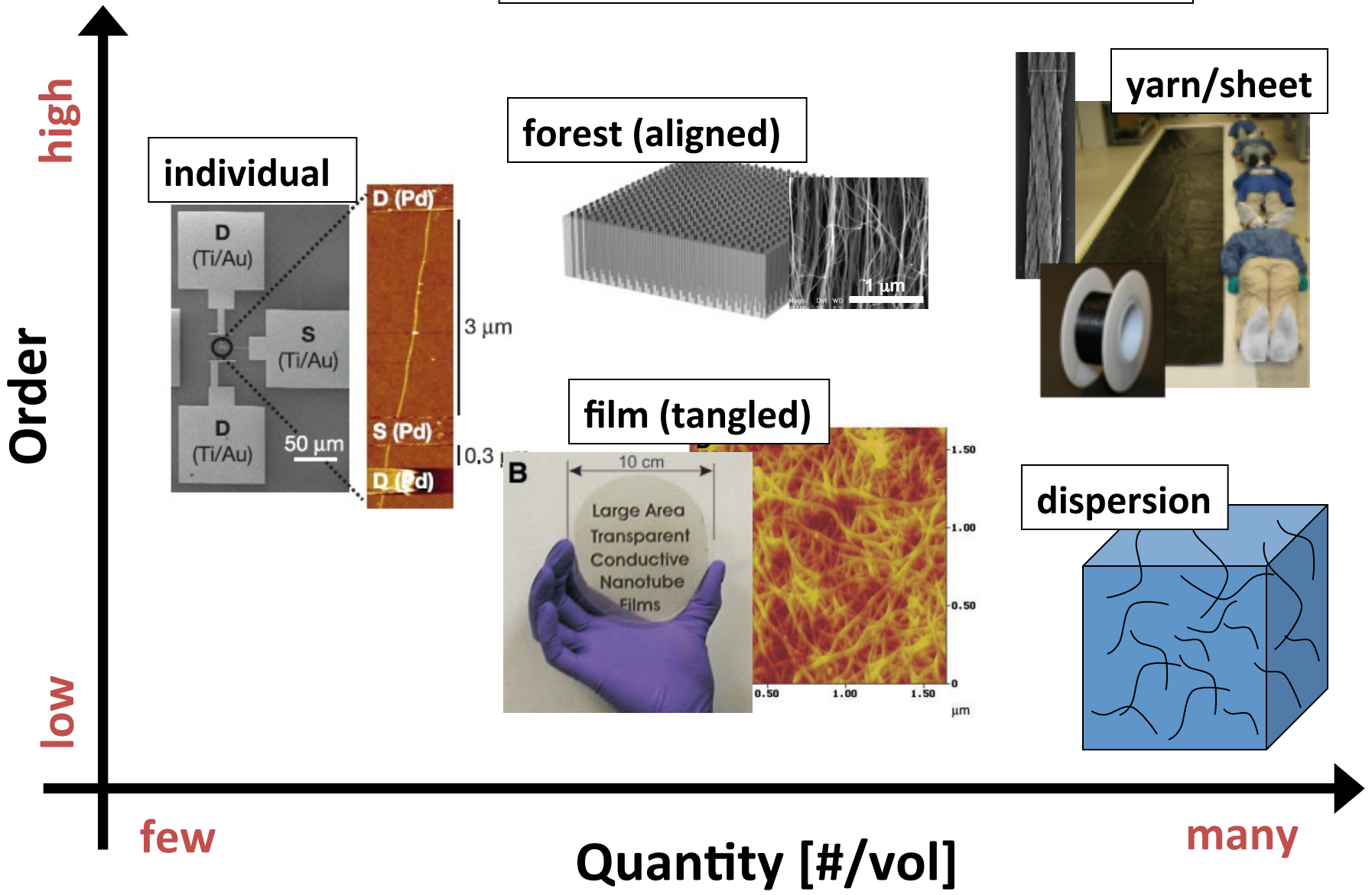

Images from many sources including Nanocomp, Dai, Kim, Rinzler groups

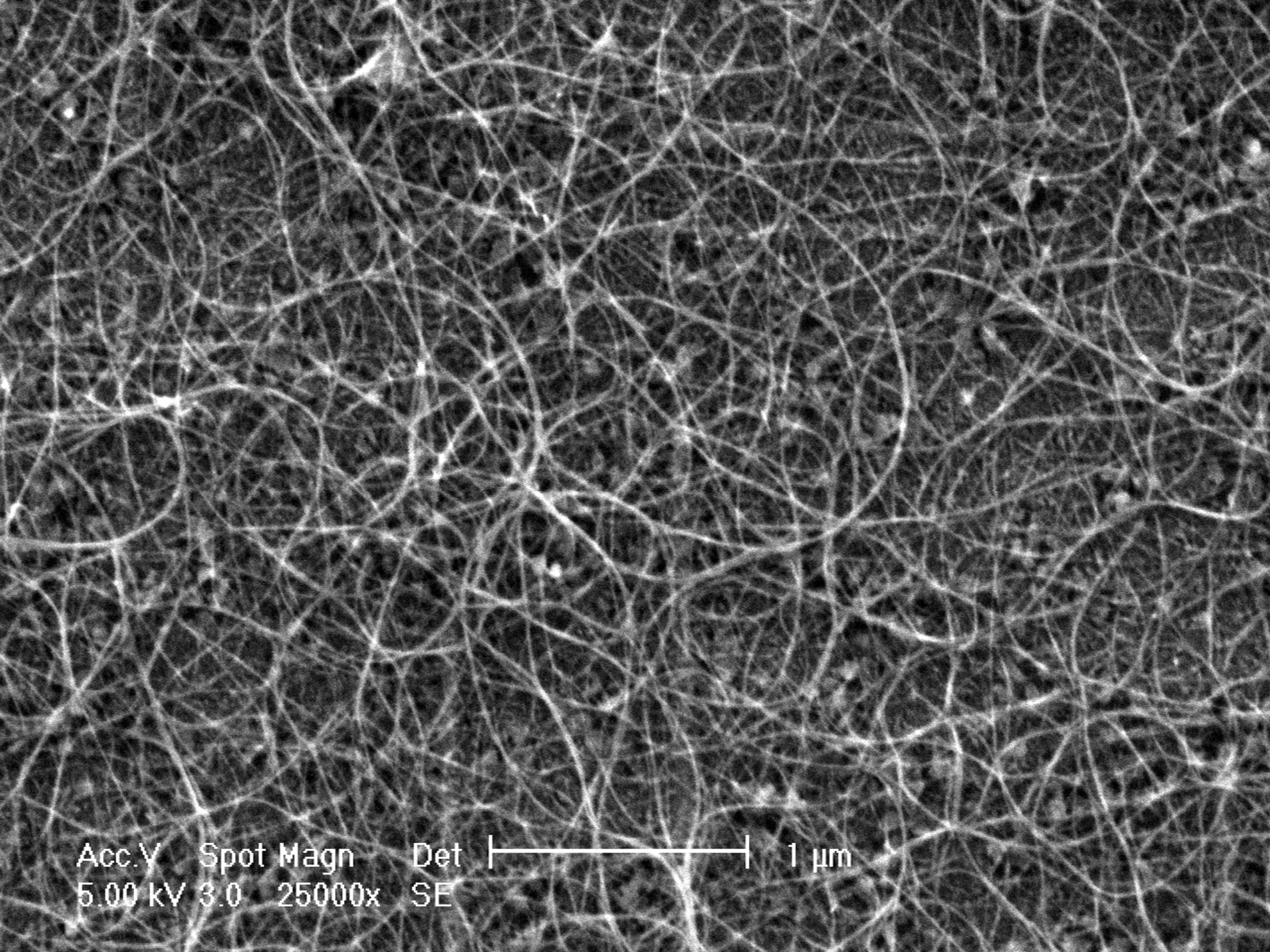
Acc.V Spot Magn Det
5.00 kV 3.0 25000x SE
1 µm

Today's agenda

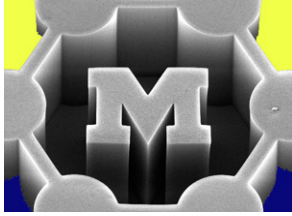

- Nanostructure networks: concepts and dominant behavior
- Electrical transport: percolation theory
- Thermal transport in networks
- Mechanical properties of networks
- Methods of joining nanostructures

Today's readings

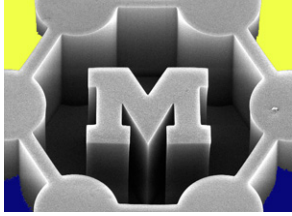

OPTIONAL: (ctools)

Electrical

- Balberg, "Critical behavior of the two-dimensional sticks system"
- Kumar et al., "Percolating conduction in finite nanotube networks"

Thermal

- Prasher et al., "Turning carbon nanotubes from exceptional heat conductors into insulators"

Mechanical

- Berhan et al., "Mechanical propertis of nanotube sheets"
- Koziol et al., "High performance carbon nanotube fiber"

Today's readings

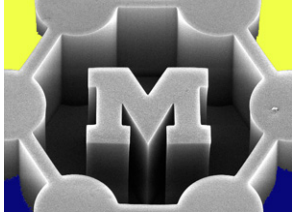

OPTIONAL: (ctools)

Joining

- Krasheninnikov and Barnhart, "Engineering of nanostructured carbon materials with electron or ion beams"
- Manzo et al., "Heterojunctions between metals and carbon nanotubes as ultimate nanocontacts"

Networks of nanostructures

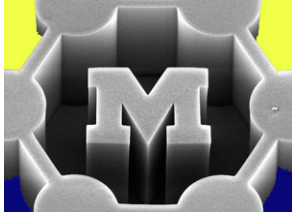

GOAL:

Achieve properties of individual nanostructures at large (bulk) scales, by assembling the structures into a 2D or 3D network

AND/OR

achieve *combined* properties of different types of nanostructures and host materials by making a network

Practically, network performance is dominated by:

- Network architecture and morphology (alignment and interconnection)
- Geometry (shape) of the individual nanostructures
- Intrinsic properties of the individual nanostructures (e.g., defect density)
- **Structure-structure interactions (contact resistance)**
- Structure-matrix interactions (functionalization, bonding)

→ *the complexity of a network also complicates characterization*

Applications of nanostructure networks

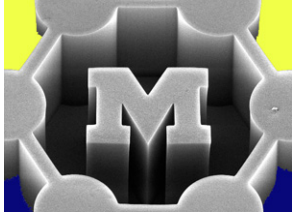

- Conductive plastics for electrostatic discharge/shielding
  - vehicle interiors
  - E/M shielding
- Thin-film electronics
  - memory
  - flexible transistors
  - transparent conducting films
- Strain sensors and chemical sensors (resistive or capacitive)
- Energy conversion and storage devices
  - battery and fuel cell electrodes
  - catalyst supports
- Electrical/mechanical/thermal interfaces

Electrical properties of networks

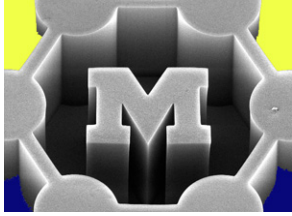

Percolation at low loadings gives large increase in electrical conductivity

- Typically 0.1-1% percolation threshold for high-aspect-ratio structures
- Large conductivity difference between filler and matrix, meaning electron transport is almost entirely through the filler, e.g., $>10^{11}$ conductivity ratio for CNTs/polymer

Thermal properties of networks

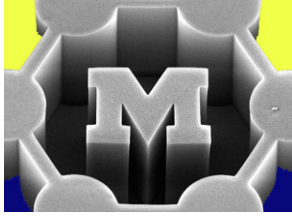

- No sharp transition at percolation
- Phonon scattering at structure-structure contacts dominate thermal transport
- Structure-matrix interactions can also significantly affect conductivity by phonon scattering

Mechanical properties of networks

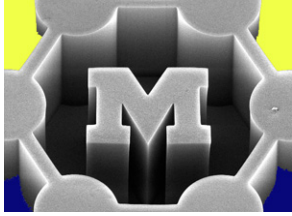

- Largely follow a linear rule of mixtures
- Stiffness can scale to near-theoretical values
- Strength governed by defect isolation and propagation
- Overlap/joining between structures (shear strength) vital for load transfer, especially between strong structures and a weak matrix
- Alignment (waviness) is critical
- Joint morphology is critical

What types of joints are in this network?

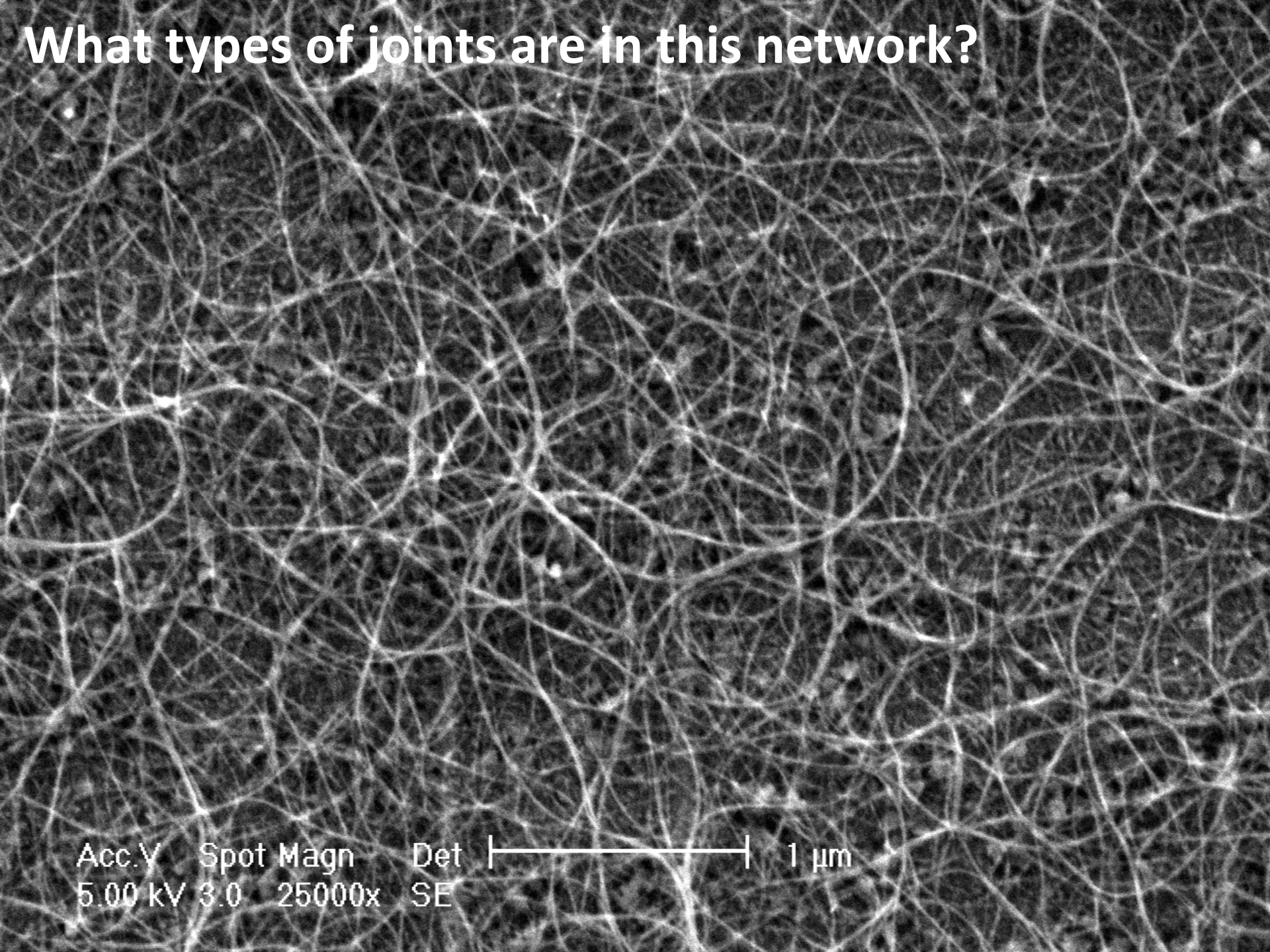

Joints: an intrinsic attribute of a network

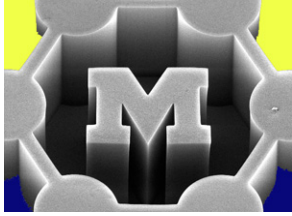

Entangled (VDW contact)

(a)

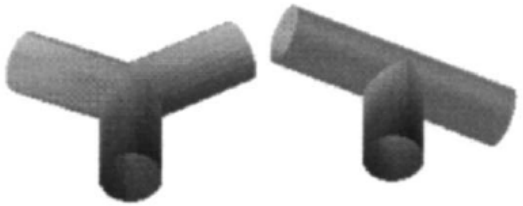

(b)

Branched (as-grown)

Welded (irradiated)

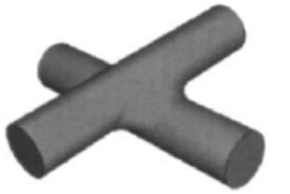

(c)

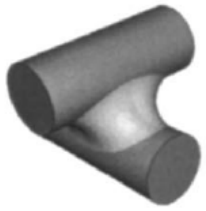

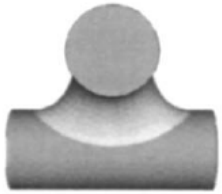

(d)

"Soldered" (deposited)

Coated (e.g., metal or polymer)

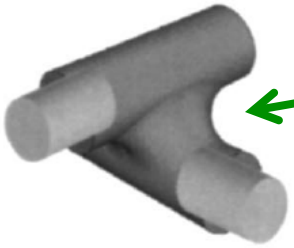

Interface region

(e)

Types of contact

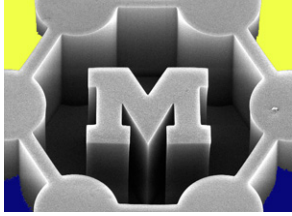

Non-bonding: van der Waals adhesion

- contact
- thin interlayer (e.g, polymer, functional group)

Bonding: covalent linkages

- contact
- thin interlayer (e.g., polymer, functional group)

Relevant separation distances

Electrical: 0 to ~10 nm

- tunneling

Thermal: 0 to ~1 nm

- phonon propagation

Mechanical: contact only

- direct load transmission

Network deposition methods

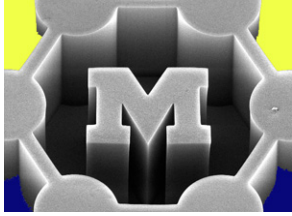

- Direct growth (e.g., CVD) on a substrate

- Dispersion (and purification, separation) then deposition on a substrate by, e.g.,
  - Spin-coating
  - Dip-coating
  - Vacuum filtration
  - Electrophoretic deposition
  - Transfer (e.g., contact printing)
  - Bulk mixing (e.g., polymer composites)

CNT films: tangled vs. aligned

(1) $Mo/Fe/Al_2O_3$ in CH_4/H_2, 875 °C

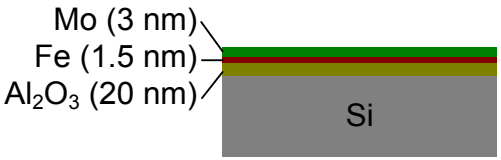

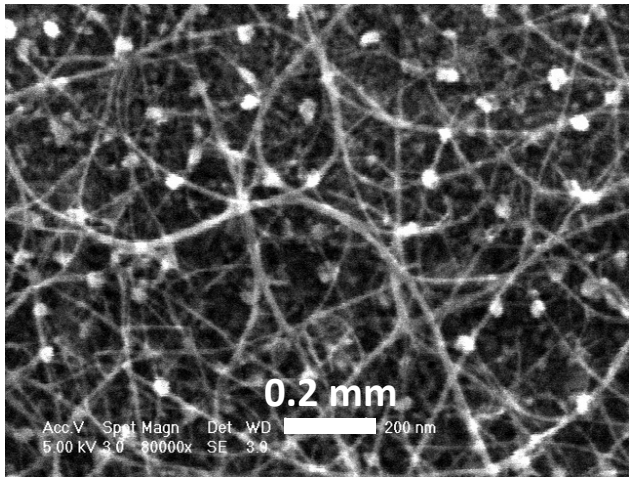

SWNT selectivity

Mo mediates CH_4 decomposition to give SWNTs

Fewer active catalyst particles
Low activity carbon source

(2) Fe/Al_2O_3 in C_2H_4/H_2, 750 °C

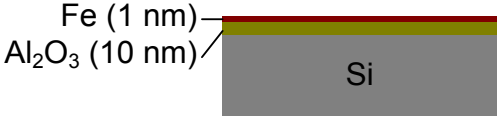

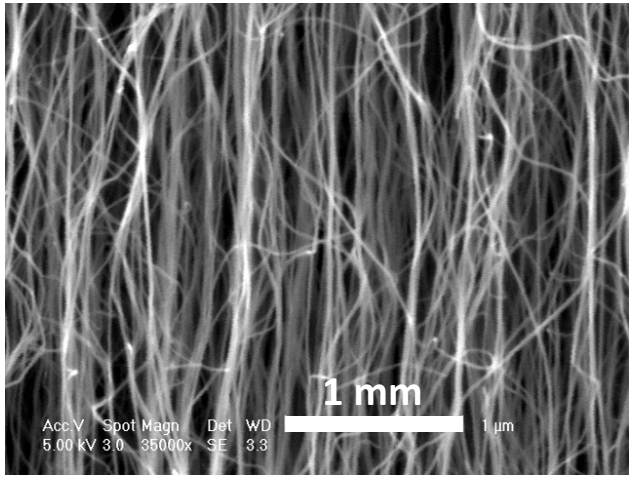

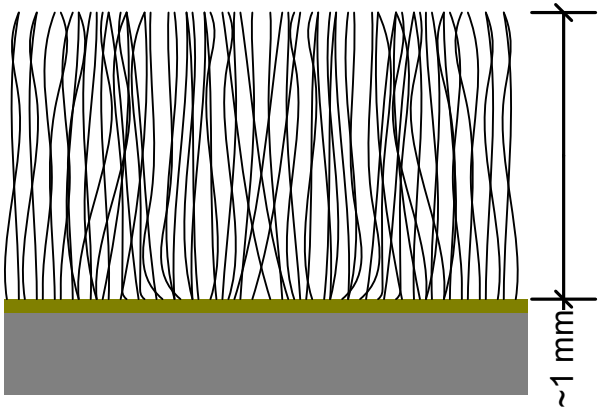

More active catalyst particles
High activity carbon source

Hart, Slocum, Royer, *Carbon* 44:348-59, 2006.

Vacuum filtration

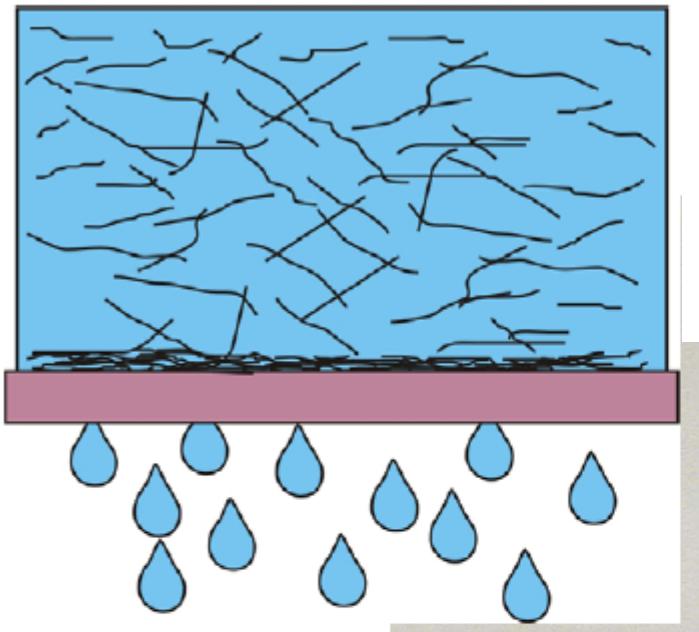

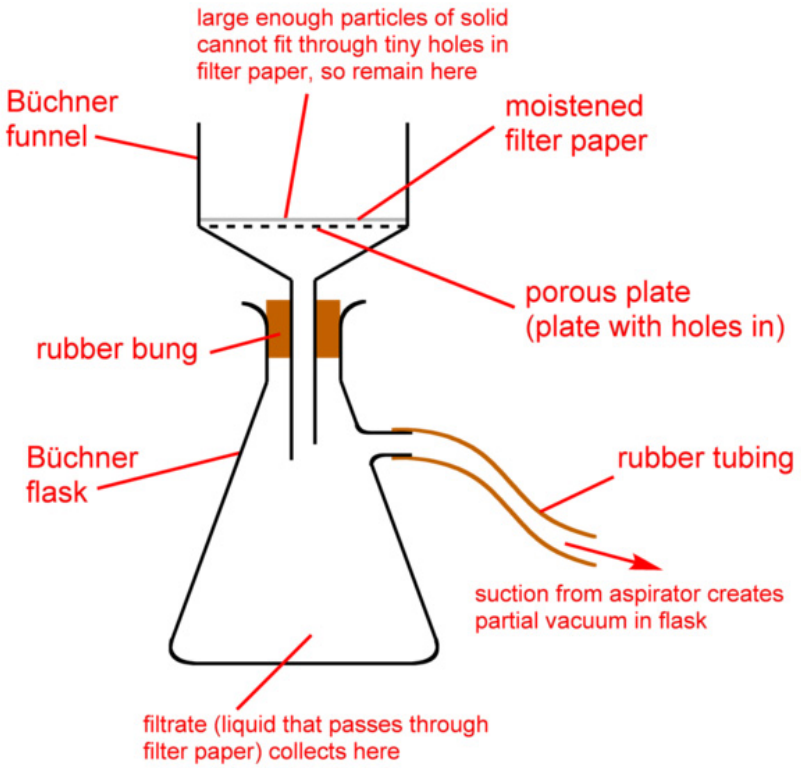

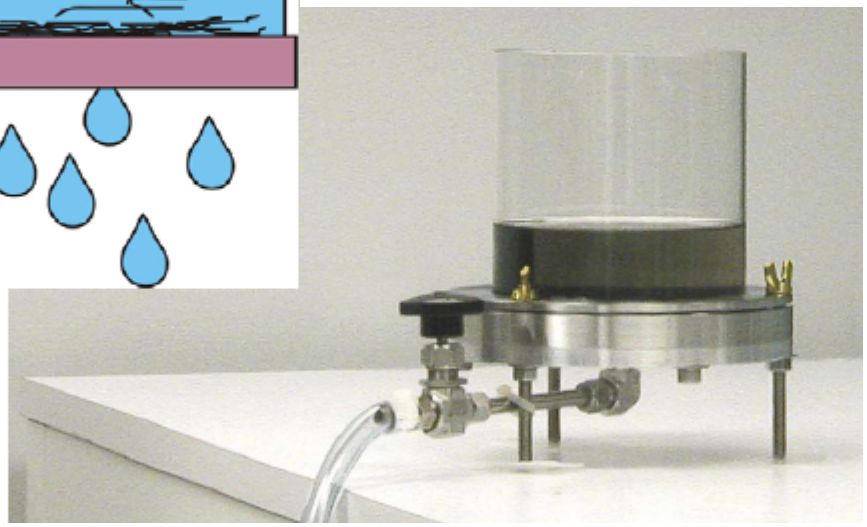

Vacuum-filtered CNT films at different densities

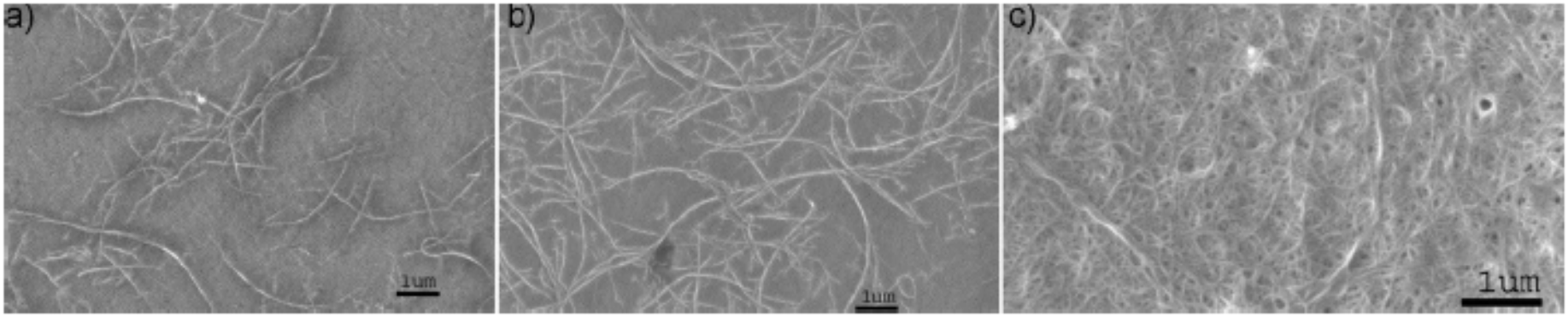

Figure 1. SEM images of the NTNs on alumina substrates, taken at 1.5 kV and 5 μA emission current. (a) Network resulting from filtering 7 mL of NT solution through the membrane. The filter pores are not visible in the scale shown. The network is near the percolation threshold and has few or no percolative paths through the sample. (b) 10 mL of NT solution for this sample. The network is above the percolation threshold and has several parallel pathways, allowing conduction across the film. (c) Film resulting from 400 mL of solution. Film is several layers thick.

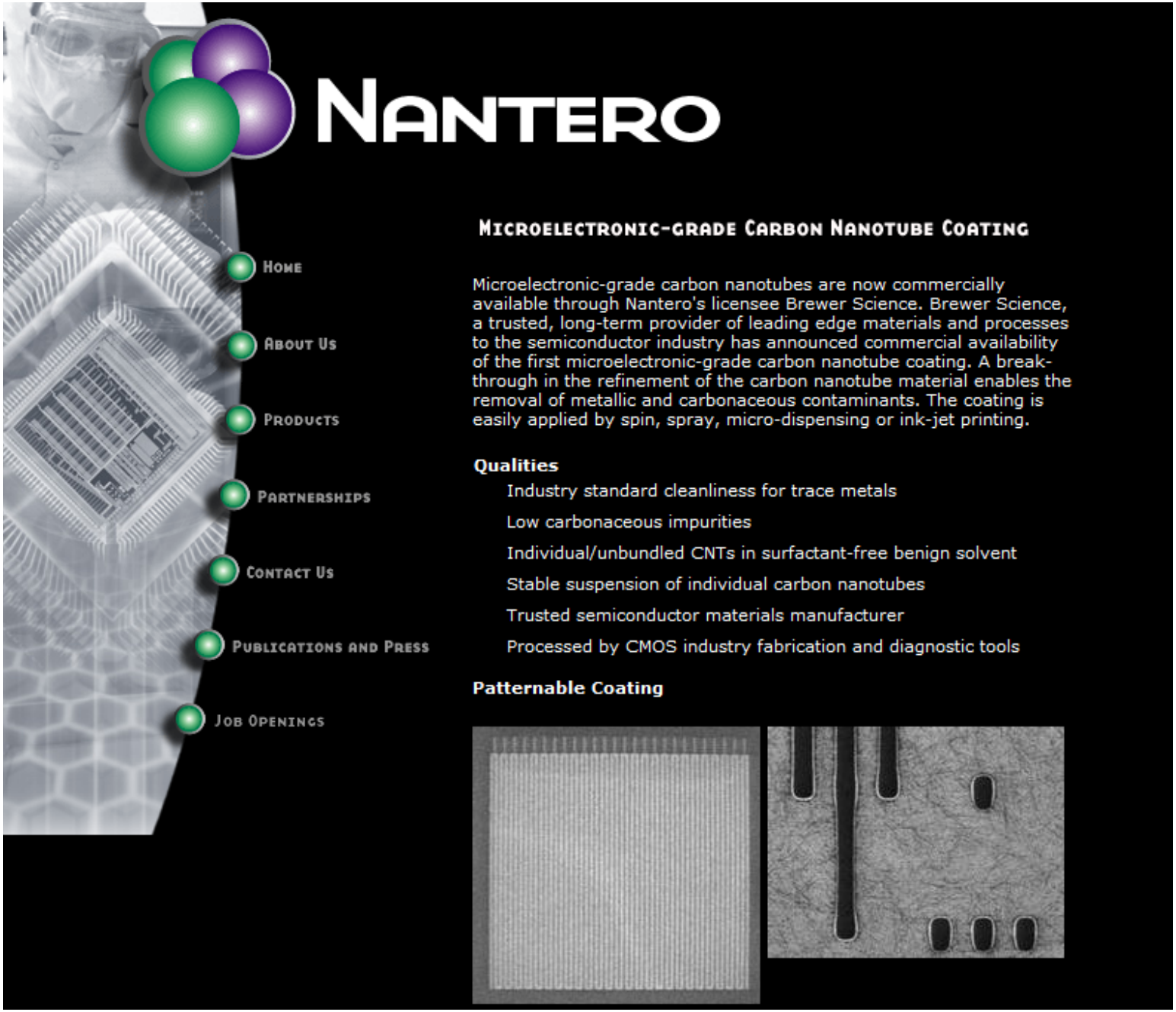

http://www.nantero.com

Anisotropic networks

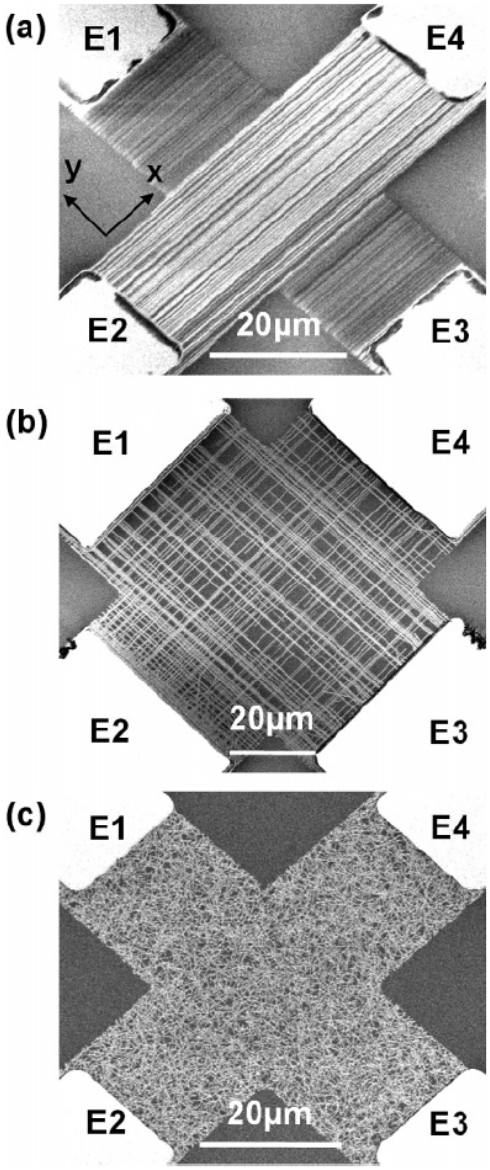

gure 6. SEMs of four terminal test structures formed on SWNTs ith different layouts, including (a) aligned arrays, (b) crossbars, id (c) random networks.

SWNTs (transfer printed)

Ag NWs (Langmuir-Blodgett method)

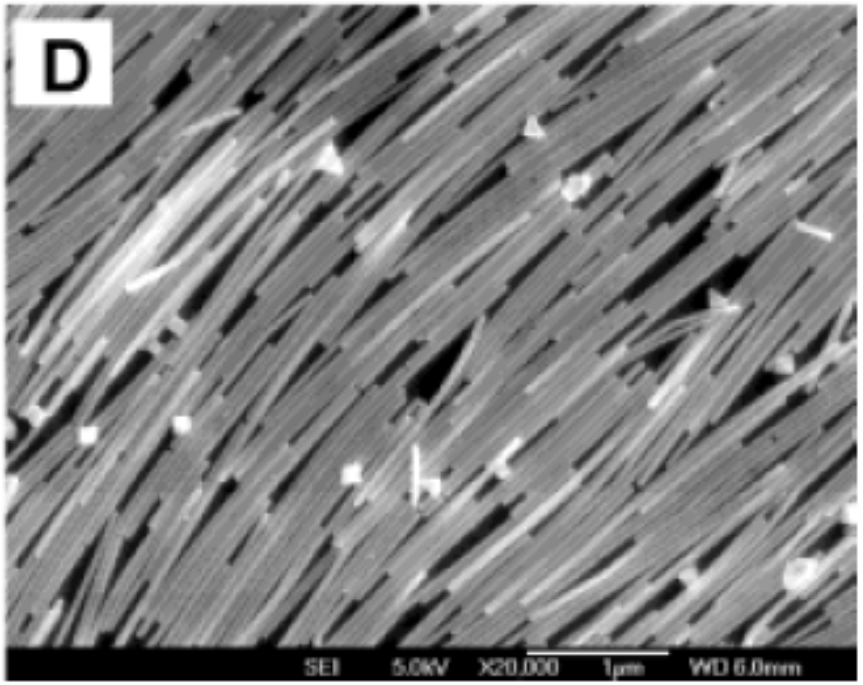

Configuration matters

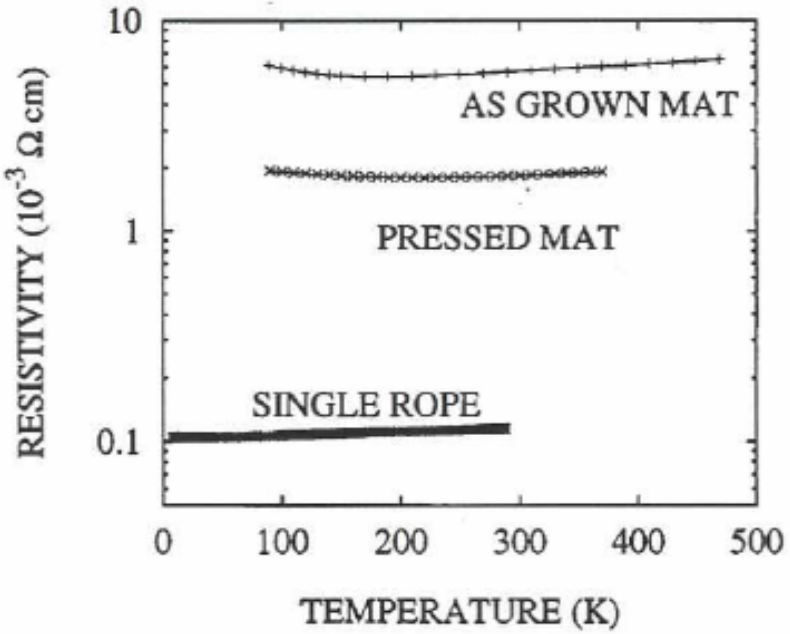

A single uniaxial rope is ~ 60 X more conductive than the disordered mat.
The compressed mat is ~3X densified.
For all three materials ρ(T) is quite flat.

R. S. Lee *et al*, Phys. Rev. B **55**, R4921 (1997)

Geometry determines transport pathway(s) (electrons, phonons, forces)

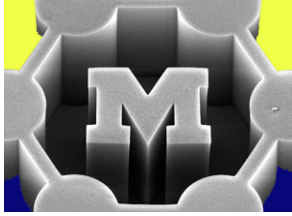

Square lattice

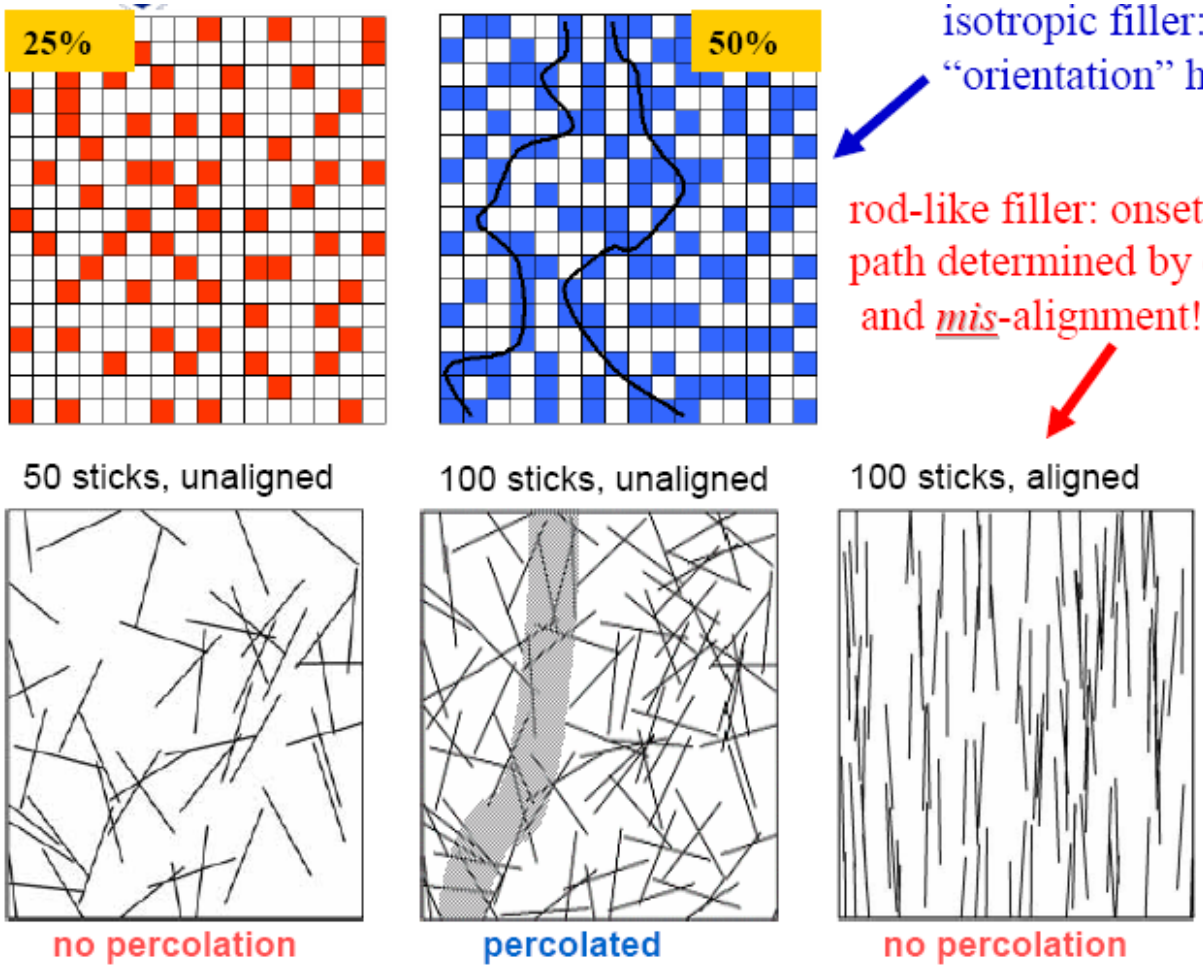

F. Du *et al.*, *Phys. Rev.B* **72**, 121404R (2005

Stick count → density; 1D concept introduces cluster size

Imaging network connectivity

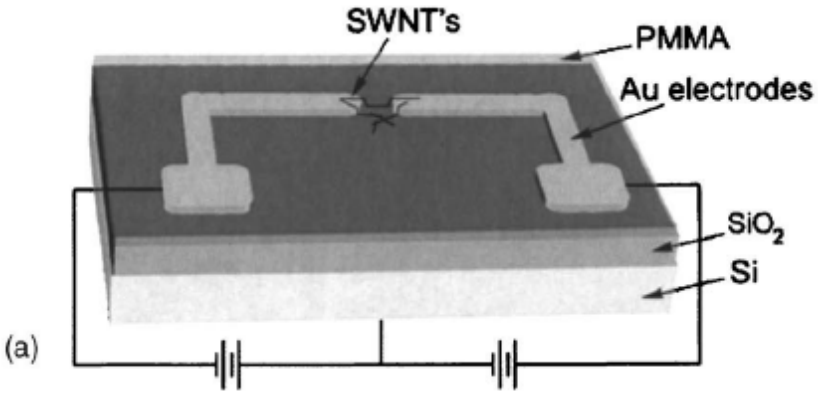

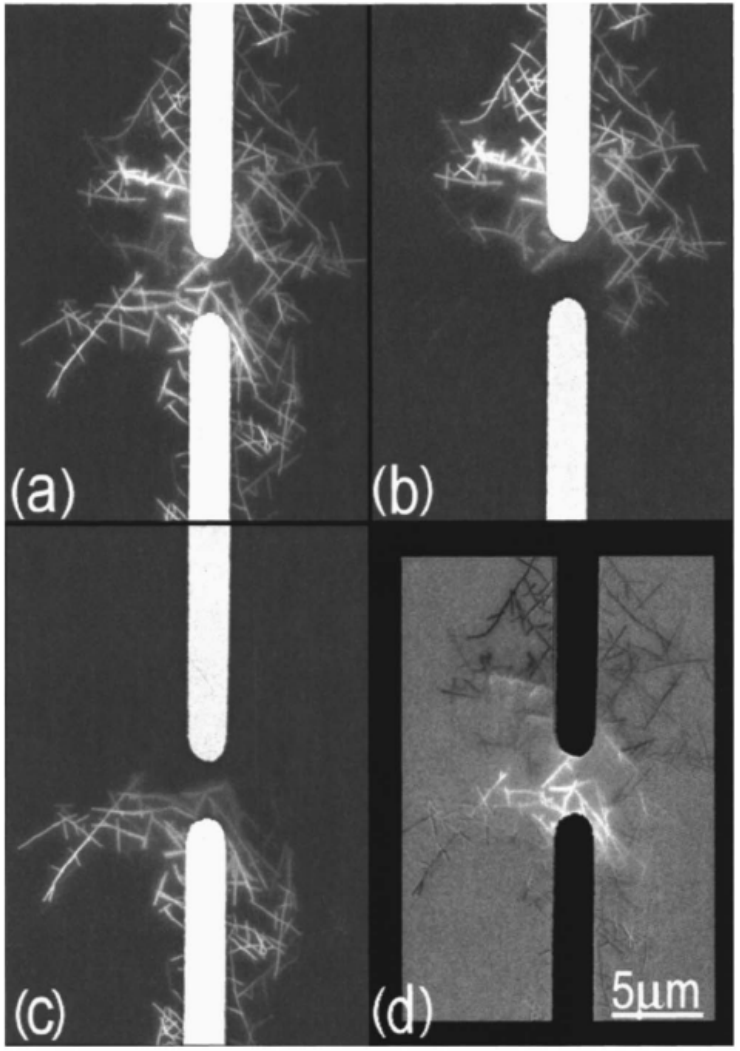

FIG. 2. A series of voltage contrast SEM micrographs under various bias conditions: (a) both electrodes at −20 V, (b) top electrode at −20 V, bottom electrode at ground, and (c) top electrode at ground, bottom electrode at −20 V. (d) Image generated by subtracting (b) and (c) from (a).

Jesse et al., *Appl Phys Lett* 89:013114, 2006.

Percolation threshold

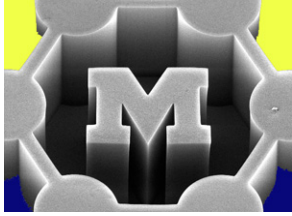

The density (volume fraction) of filler above which there is a continuous path across a material

- Typically 0.1-1% for "long" (fiber/wire) conductors
- Typically 1-10% for agglomerates/disk

Percolation is a random process…

Percolation is a sudden transition!

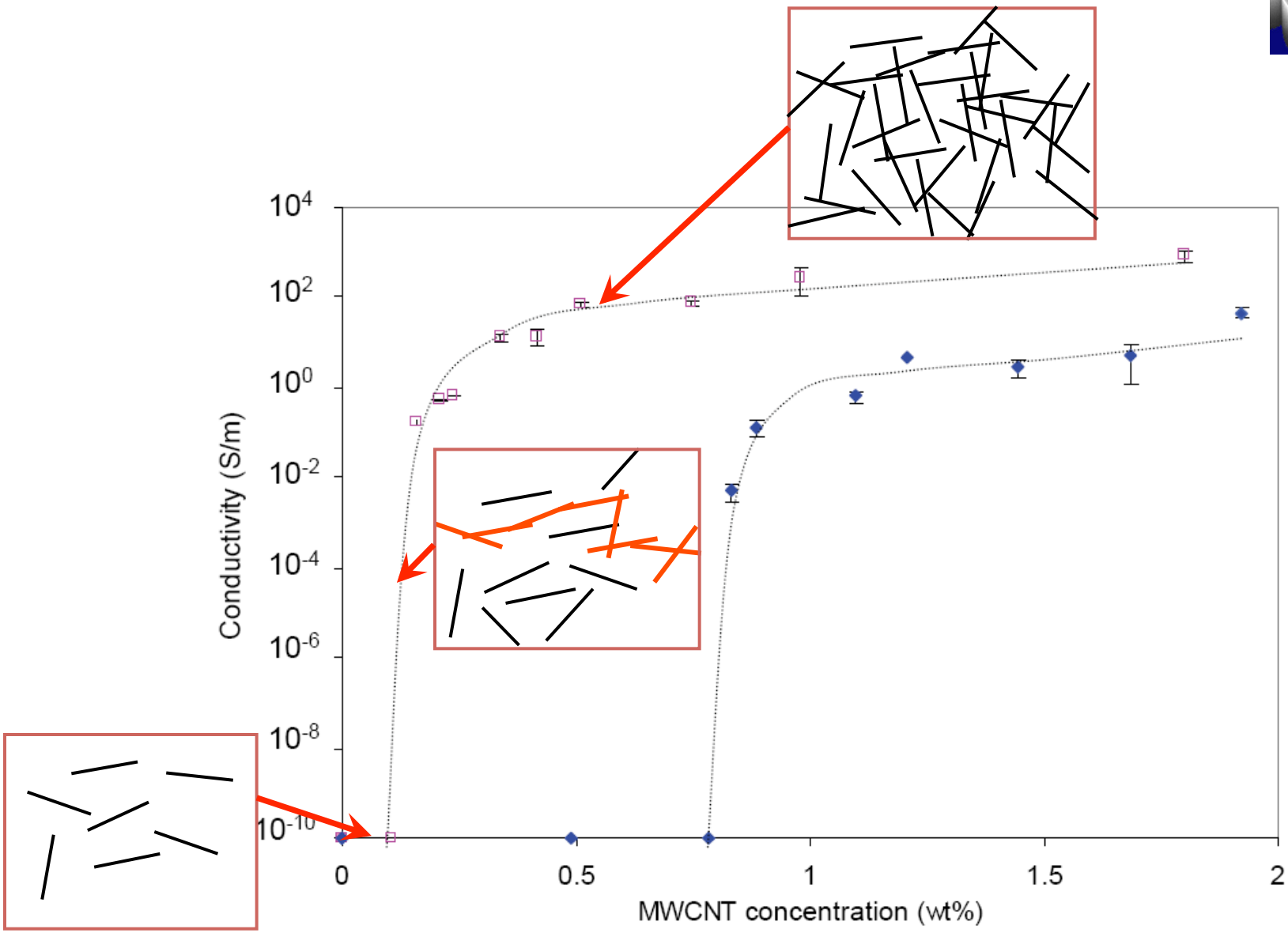

N. Grossiord et al, TU/Eindhoven.

A general network conductivity (diffusivity) model (above percolation threshold)

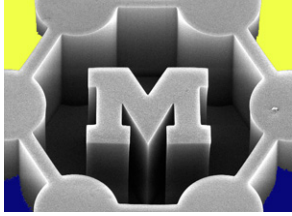

$$\sigma = \sigma_{\max}\left(\rho - \rho_c\right)^t$$

For a "perfect" 3D network (lattice), *t* = 2

Practically, *t* varies a lot (*t*< 2) based on

- Geometry and morphology of conductors (e.g., CNTs)
- Electron hopping between conductors (across gaps)
- Network is often locally agglomerated

Resistor network model

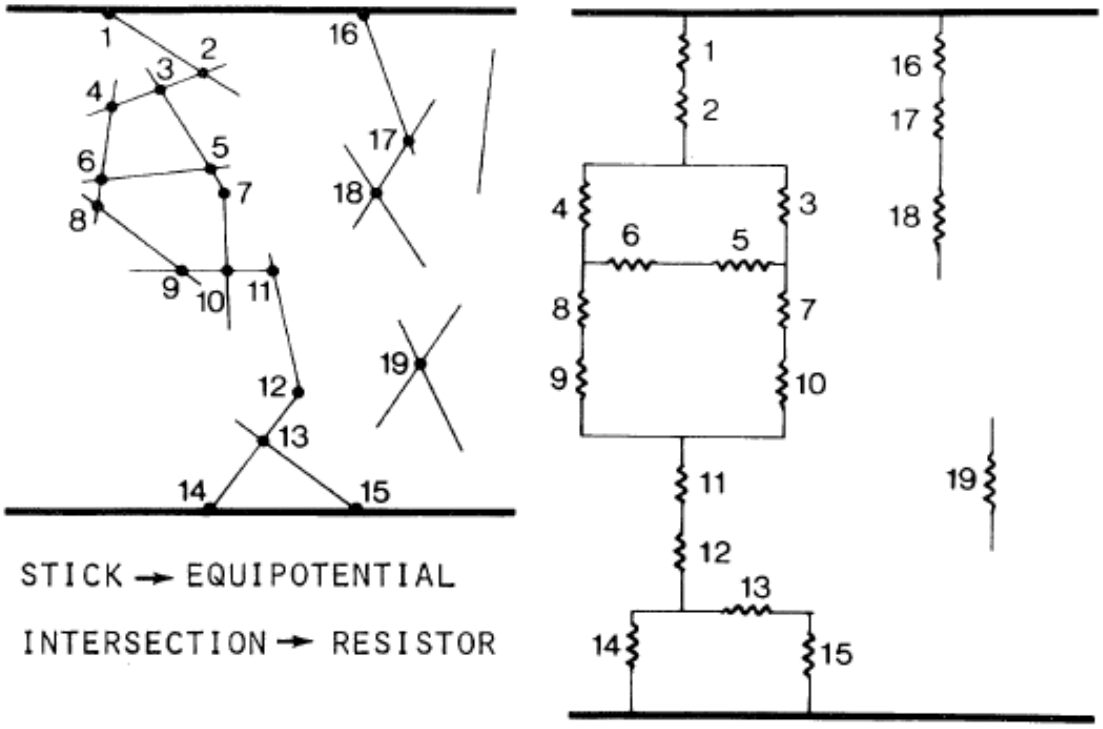

FIG. 1. The transformation of a conducting-sticks system into a resistor network. The sticks are assumed to be conducting and a resistor is assumed to be associated with the intersection of two sticks. Note that the equipotential stick is reduced to a point or a junction in the resistor network.

Balberg et al., *Physical Review Letters* 51(18):1605, 1983.

"Composite" transistor shows size effects and network effects

- Narrow = ballistic
- Wide = diffusive

- Junction resistances ~1000's of ohms (tunneling, M/M, M/SC)

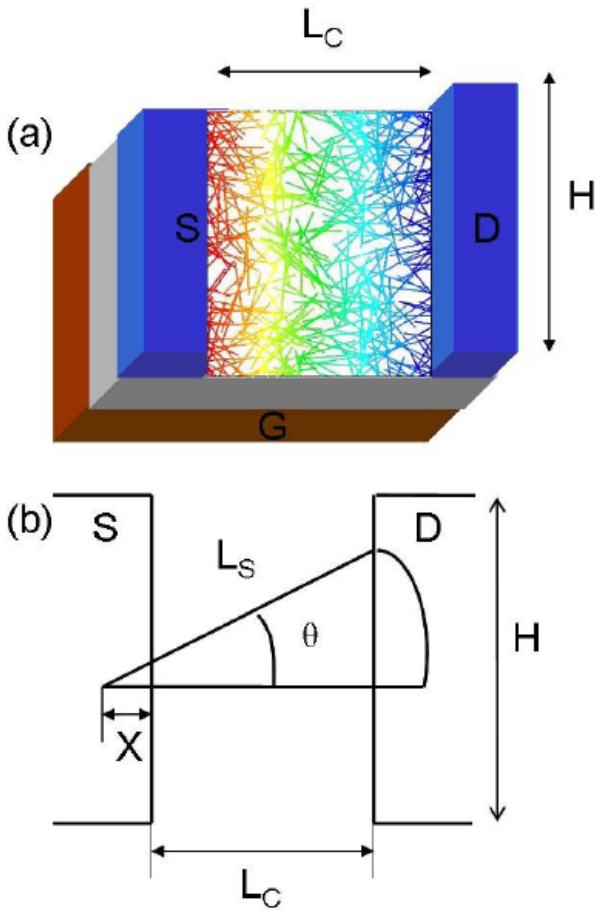

FIG. 1 (color online). (a) A thin-film network transistor with channel length L_C, channel width H, and individual tube length L_S. Source (S), drain (D), and gate (G) are also indicated; the color code of the network reflects the typical potential distribution in a nanotube network for a channel with $L_C = 3\ \mu m$, $H = 4\ \mu m$, $L_S = 2\ \mu m$, $c_{ij} = 5.0$, and $\rho = 3.5\ \mu m^{-2}$. (b) Nomenclature for bridging tube calculation.

Kumar et al., *Phys Rev Lett* 066802, 2005.

Low CNT density: few CNT-CNT contacts

- Density is below percolation threshold
- Vary channel length relative to mean free path: ballistic and diffusive regimes
- L_C = channel length, L_S = CNT length

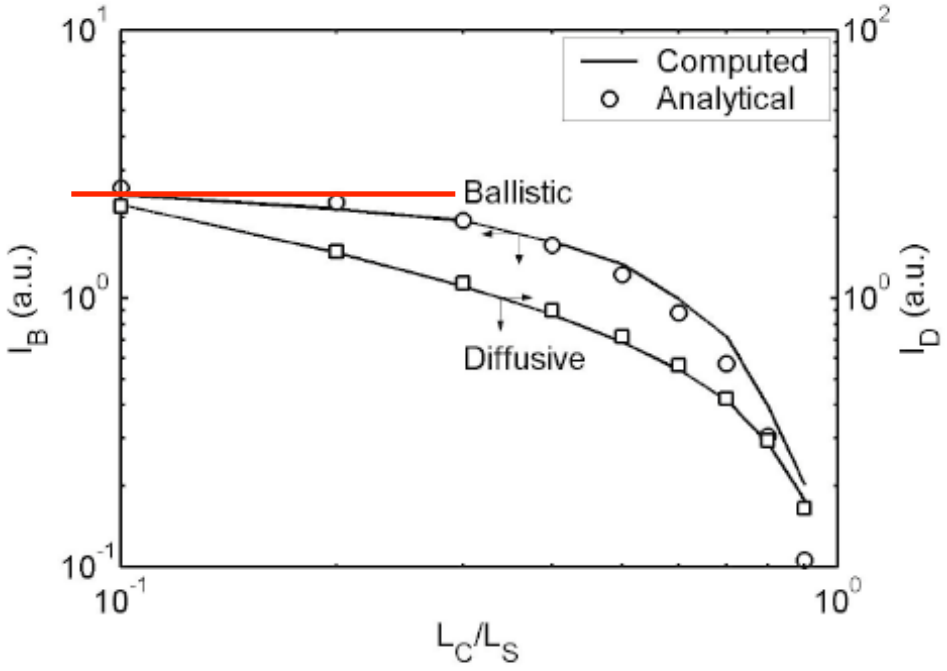

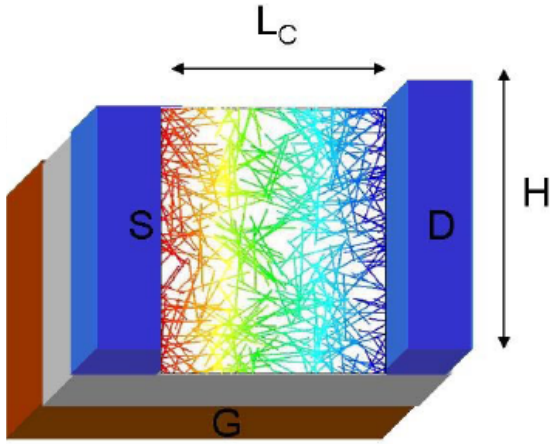

$$I_B \alpha N_S = \frac{2D_x}{\pi}\int_0^{\theta_L}(L_S\cos\theta - L_C)d\theta$$

$$= \left(\frac{2}{\pi}\right)D_x L_S\left[\sqrt{1-\left(\frac{L_C}{L_S}\right)^2} - \left(\frac{L_C}{L_S}\right)\cos^{-1}\left(\frac{L_C}{L_S}\right)\right]. \quad (1)$$

FIG. 2. Comparison of analytical results and numerical predictions of channel length dependence of ballistic and diffusive currents for densities below the percolation limit.

Kumar et al., *Phys Rev Lett* 066802, 2005.

High CNT density: many contacts

- Channel length is much larger than mean free path for electron scattering with phonons and at tube-tube contacts
- Occurs when:
  - Channel is long
  - Channel is short and density far exceeds percolation threshold

- Conduction strongly depends on tube-tube contact resistance
- I-V characteristics (conductance exponent) depend on L_C

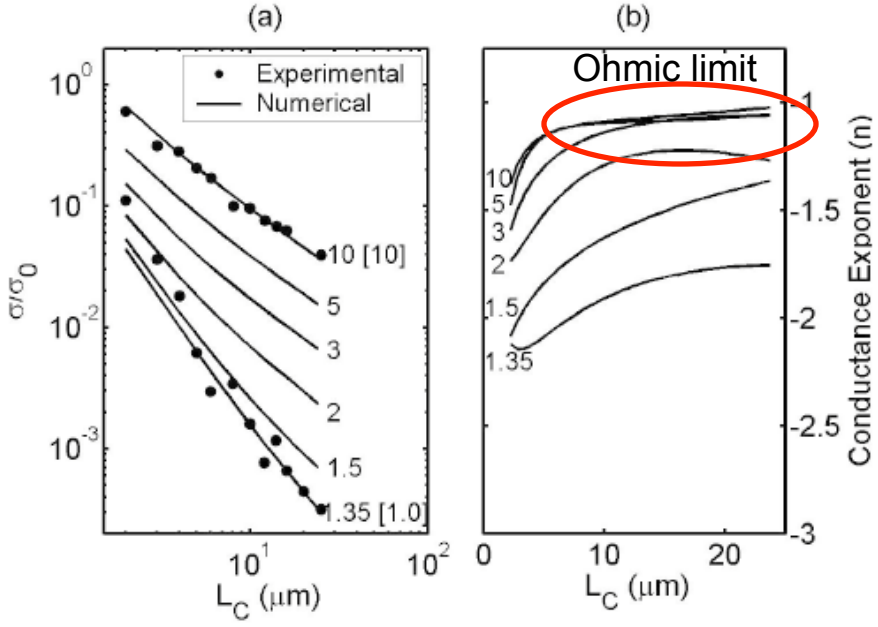

FIG. 3. (a) Computed conductance dependence on channel length for different densities (ρ) in the strong coupling limit ($c_{ij} = 50$) is compared with experimental results from [15]. $\sigma_0 = 1.0$ (simulation; $\rho = 1.35$–$10\ \mu m^{-2}$), $\sigma_0 = 1.0$ (experiment; $\rho = 1.0\ \mu m^{-2}$), and $\sigma_0 = 1.4$ (experiment; $\rho = 10.0\ \mu m^{-2}$). The number after each curve corresponds to ρ and the number in [] corresponds to ρ in experiments from [15]. (b) Dependence of the conductance exponent (n) on channel length for different densities (ρ) based on Fig. 3(a) (i.e., $\sigma/\sigma_0 \sim L_C^n$). Assumed parameters, chosen to reflect experimental conditions in [15], are: $H = 90\ \mu m$, $L_S = 2\ \mu m$, and $L_C = 1$–$25\ \mu m$.

Kumar et al., *Phys Rev Lett* 066802, 2005.

Percolation in metal nanowire films

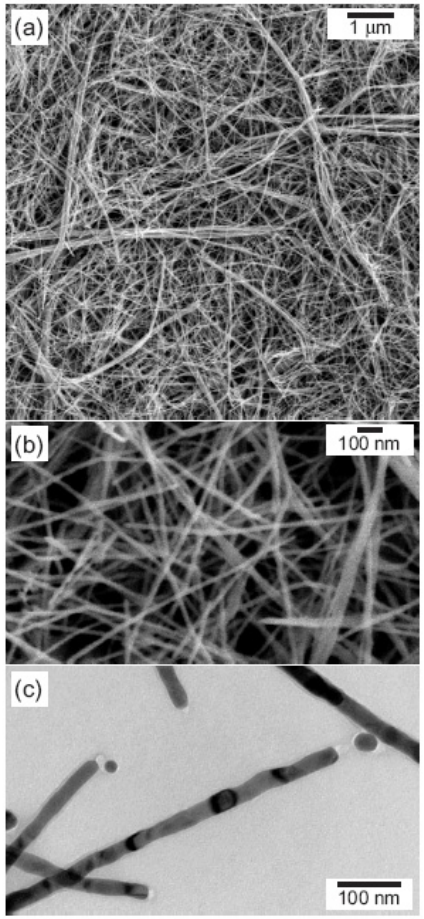

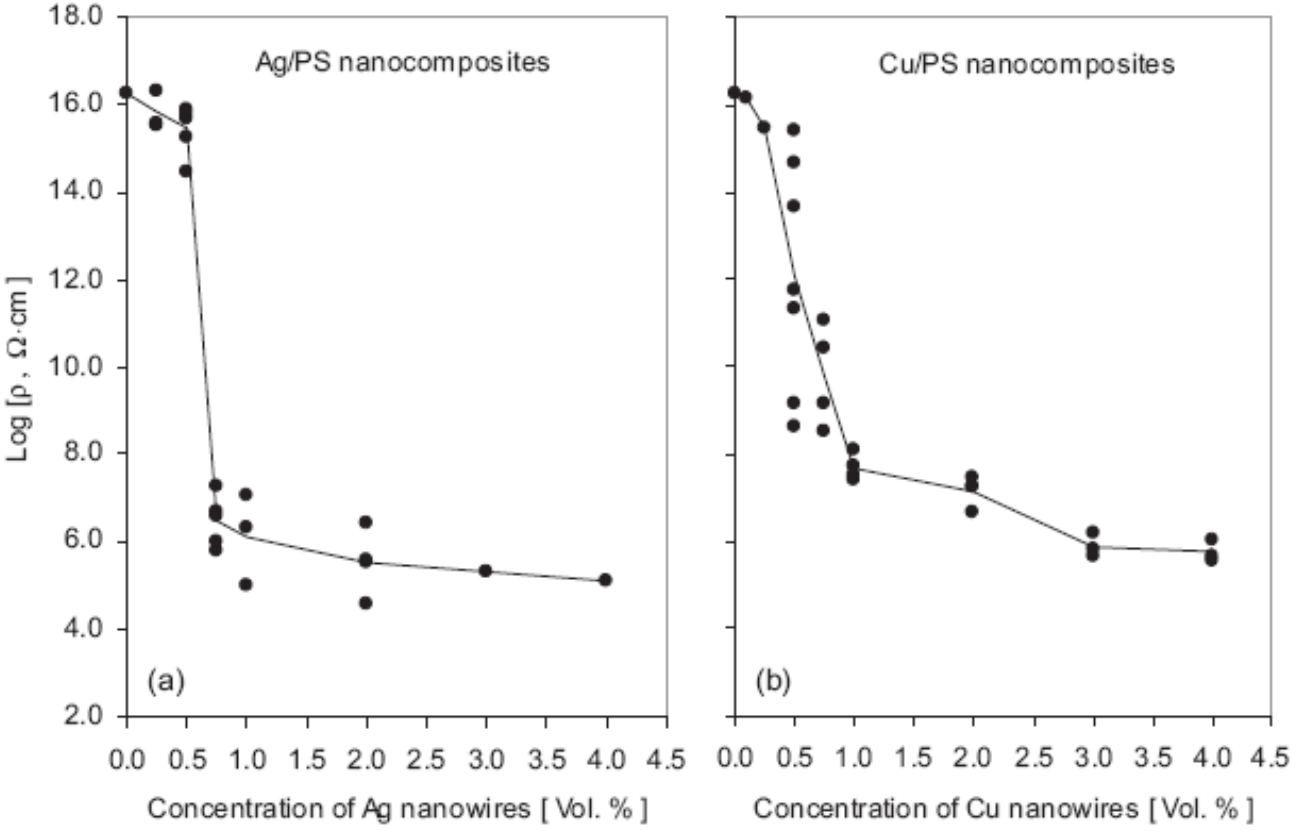

Figure 6. Volume electrical resistivity (ρ) of PS nanocomposites for different concentrations of a) Ag and b) Cu nanowires. The lines connect the average values calculated from replicate specimens prepared at each concentration.

Gelves et al., *Advanced Functional Materials* 16:2423-30, 2006.

Percolation in nanoparticle films

Antimony-doped tin oxide (ATO)

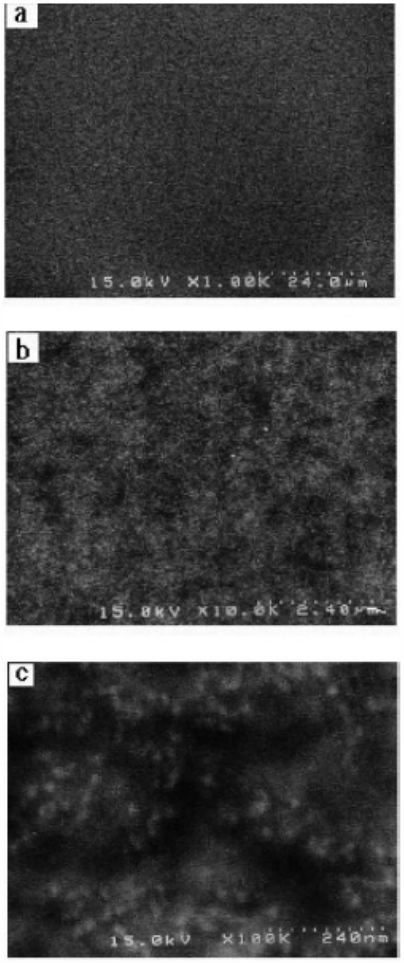

Figure 3. FE-SEM images of the surface of deposited layers prepared with ATO volume fraction $\phi = 0.0083$ observed at low (a), medium (b), and high (c) magnifications.

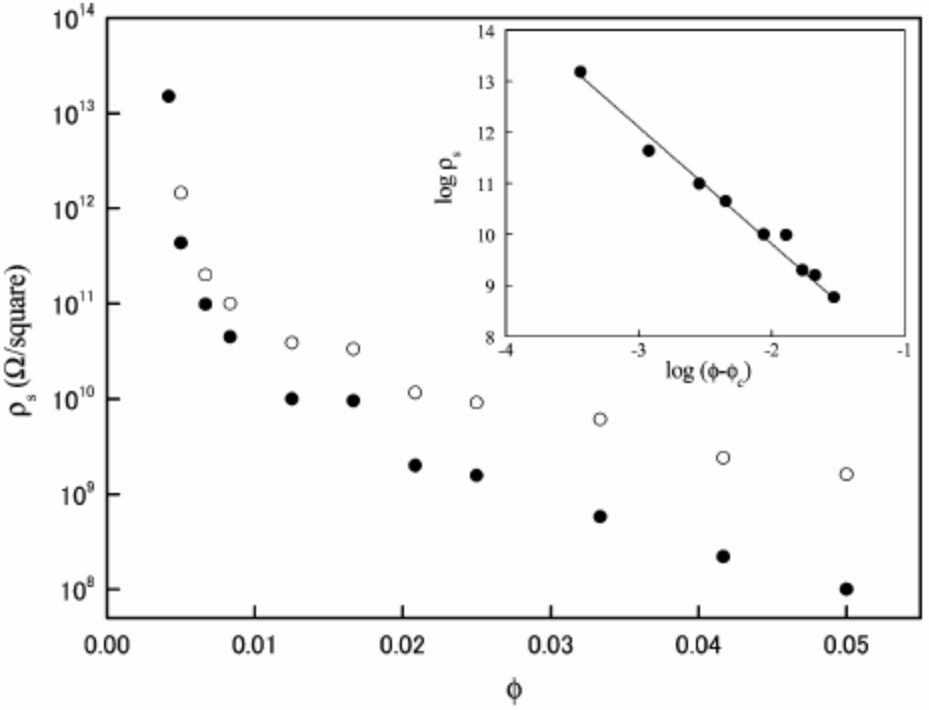

Figure 4. Surface resistivity as a function of ATO volume fraction for deposited layers. Controlled relative humidity during layer deposition: 54% RH (●), 40% RH (○). Inset: log−log plot of surface resistivity ρ_s versus ATO volume fraction ϕ. Relative humidity during layer deposition: 54% RH.

Wakabayashi et al., *Langmuir* 22:9260-9263, 2006.

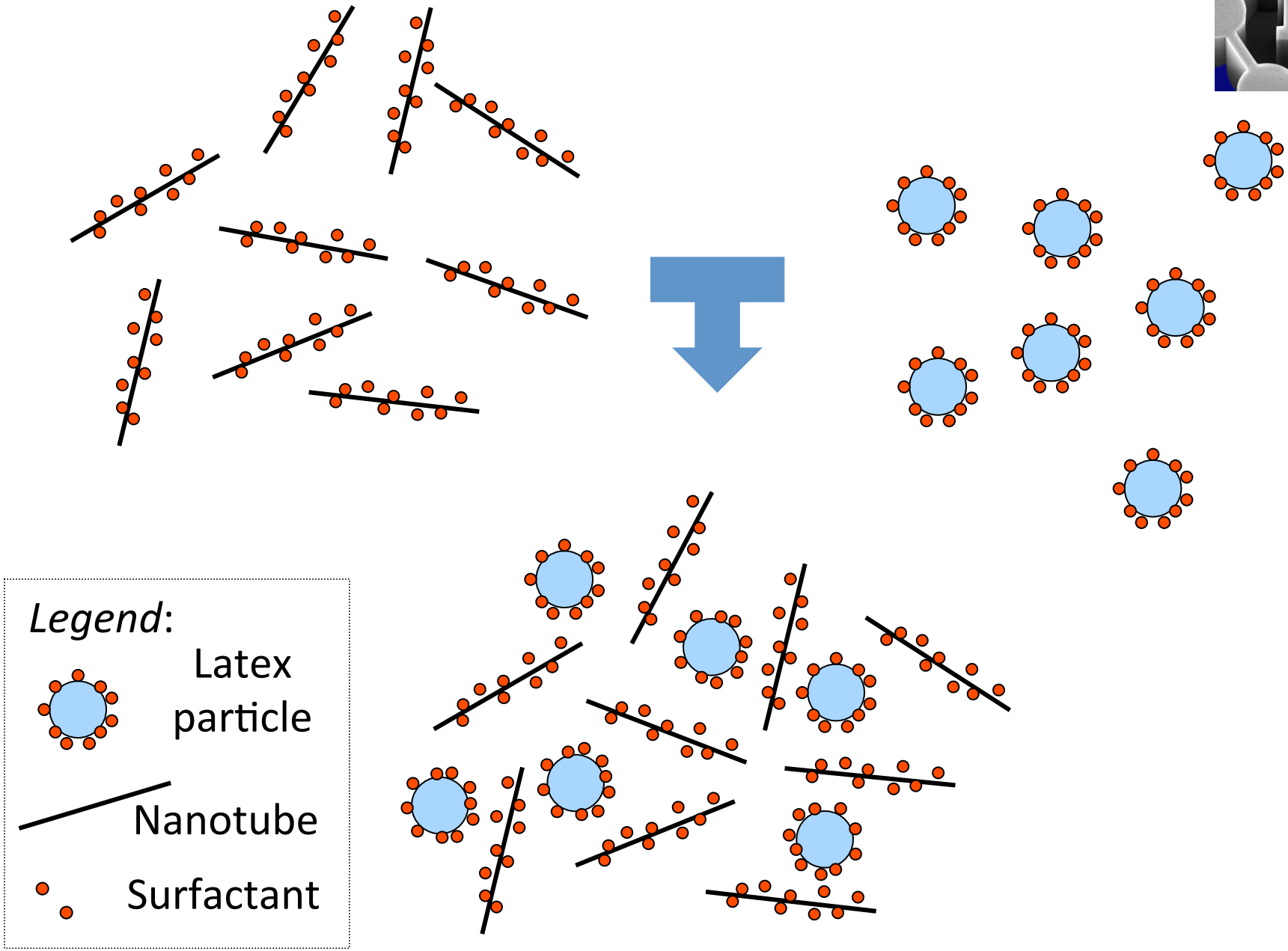
Legend:
Latex particle
Nanotube
Surfactant

CNT/PS film

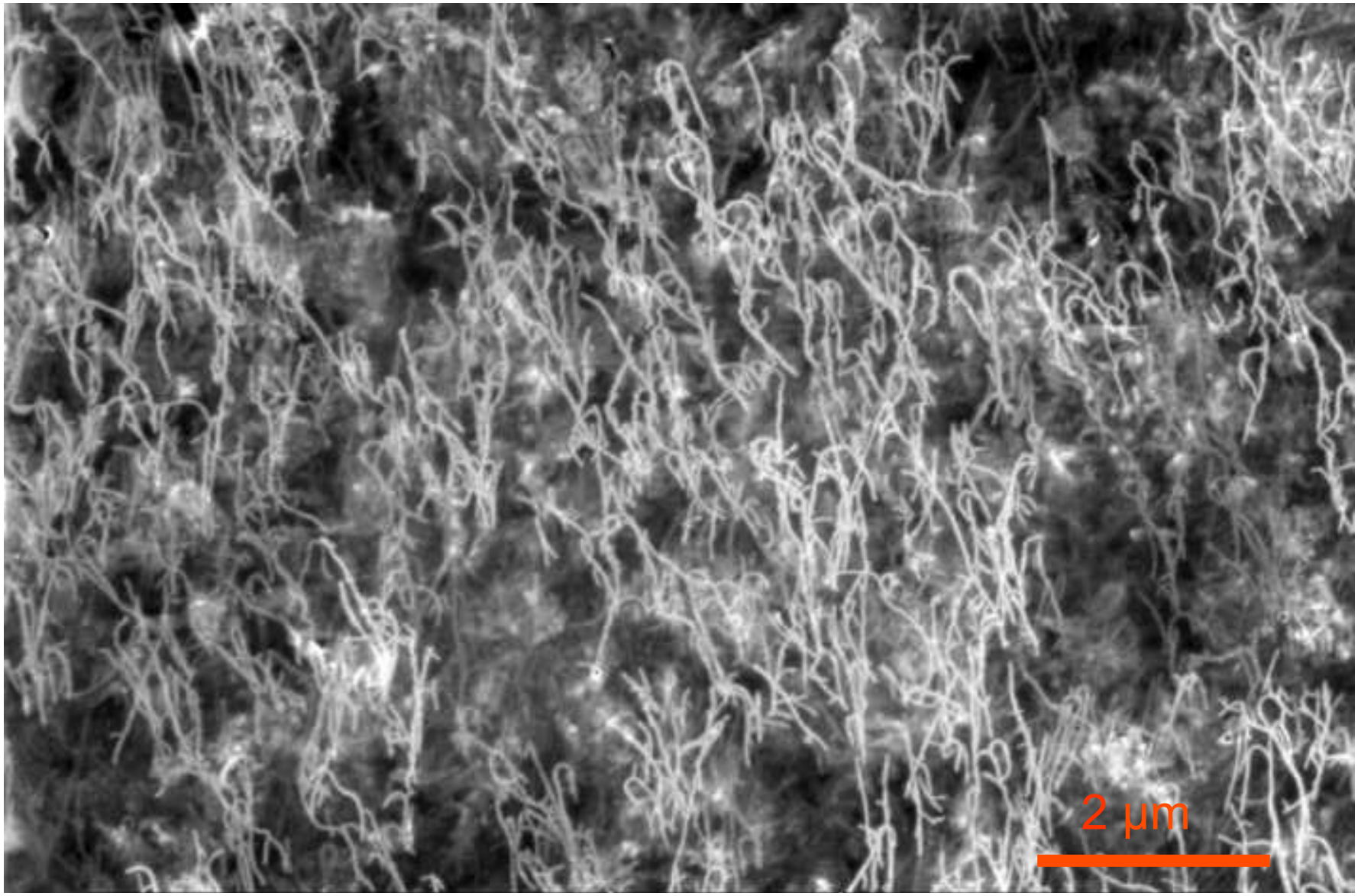

N. Grossiord et al.

MWCNT/PS composites

- Disperse CNTs in SDS surfactant
- Mix with PS; emulsion polymerization

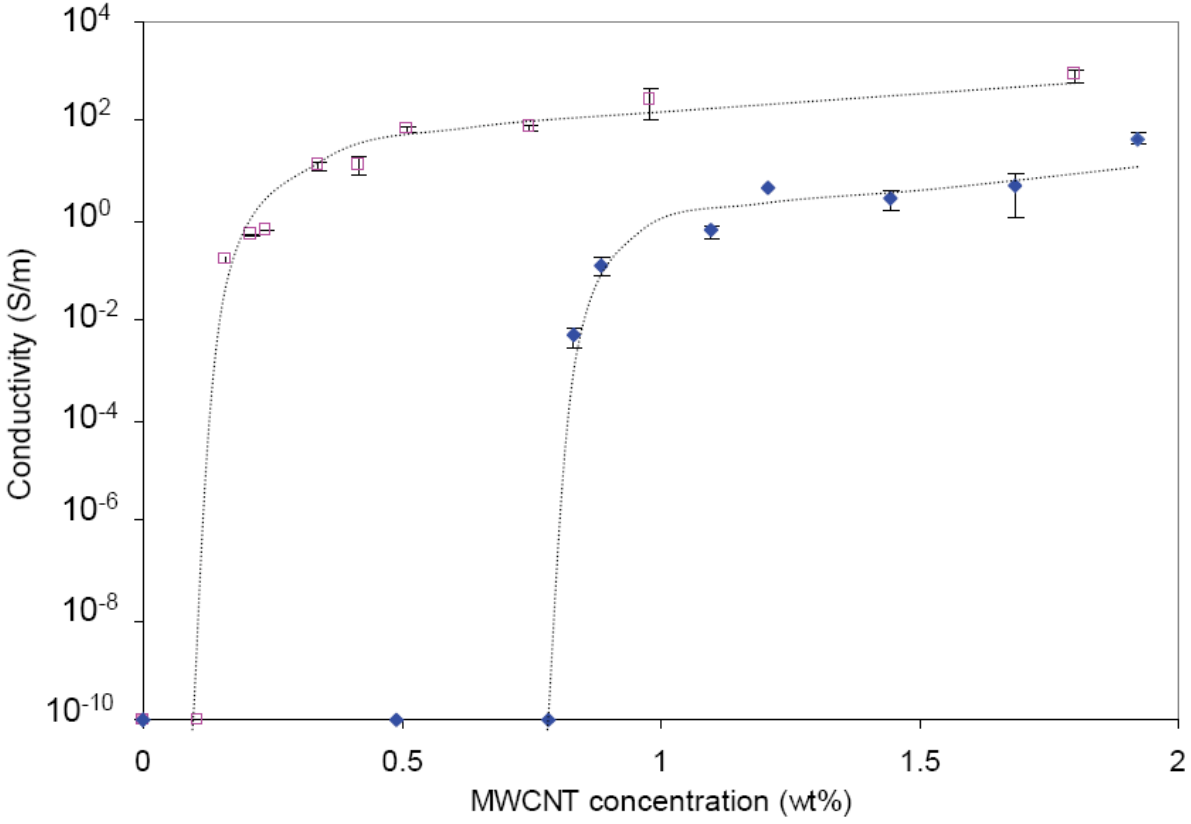

Figure 6.7. Four-point conductivity of MWCNT/PS composite as a function of MWCNT content. Each point of the curve is the average of several measurements performed several times on several locations on the two sides of the nanocomposite films. Several types of MWCNTs, viz. VGCNTs (□) and IPCNTs of Nanocyl, batch 060213 (◆), were dispersed in the same PS matrix, namely EP2.

Bounds

- Individual CNT = 10^5-10^8 S/m (MW→SW)
- Buckypaper (about 50% CNTs) = 10^4-10^5 S/m
- Typical composite (1 wt% CNTs) = 10^0-10^3 S/m

N. Grossiord et al, TU/Eindhoven.

Performance relates to CNT quality

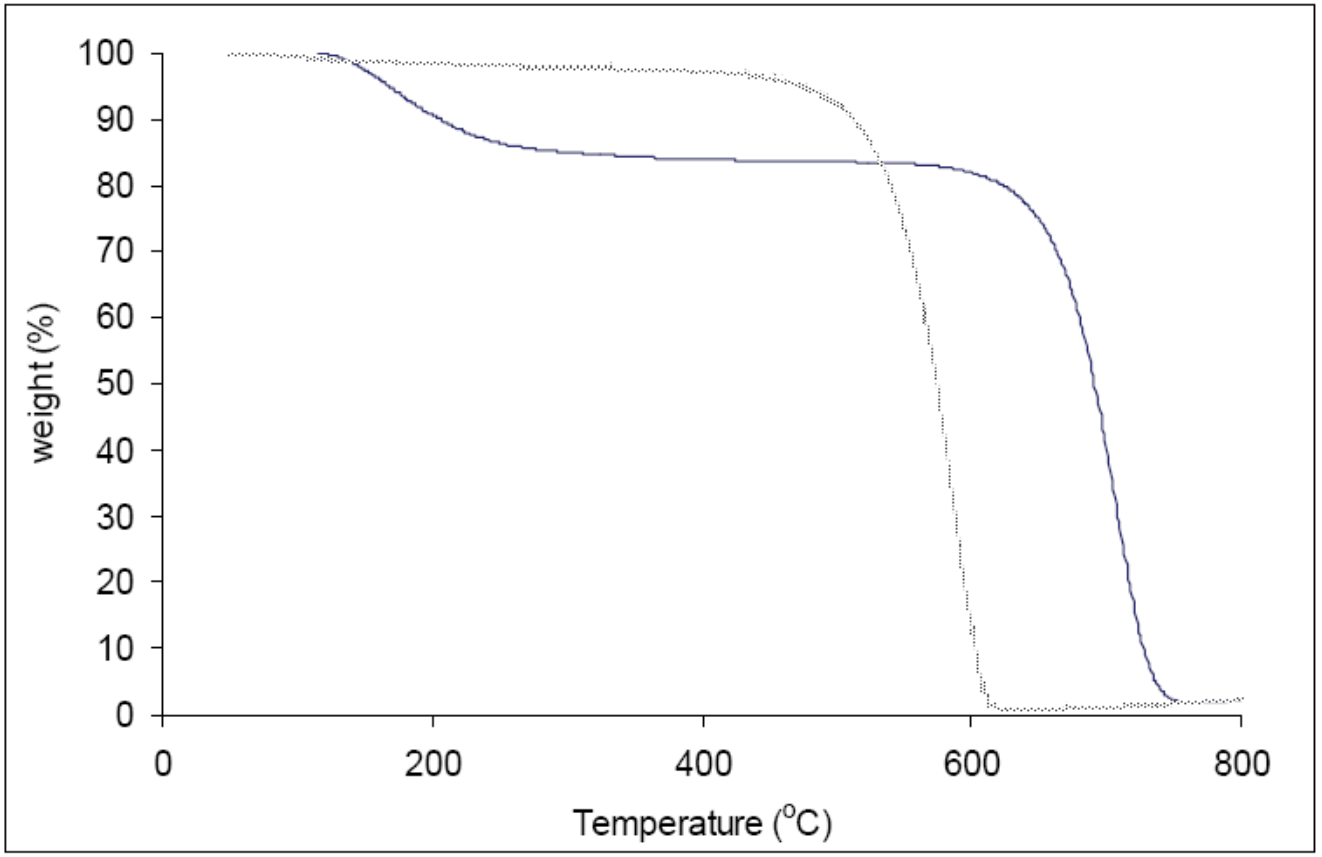

Figure 6.9. Thermograms of crude VGCNTs (plain line) and of IPCNTs (dashed line) performed under air at a flow rate of 25 mL/min and a heating rate of 5 °C/min.

N. Grossiord et al, TU/Eindhoven.

Thin CNT networks are also transparent

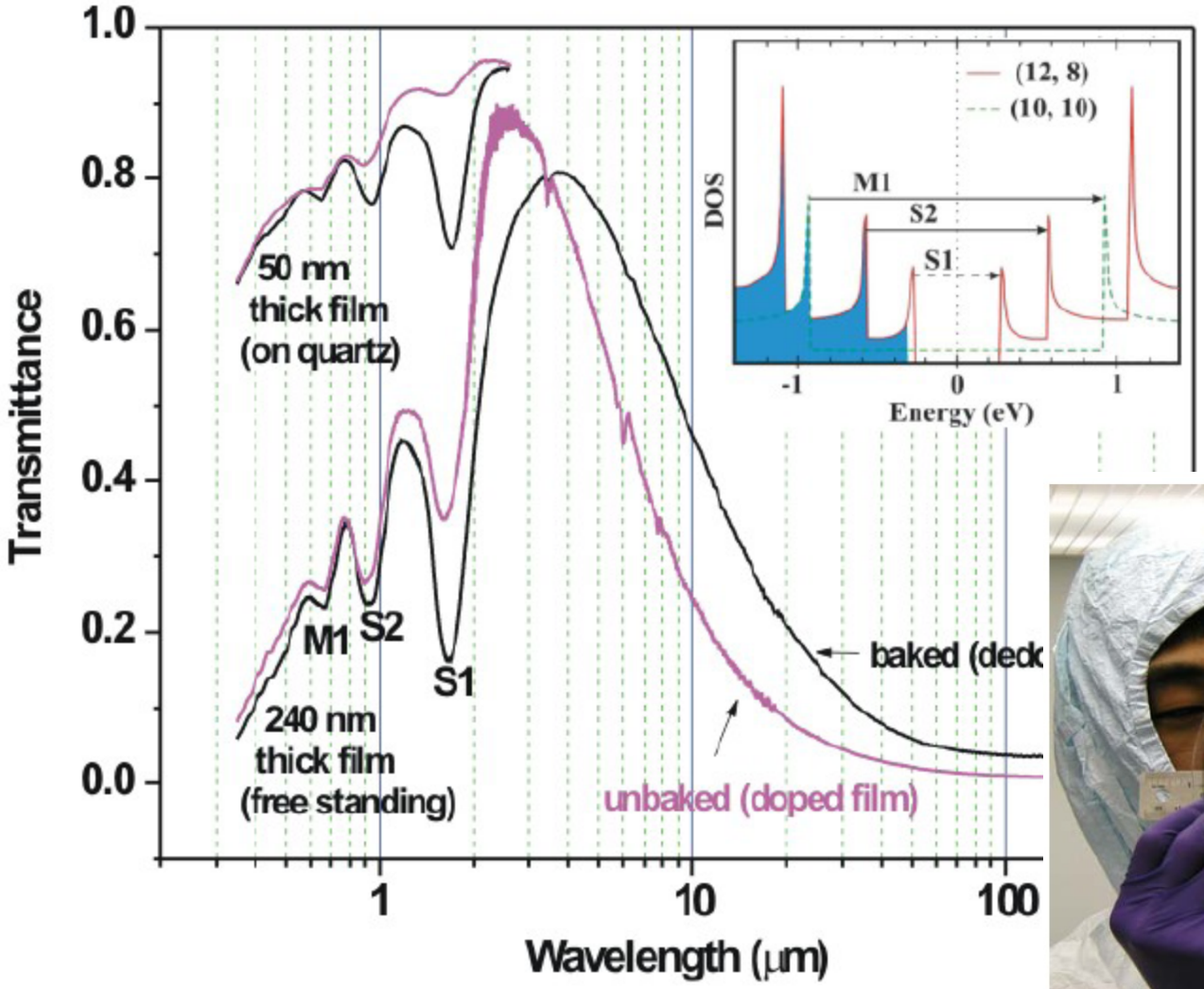

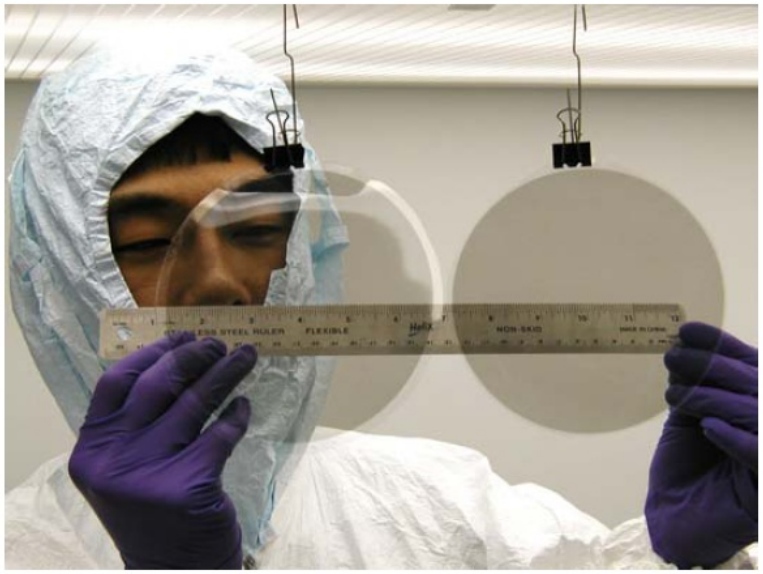

A. Rinzler.

Reverse percolation strain sensors

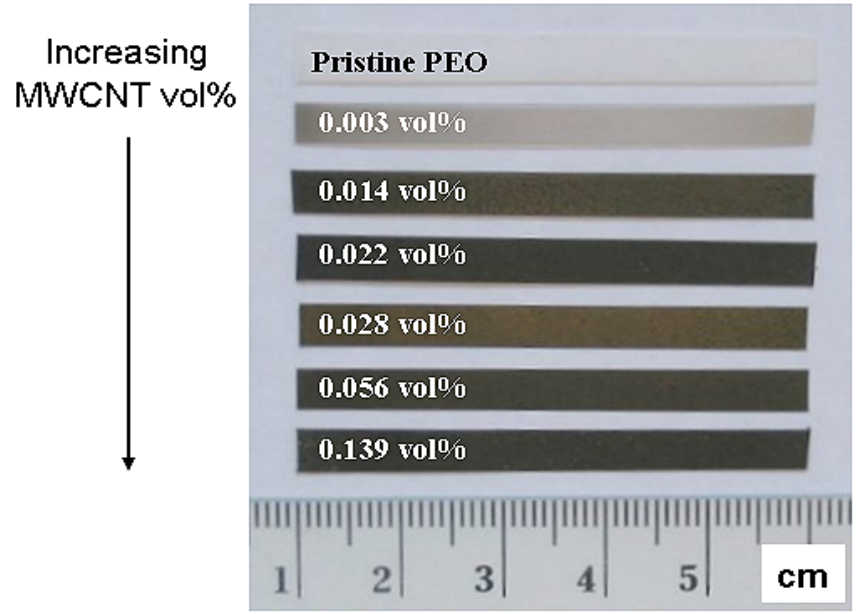

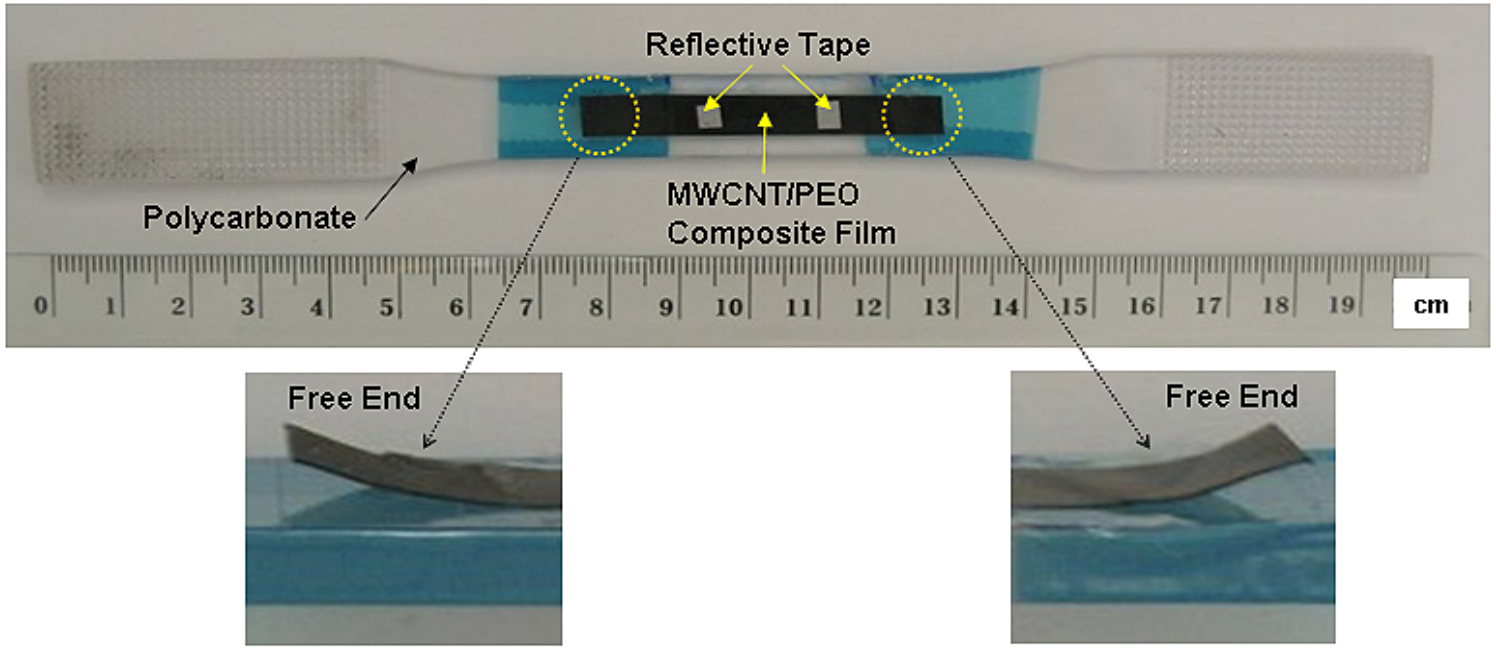

M. Park et al.

Reverse percolation strain sensors

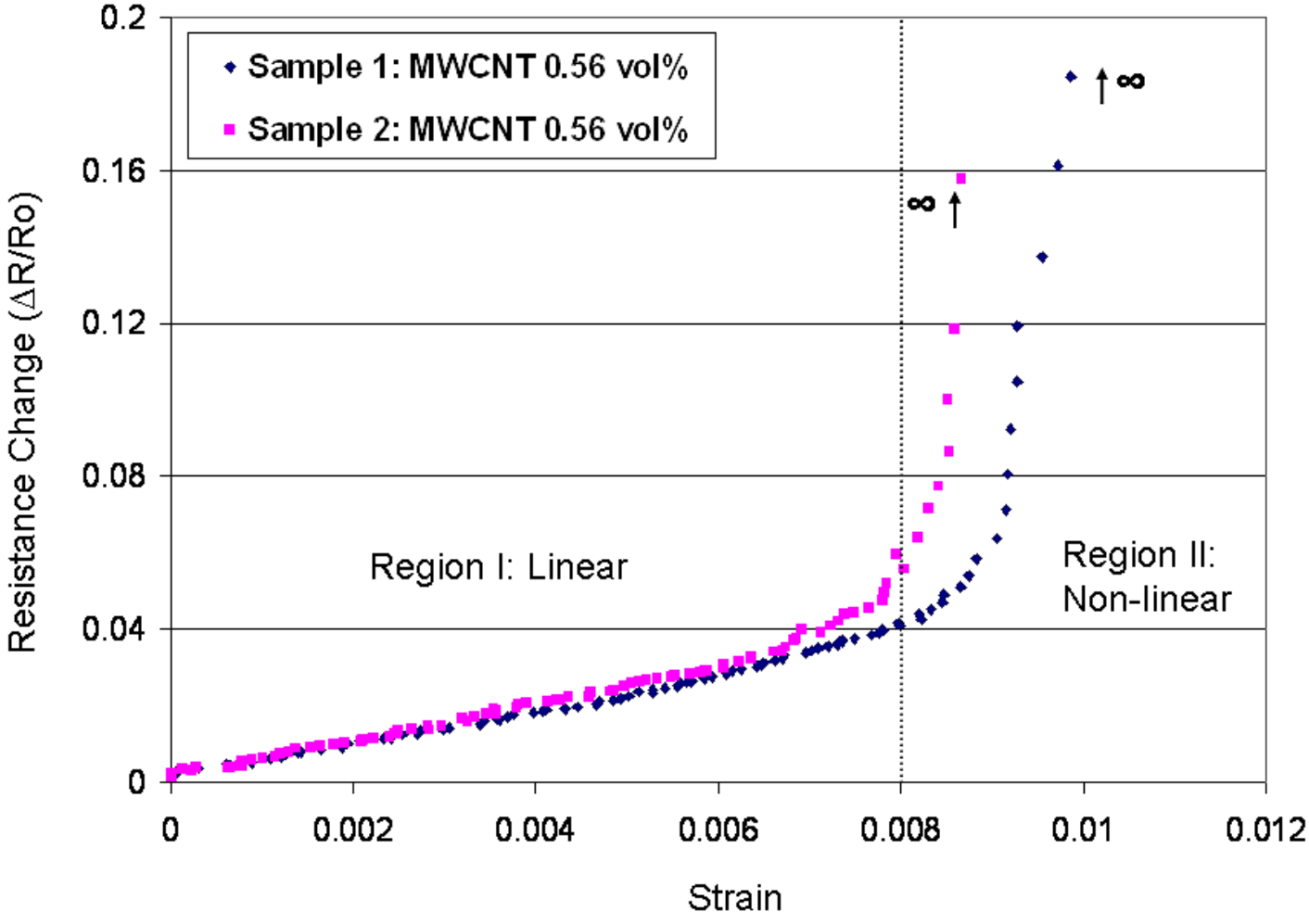

What is the mechanism of resistance increase in each region?

M. Park et al.

Electrical properties of CNT assemblies: real vs. ideal values

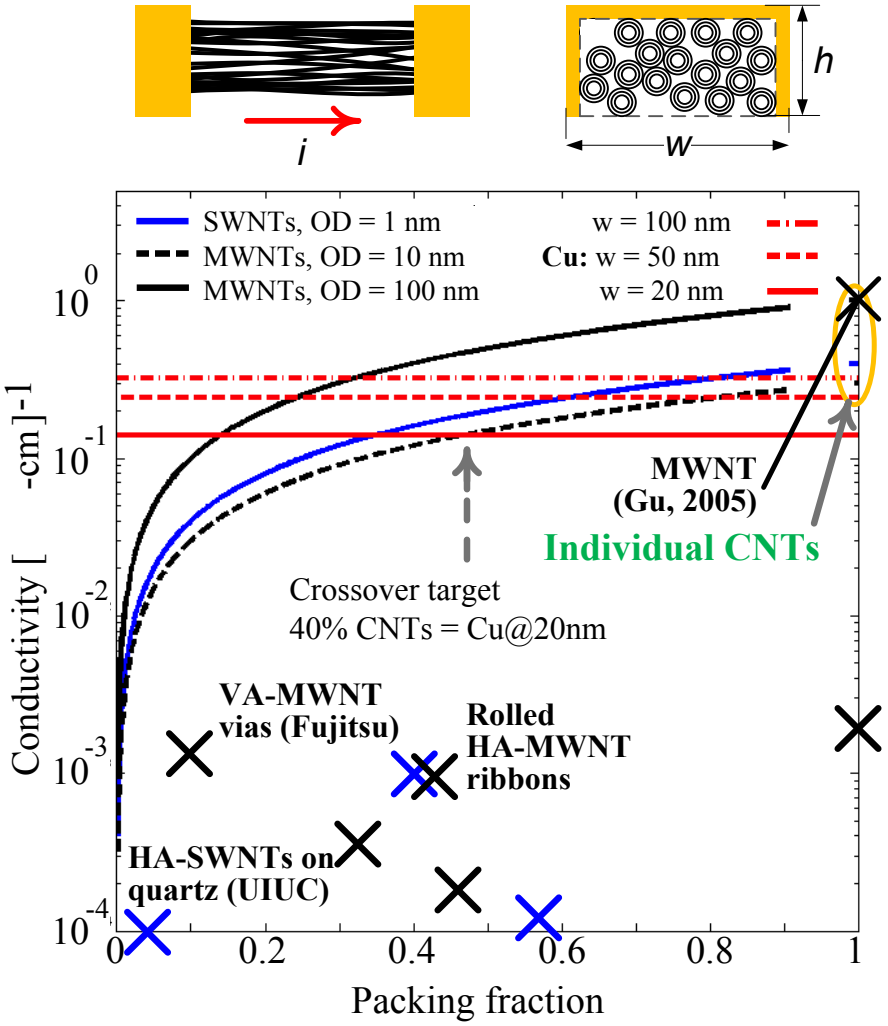

More applications of percolation theory

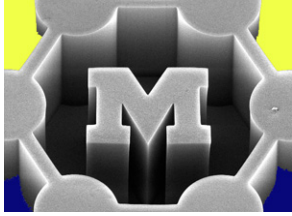

- Spread of forest fires
  - predicting rate of forest consumption and extinction
- Distribution of oil/gas inside porous reservoirs
  - predicting needed drilling locations and reservoir size
- Polymer and gel materials
  - predicting kinetics of polymerization and gelation

Peters et al., *PNAS* 101(42):15130:2004.

Thermal properties of networks

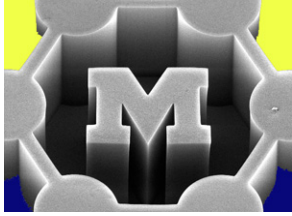

- No sharp transition at percolation
- Phonon scattering at structure-structure contacts dominate thermal transport
- Structure-matrix interactions can also significantly affect conductivity by phonon scattering

Individual CNTs have exceptional thermal conductivity

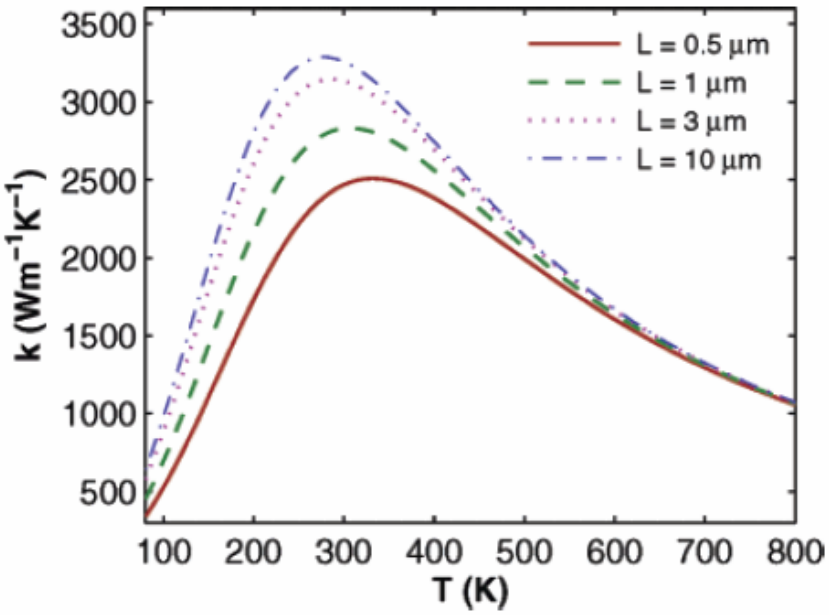

Figure 6. Analytic plot of the intrinsic SWNT thermal conductivity over the 100−800 K temperature range as computed with eq 3. The length dependence is included heuristically with a simple scaling argument, but differences in chirality may lead to variations up to 20% between different tubes.[11]

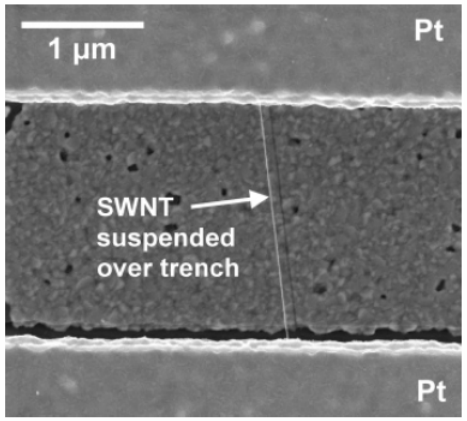

Figure 1. Scanning electron microscope (SEM) image of a typical SWNT freely suspended across a 2-μm trench and lying on top of the Pt contacts. This sample was coated with 1.5 nm Ti/2.5 nm Au to facilitate SEM imaging.

Phonon mean-free path at 300 K

$$k(L, T) = [3.7 \times 10^{-7}T + 9.7 \times 10^{-10}T^2 + 9.3(1 + 0.5/L)T^{-2}]^{-1} \quad (3)$$

Pop et al., *Nano Letters* 6(1):96, 2006

Thermal contact resistance

macroscopic formulation

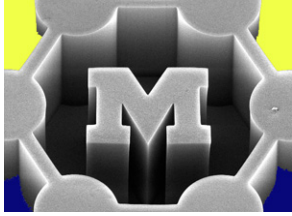

"Macroscopic" contact resistance

$$R_c = \frac{A\Delta T}{q} = \frac{1}{G_c}$$

A = contact area

q = heat flow per unit area

ΔT = temperature change across interface

h = heat transfer coefficient

$$h = \frac{1}{R_c A} = \frac{G_c}{A}$$

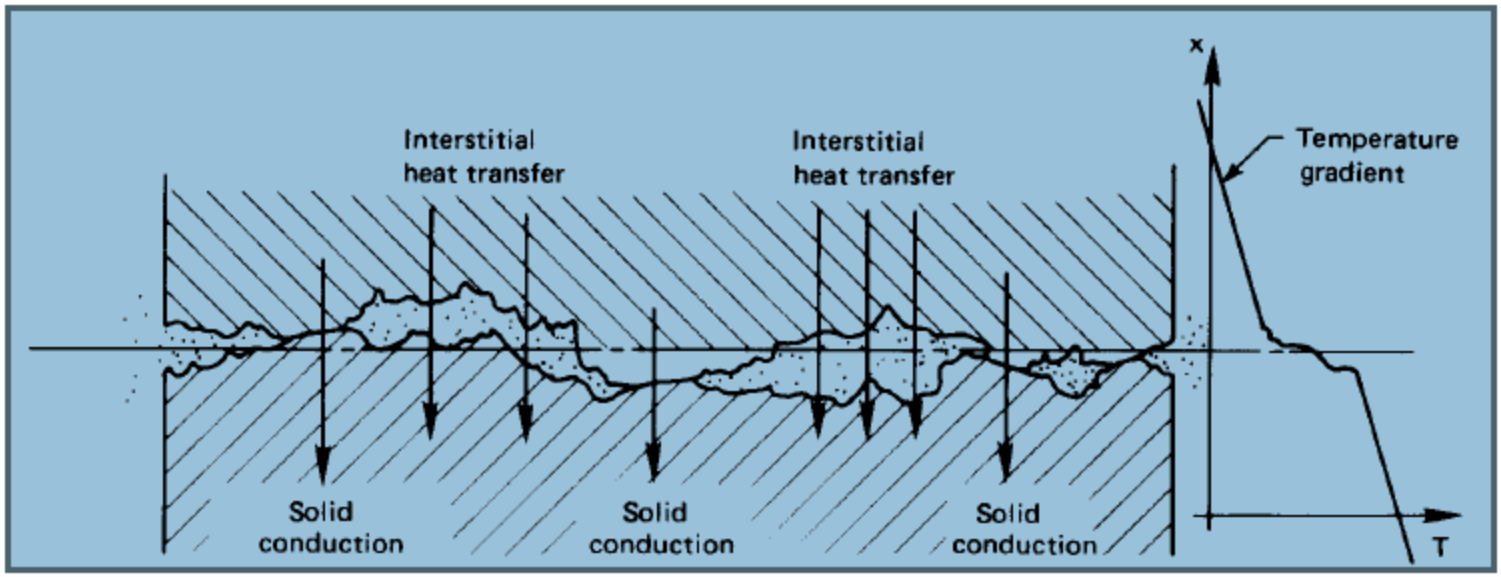

Lienhard.

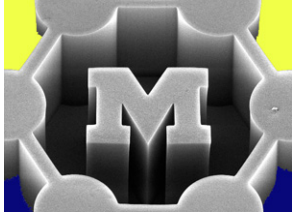

Table 2.1 Some typical interfacial conductances for normal surface finishes and moderate contact pressures (about 1 to 10 atm). Air gaps not evacuated unless so indicated.

Situation	h_c (W/m^{2}K)
Iron/aluminum (70 atm pressure)	45,000
Copper/copper	10,000 – 25,000
Aluminum/aluminum	2,200 – 12,000
Graphite/metals	3,000 – 6,000
Ceramic/metals	1,500 – 8,500
Stainless steel/stainless steel	2,000 – 3,700
Ceramic/ceramic	500 – 3,000
Stainless steel/stainless steel (evacuated interstices)	200 – 1,100
Aluminum/aluminum (low pressure and evacuated interstices)	100 – 400

Lienhard.

Case study: CNT-CNT thermal contact (see extra slides for more details)

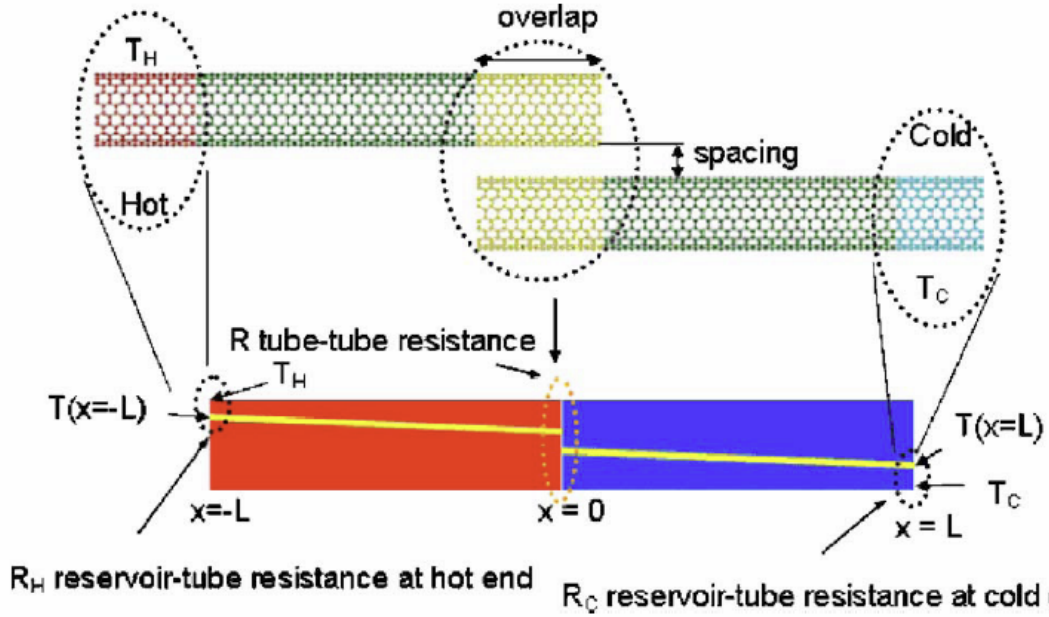

FIG. 1. (Color online) Correspondence between molecular dynamics (upper figure) and finite difference (lower figure) models. Two nanotubes are configured with a given overlap and spacing, which are varied to see the effect on tube-tube and reservoir-tube resistances. Hot and cold ends of the nanotubes are maintained at temperatures T_H and T_C, respectively.

At the boundary $$-k\left.\frac{\partial T}{\partial x}\right|_{0^-} = \frac{T(0^-) - T(0^+)}{R} = -k\left.\frac{\partial T}{\partial x}\right|_{0^+}.$$

Zhong and Lukes, *Phys Rev B* 74:125403, 2006.

Thermal contact resistance

molecular formulation

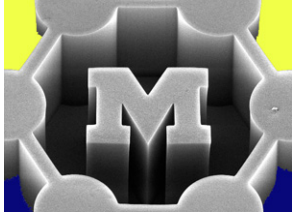

Lennard-Jones potential

$$U(z) = 4\varepsilon\left[\left(\frac{\sigma}{r}\right)^{12} - \left(\frac{\sigma}{r}\right)^{6}\right]$$

repulsive - attractive

Heat is transferred by atomic vibrations at the interface; VDW interactions transfer vibrations across a small gap

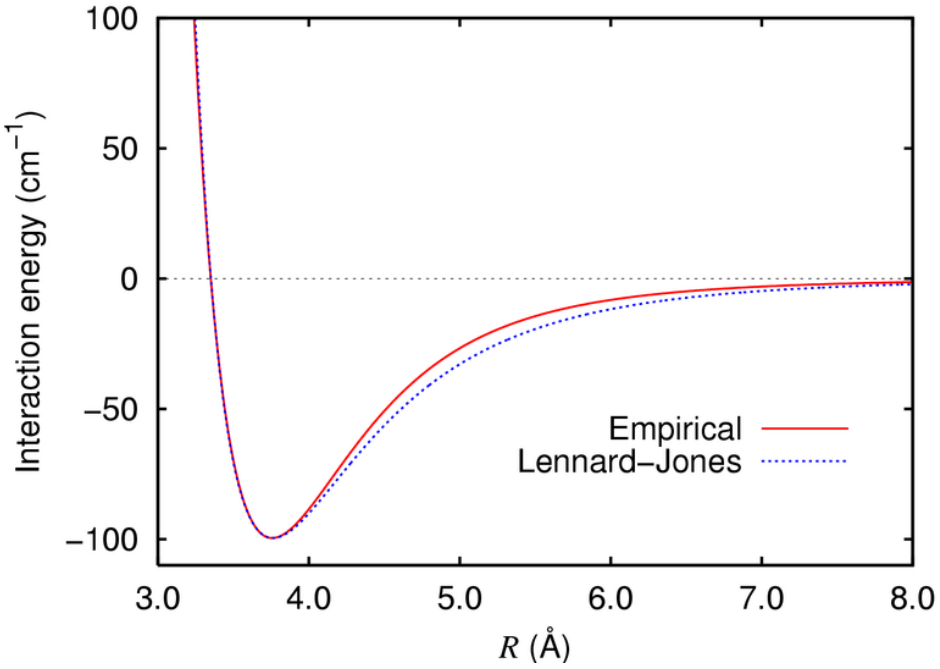

Thermal conductivity of a CNT mat

Heat suspended film by IR and measure resistance versus temperature

Calibrate absorbed power from absorption spectroscopy measurement at applied IR wavelength (940 nm)

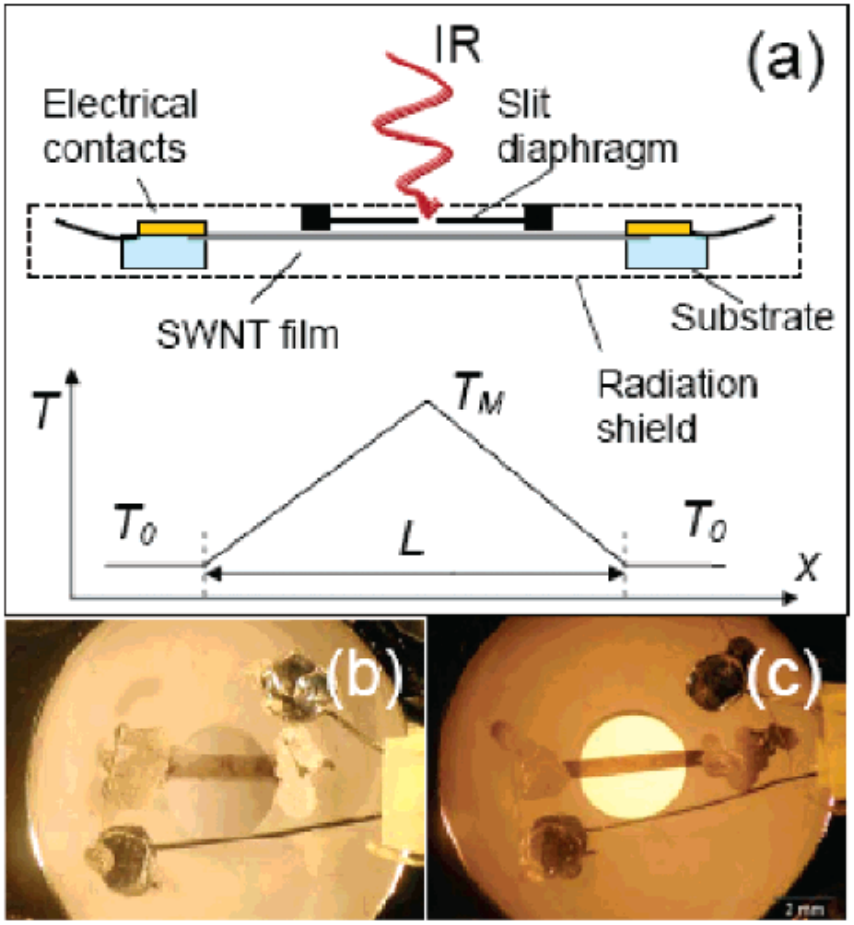

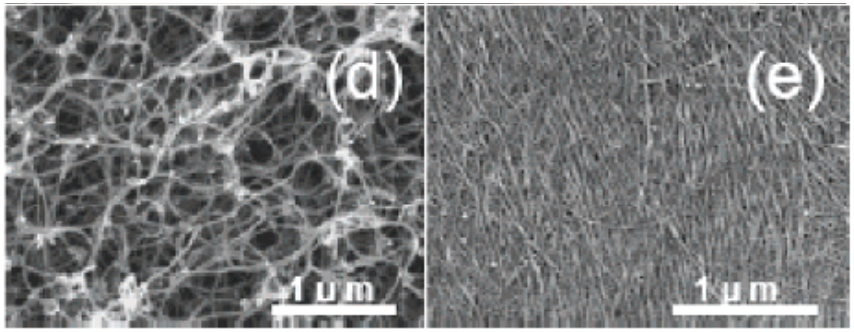

Figure 1. (a) Bolometric configuration for measurement of thermal conductivity of SWNT film suspended between electrical contacts. The heat is provided by IR LED illuminating the SWNT film through the narrow slit diaphragm which generates a triangular temperature profile. (b) Semitransparent film of as-prepared SWNTs film grown in the electric arc discharge chamber and suspended across the opening in a sapphire ring. (c) Semitransparent film of purified SWNTs prepared by vacuum filtration mounted for thermal conductivity measurements. SEM images of fragments of (d) AP-SWNT film, and (e) P-SWNT film. Note that the P-SWNT film is much more densely packed than the AP-SWNT network.

Itkis et al., *Nano Letters* 7(4):900-904, 2007.

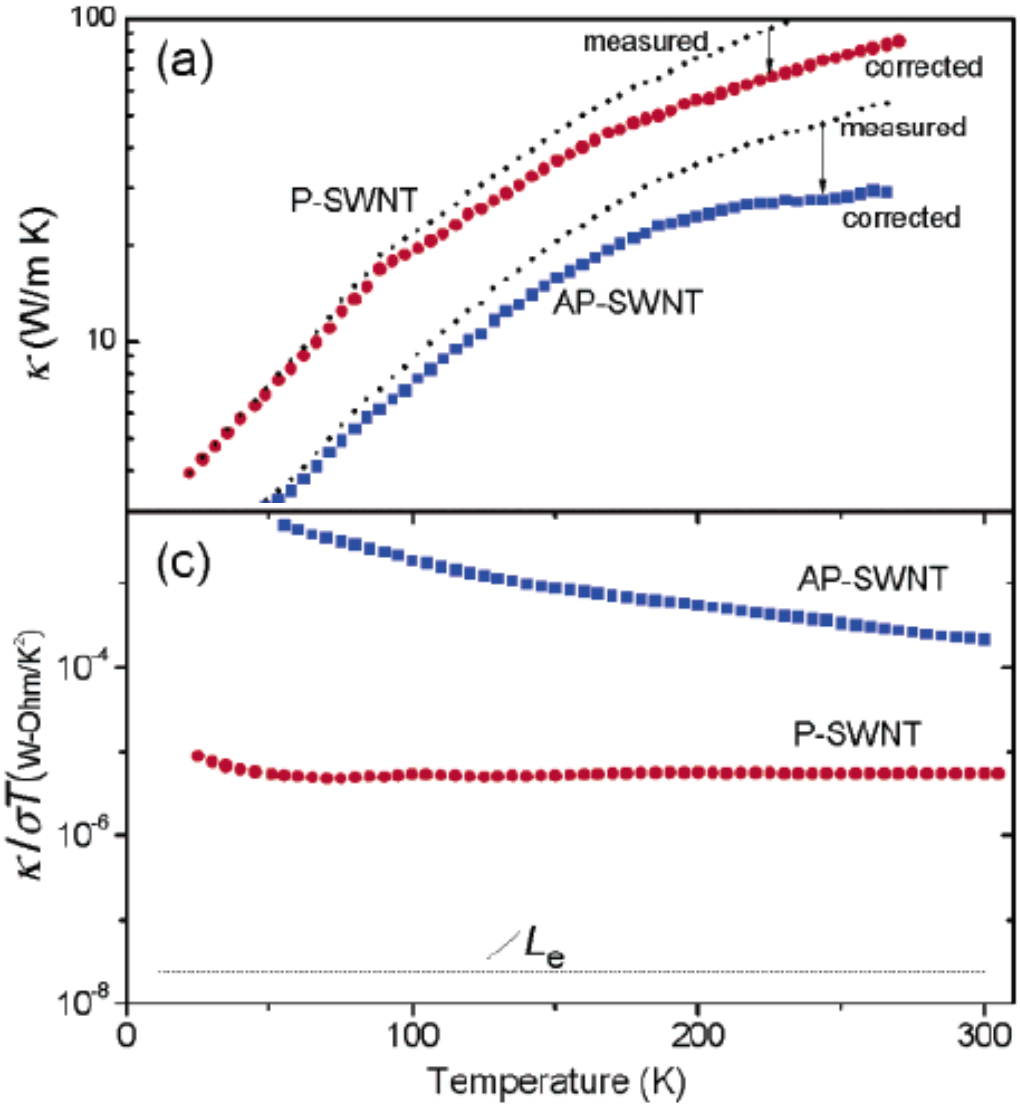

AP- = as-prepared
P- = purified

Lorentz number:
Relative role of phononic versus electronic heat conduction

$$L = \frac{k}{\sigma T}$$

L_e = for metal

→ Composites show a lower thermal conductivity (polymer layer is additional thermal barrier)

Itkis et al., *Nano Letters* 7(4):900-904, 2007.

Measuring thermal conductivity of a packed bed (ASTM standard)

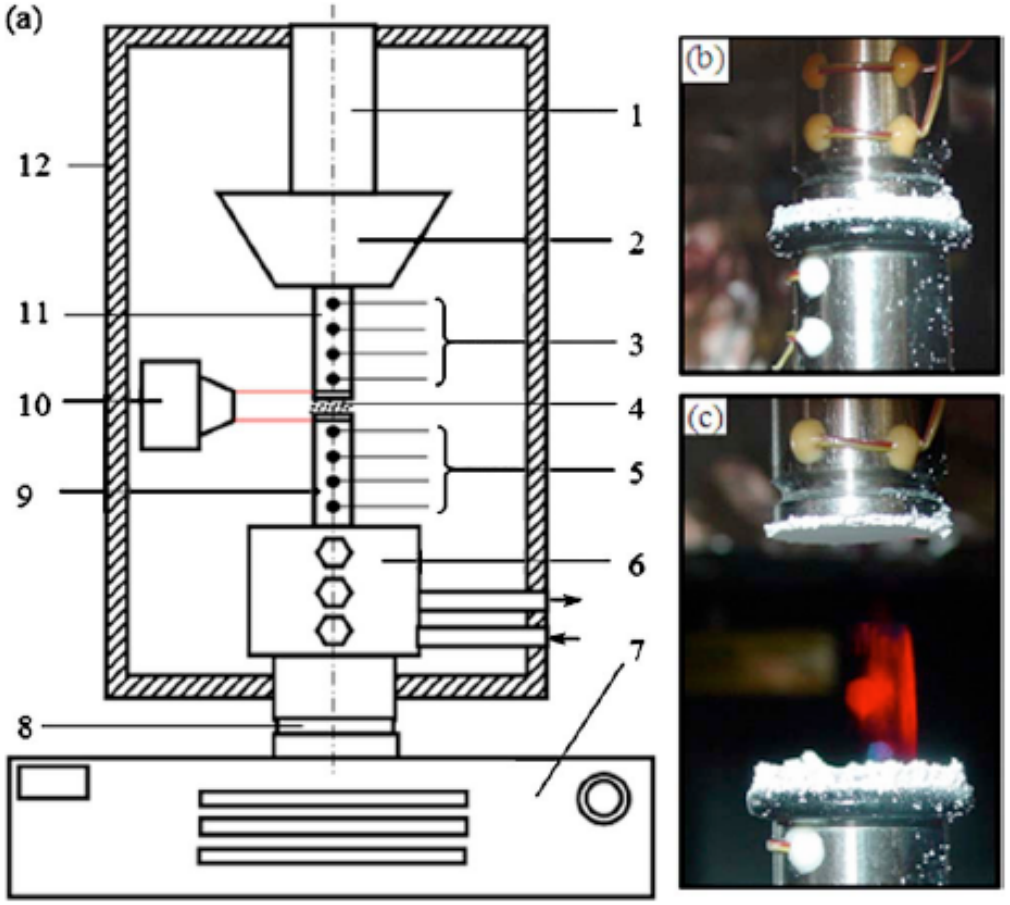

FIG. 1. (Color online) Measurements of the thermal conductivity of alumina nanoparticle bed using a steady-state heat conduction apparatus based on ASTM D5470. (a) Schematic of the test apparatus: 1, hydraulic actuated shaft; 2, electrical heater with insulation; 3 and 5, thermocouples; 4, test sample; 6, water-cooled cold block; 7, base and control panel; 8, alignment fixture and load cell; 9, lower rod; 10, laser extensometer; 11, upper rod; 12, insulation box. (b) Photograph during test. (c) Photograph after test.

Top rod: resistively heated

Bottom rod: water-cooled

Stainless steel rods give a measurable temperature drop across the series of mounted TCs

Can we have "too much" contact?

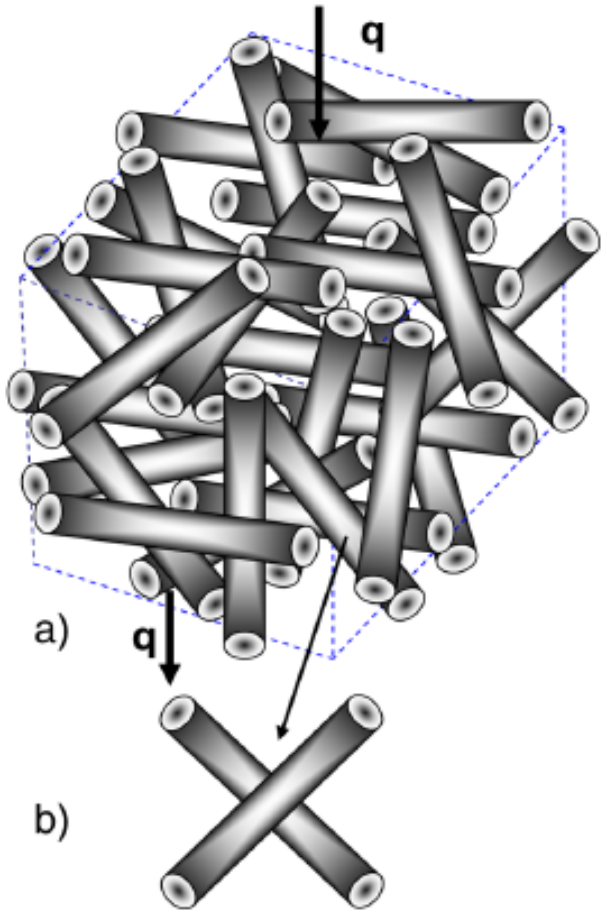

FIG. 1 (color online). (a) Schematic of the 3D random array of CNTs forming a bed. (b) Schematic of the crossed CNT junction.

TABLE I. Thermal conductivity of the CNT bed.

Sample	Pressure (psi)	k_{bed} (W/m K)	ϕ
1–2 nm	20	0.155	17.2%
SWCNT	50	0.175	18.1%
	90	0.194	19.4%
<8 nm	20	0.154	12.7%
MWCNT	50	0.171	13.7%
	90	0.195	15.2%
60–100 nm	20	0.134	8.9%
MWCNT	50	0.154	10.4%
	90	0.170	12.4%

10X lower than for a 3D network using previously measured CNT-CNT thermal contact resistance –why?

Prasher et al., *Physical Review Letters* 102:105901, 2009.

Effect of two junctions separated by less than the phonon mean free path

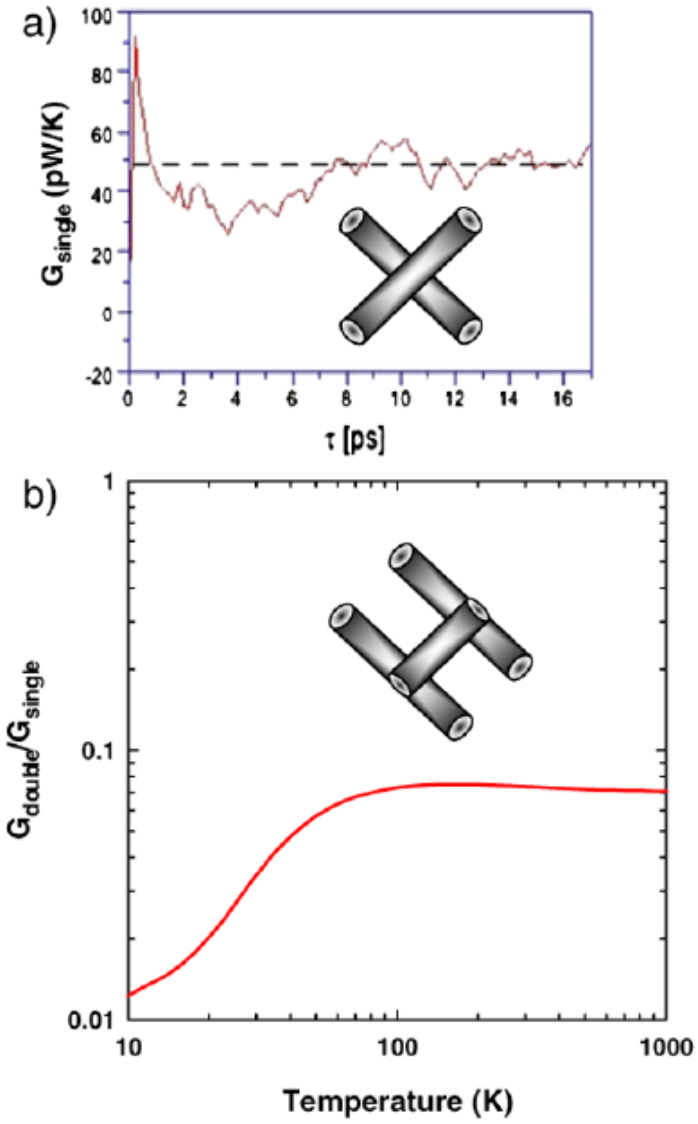

FIG. 3 (color online). (a) The running integral of the power auto correlation function converging to the contact conductance between the two (10, 10) SWCNT obtained by MD simulation for a single isolated junction. Atomistic Green's function simulation independently gives similar value of the contact conductance (see text for details). The error in conductance obtained from MD is ~5 pW/*K* (b) The lower data show the *ratio* of the conductance of a double junction and a single junction obtained by AGF simulations. The two junctions in the double junction are separated by a distance much smaller than the mean free path. The conductance of the double junction is ~1 order of magnitude smaller than a single junction (see text for details).

Application of tuning junction behavior:
thermoelectrics

Prasher et al., *Physical Review Letters* 102:105901, 2009.

Mechanical properties of networks

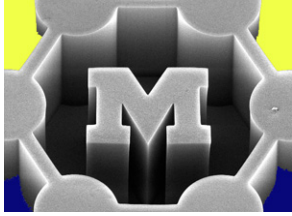

- Largely follow a linear rule of mixtures
- Stiffness can scale to near-theoretical values
- Strength governed by defect isolation and propagation
- Overlap/joining between structures (shear strength) vital for load transfer, especially between strong structures and a weak matrix
- Alignment (waviness) is critical
- Joint morphology is critical

Paper: a mechanical network

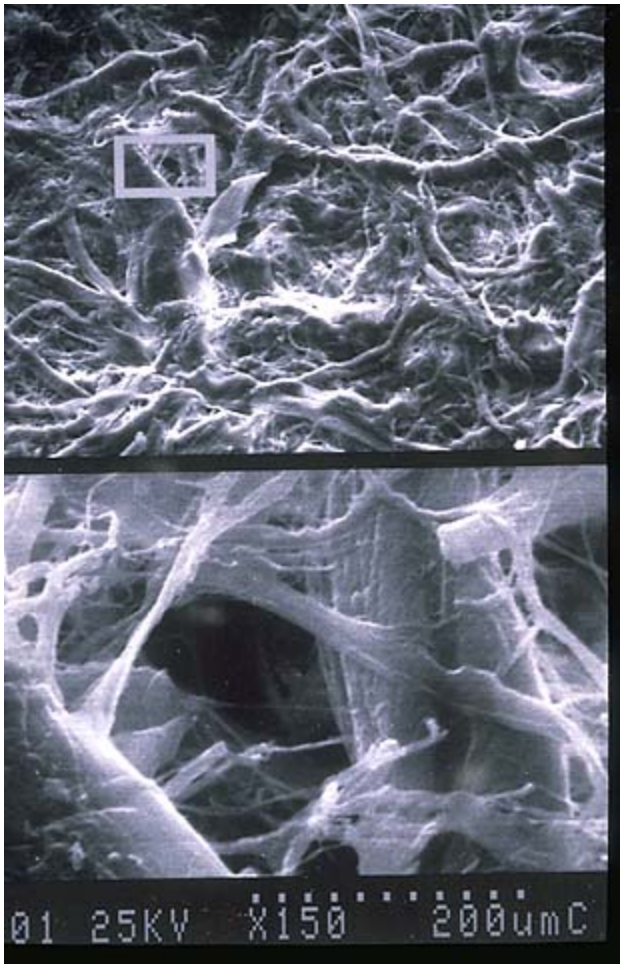

X = fiber fraction along x

Y = fiber fraction along y

Z = (1 - X - Y), equally along x and y

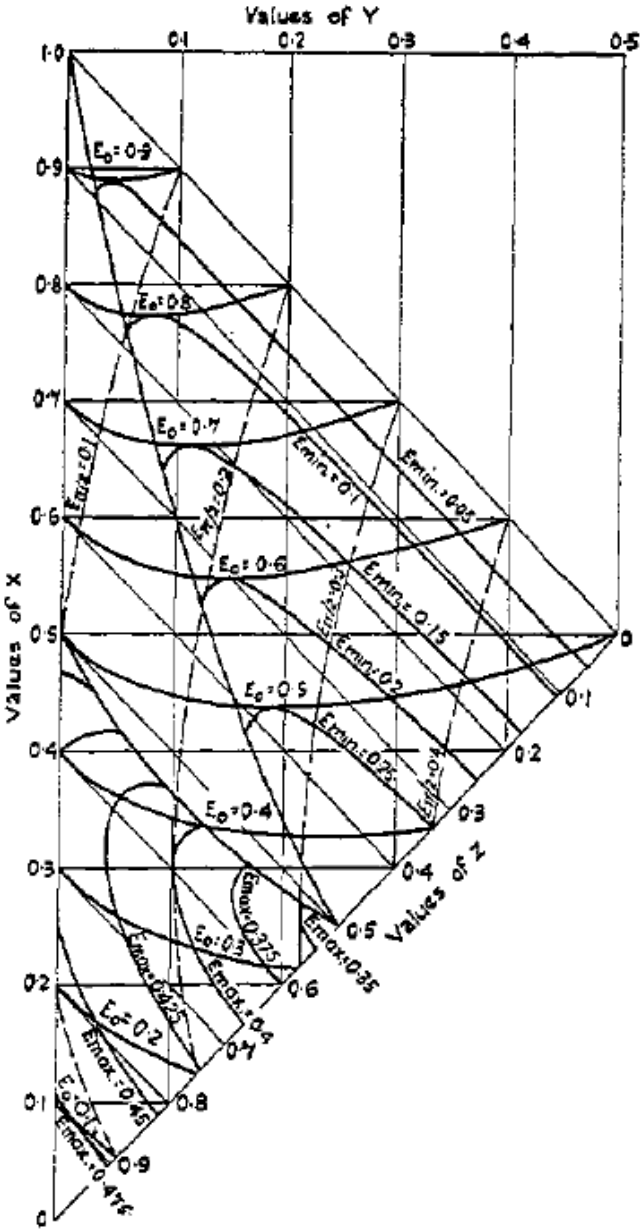

Fig. 1. Effect of fibre orientation on the principal values of Young's modulus

http://aic.stanford.edu/sg/bpg/annual/v15/bp15-17.html
Cox et al., British J. Appl. Phys 3:72 1952.

Mechanical network model: randomly placed beams

-Determine geometry using SEM/ TEM

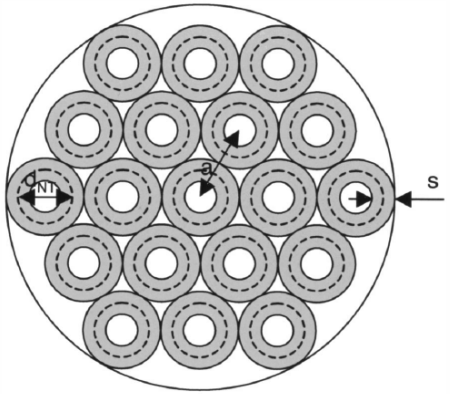

-Randomly lay beams
-Trim unit area
-Trim unconnected segments

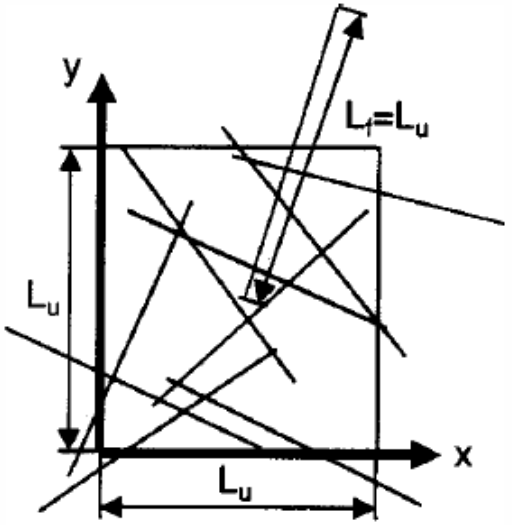

(a)

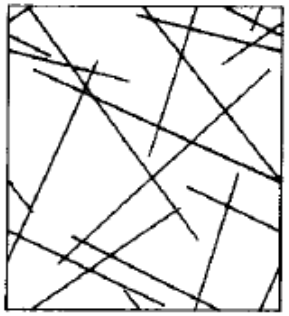

(b)

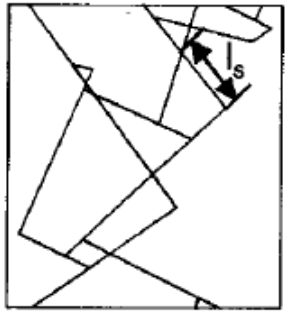

(c)

Mechanical model of a network

Key parameters (derived from distribution models):

- Total number of crossings per area

$$N_c = \frac{\left(N_f L_f\right)^2}{A\pi}$$

- Number of crossings per fiber

$$\bar{c} = \frac{2N_c}{N_f}$$

- Mean fiber length between crossings

$$\overline{L_s} = \frac{L_f}{\bar{c}}$$

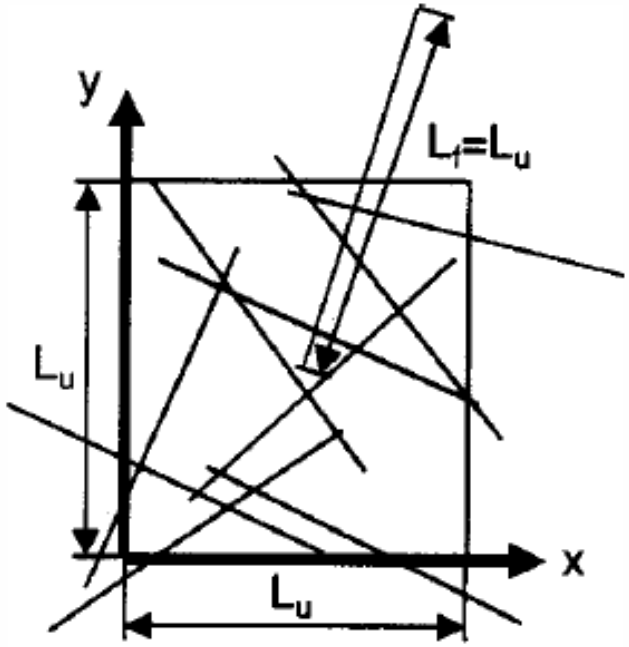

→ Must also consider fiber width

Berhan et al., *J. App. Phys.* 95(8):4335, 2004.

An exemplary joint model

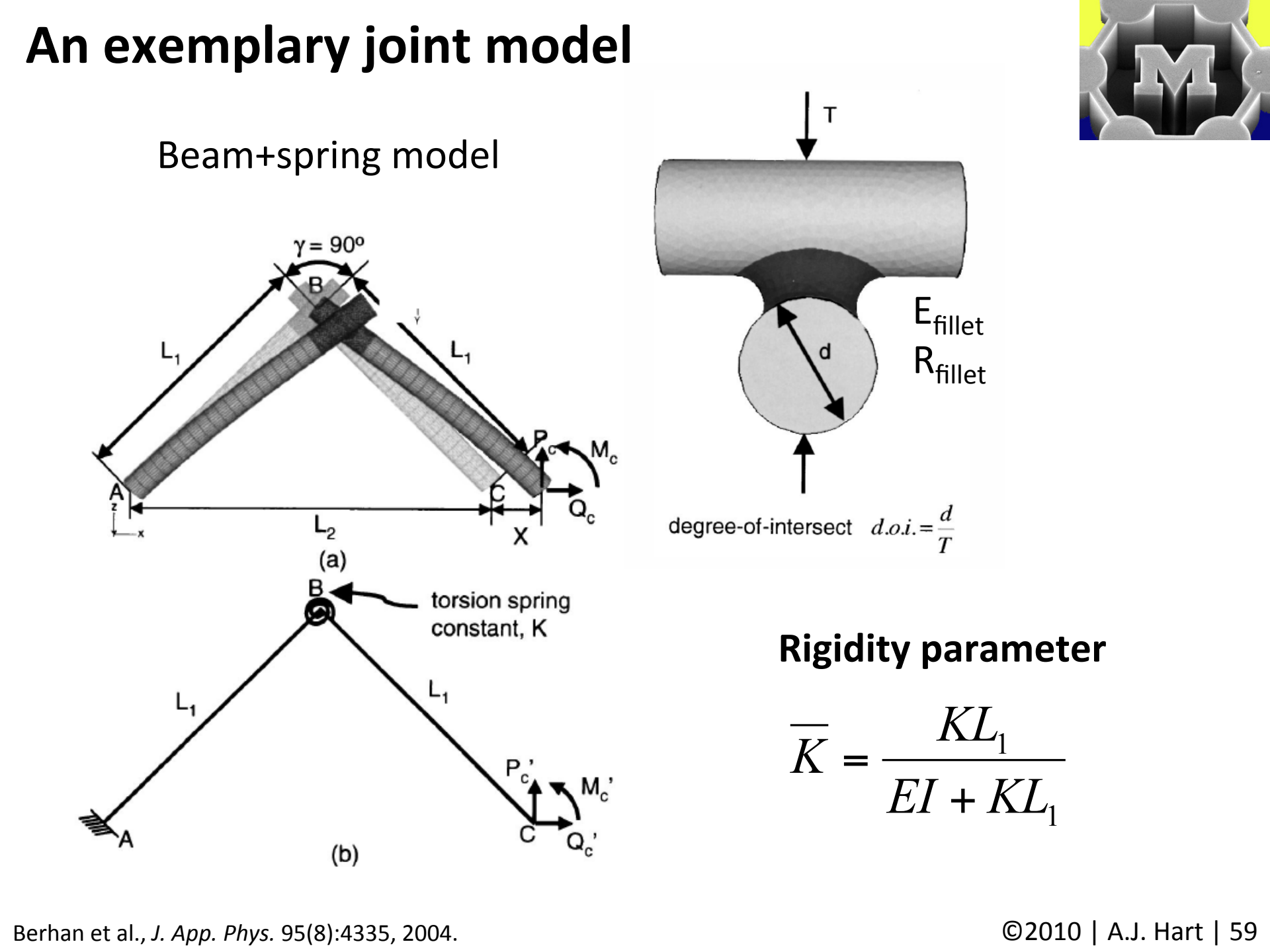

Beam+spring model

(a)

(b)

degree-of-intersect $d.o.i. = \frac{d}{T}$

Rigidity parameter

$$\overline{K} = \frac{KL_1}{EI + KL_1}$$

Berhan et al., *J. App. Phys.* 95(8):4335, 2004.

Tensile properties of CNT forests

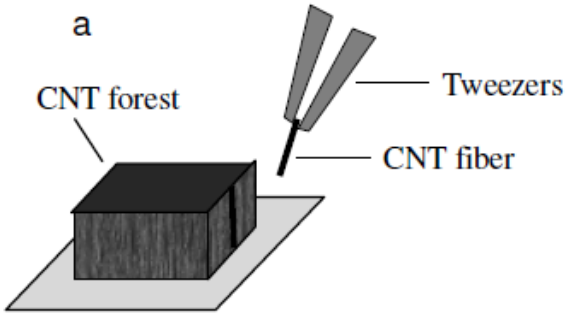

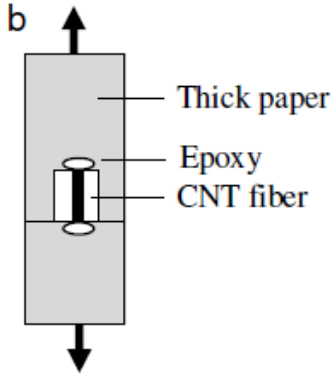

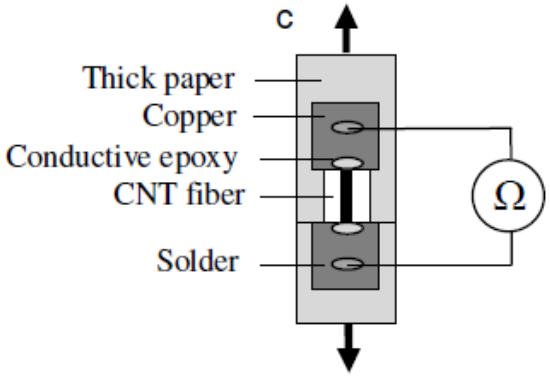

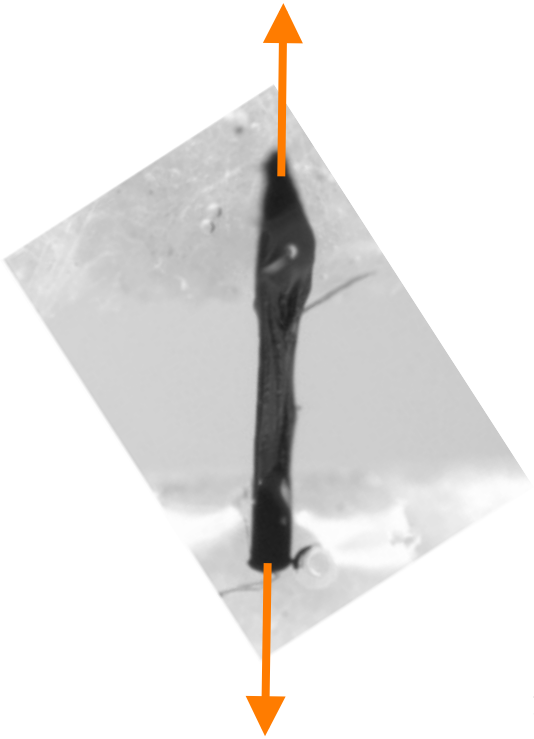

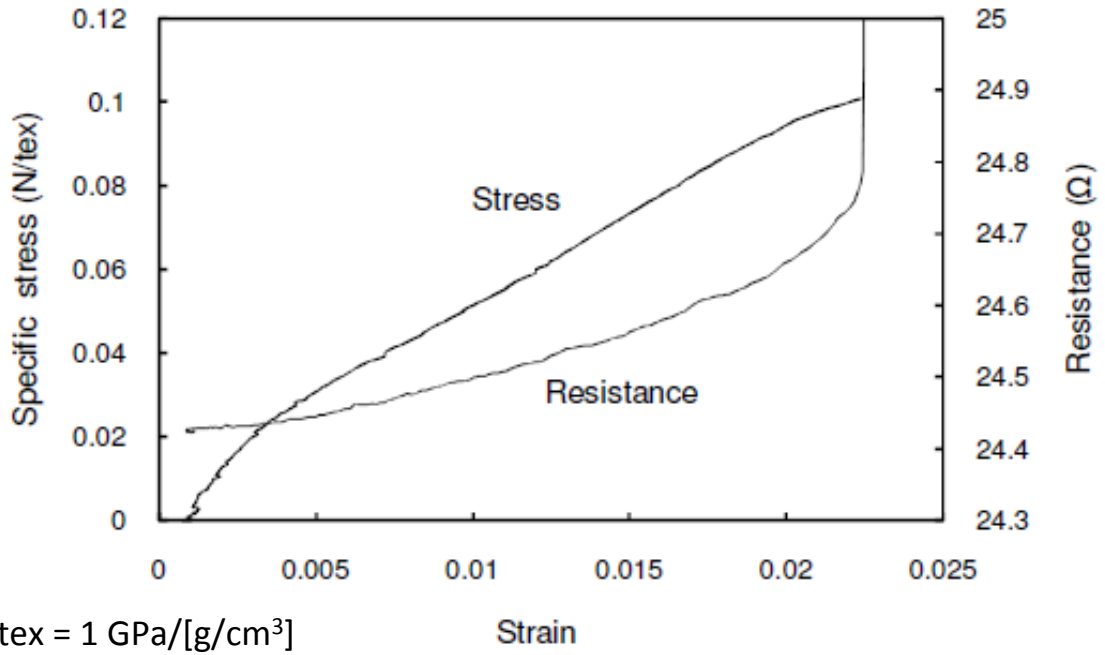

1 N/tex = 1 GPa/[g/cm^3]

Hill, Havel, Hart, Livermore. *J. Micromech. Microeng.* 19:094015, 2009; in press, 2010.

Mechanical properties of CNT yarns

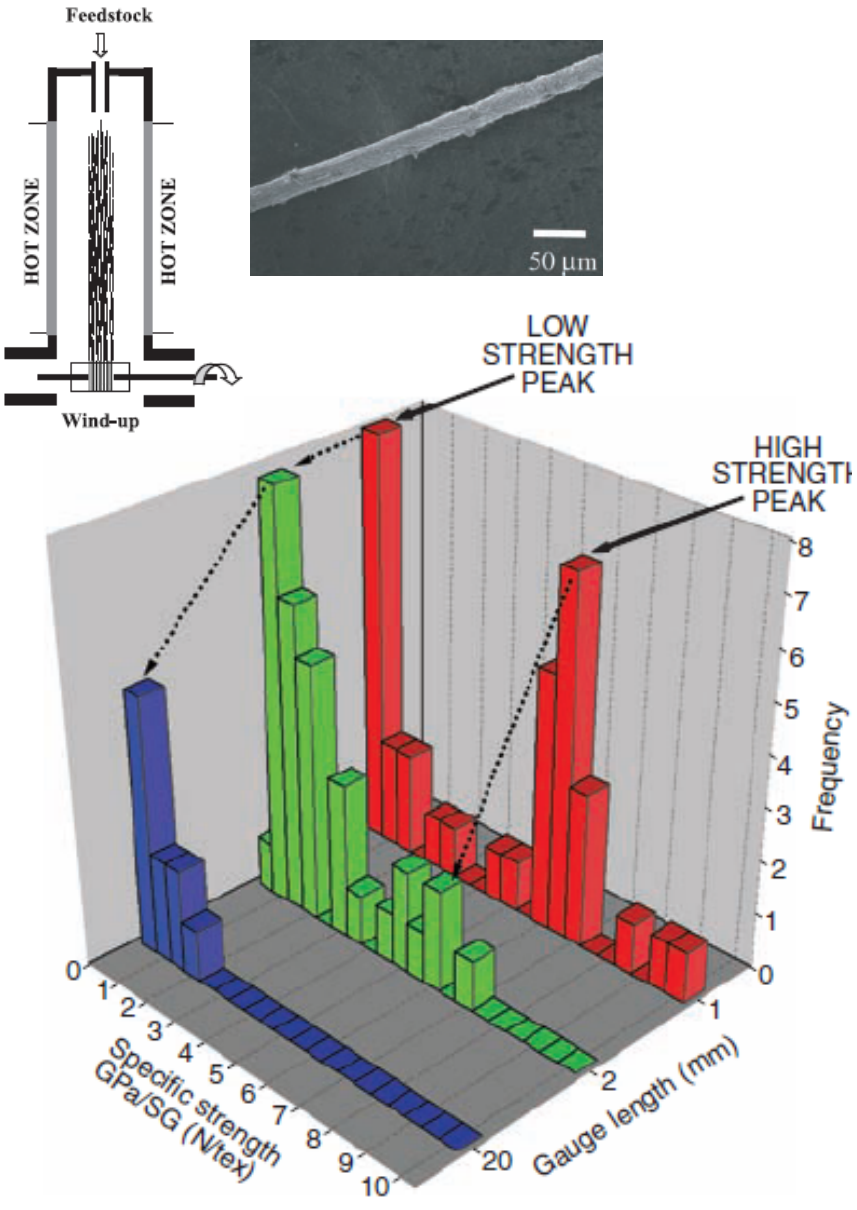

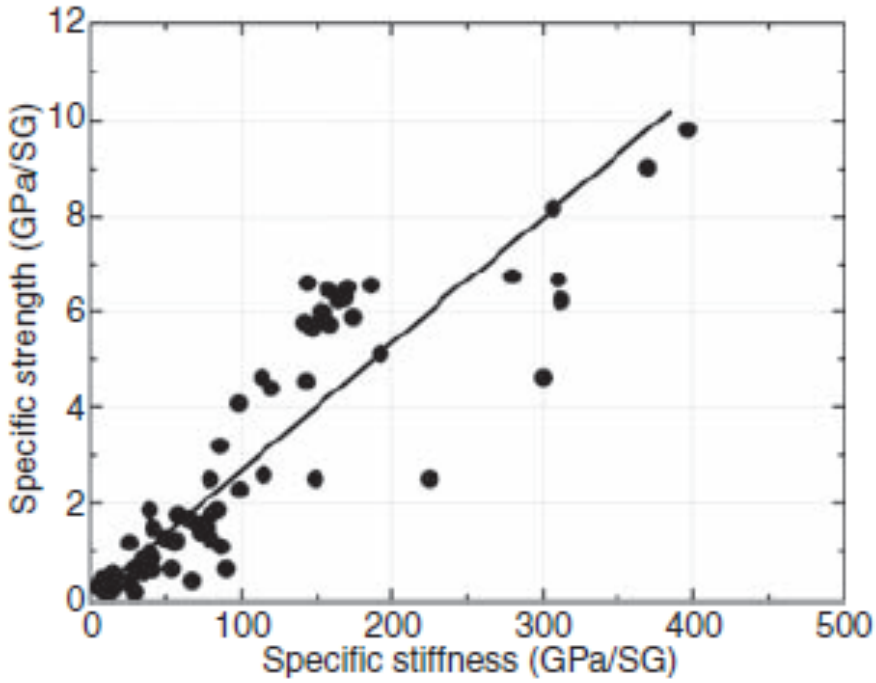

Koziol et al., *Science* 318:1892-1895, 2007.

Mechanical properties of CNT assemblies: real vs. ideal values

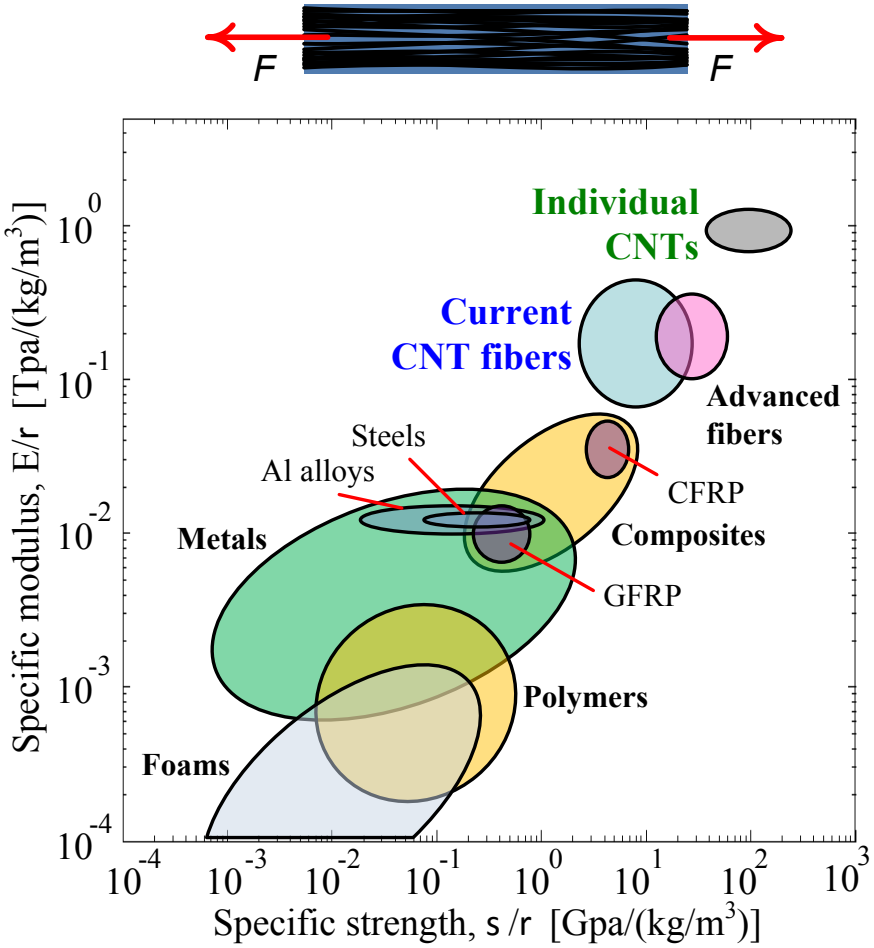

How to join structures individually?

→ *Process using electron/ion beams*

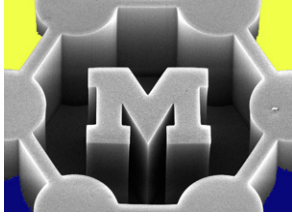

Advantages:

- Small (variable) spot size
- Rapid scanning (vs. probe techniques)

But possible damage mechanisms –remember, we are impinging upon nuclei and electrons

- Knock-on displacements (conductors) –ion beam displaces atom
- Bond breakage (insulators)

→ Balance between damage generation and healing depends on beam energy and temperature; must exceed threshold energy for desired atom displacement

→ See also: radiation damage, ion implantation, doping

A. Krasheninnikov et al.

Electron-beam induced damage

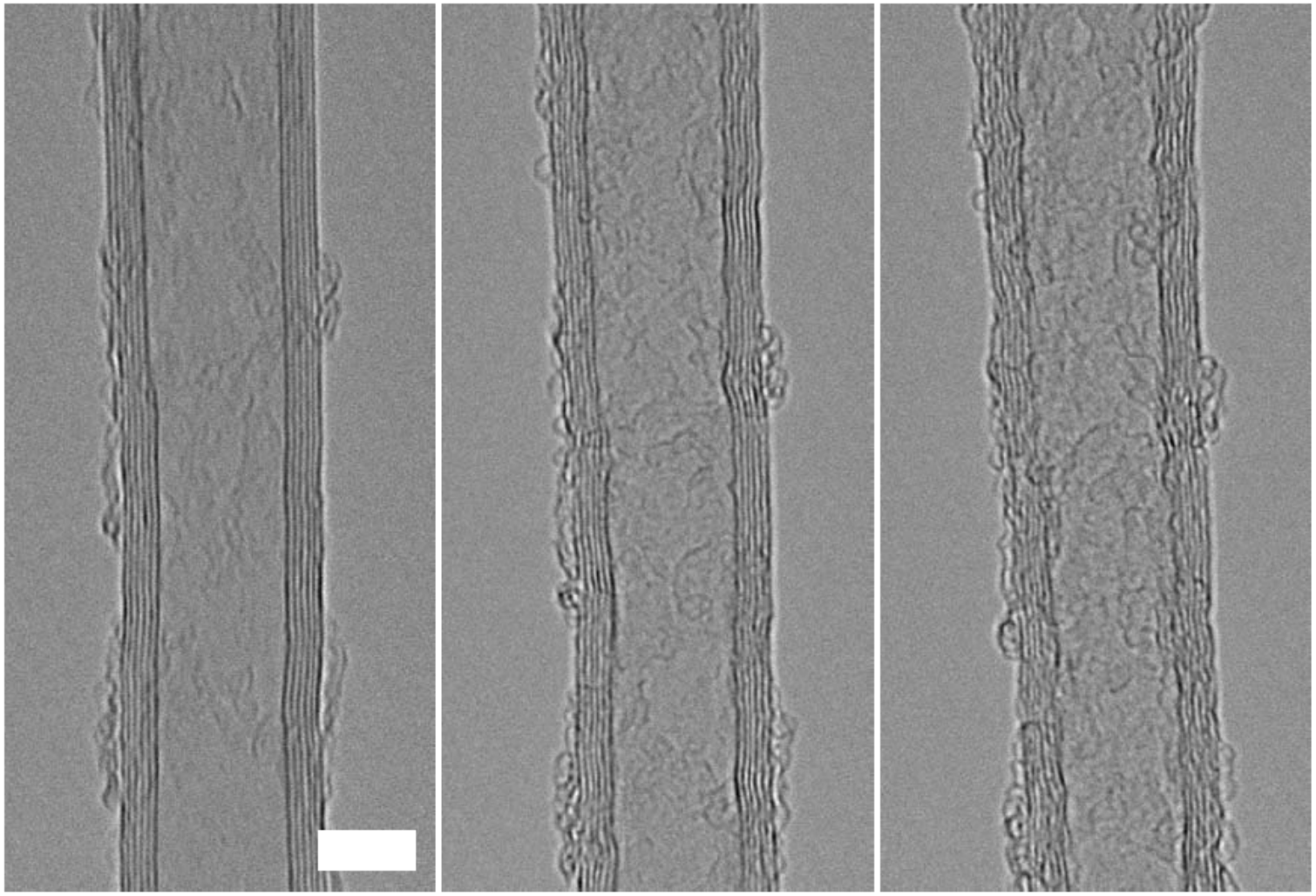

(a) $t = 10\,\mathrm{s}$ (b) $t = 30\,\mathrm{s}$ (c) $t = 180\,\mathrm{s}$

Defect generation and healing

Threshold energy (room temp ≈ 0.03 eV):

sp^2 carbon (graphene/CNT) = 15-20 eV

sp^3 carbon (diamond) = 30-50 eV

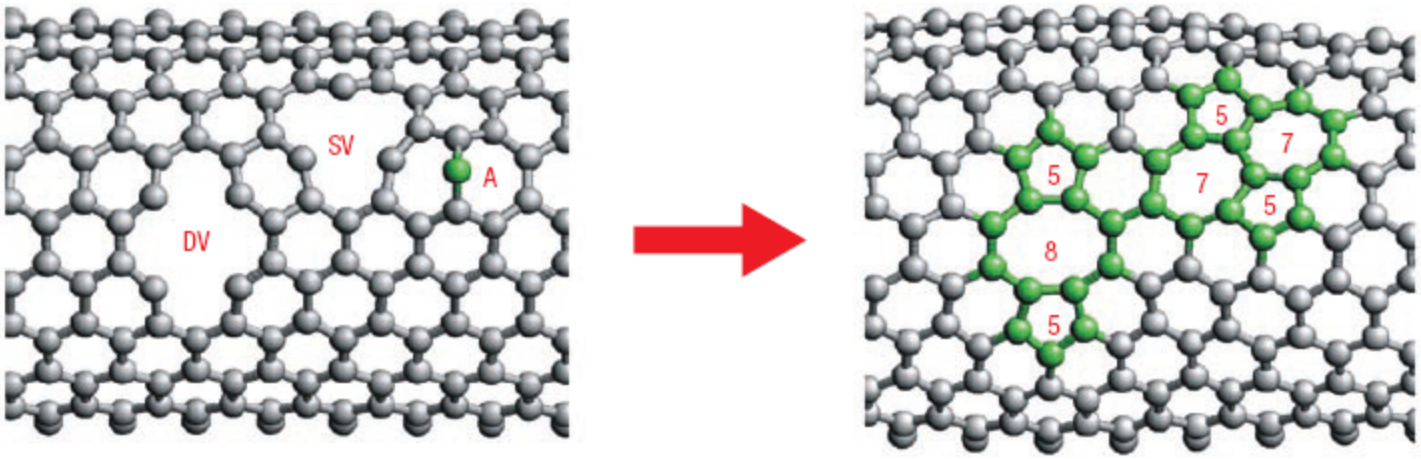

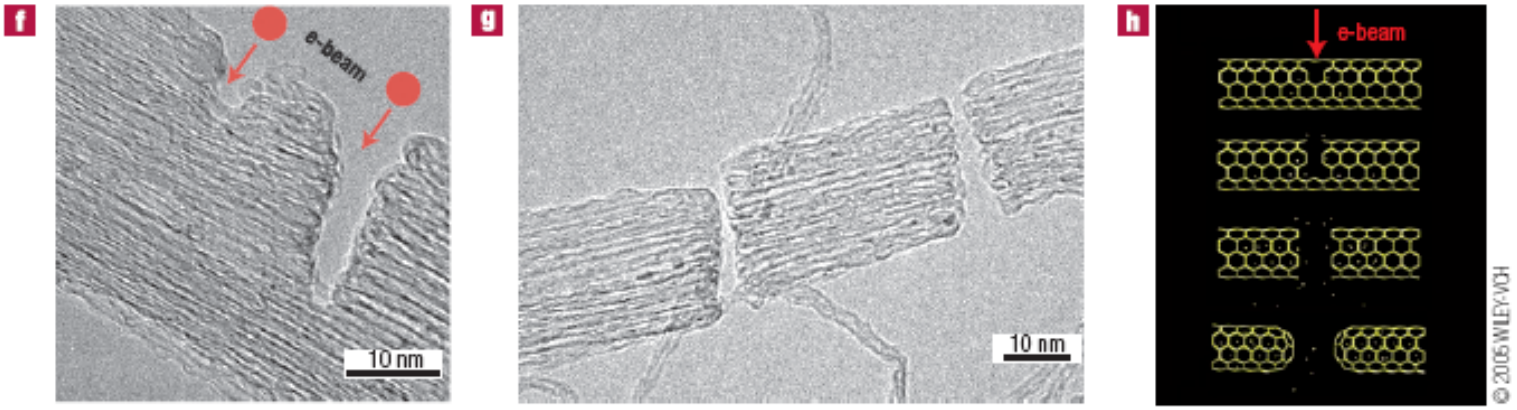

Cutting and healing of SWNT bundle ends

Welding of CNTs

Very high local temperatures

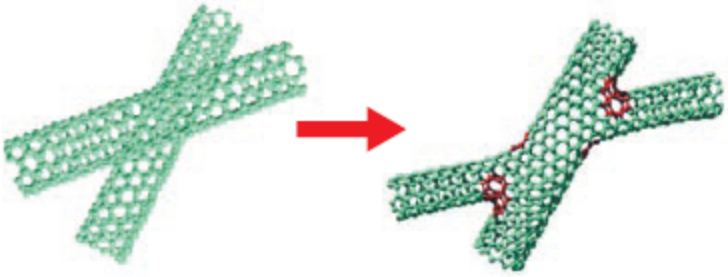

"Nanopants"

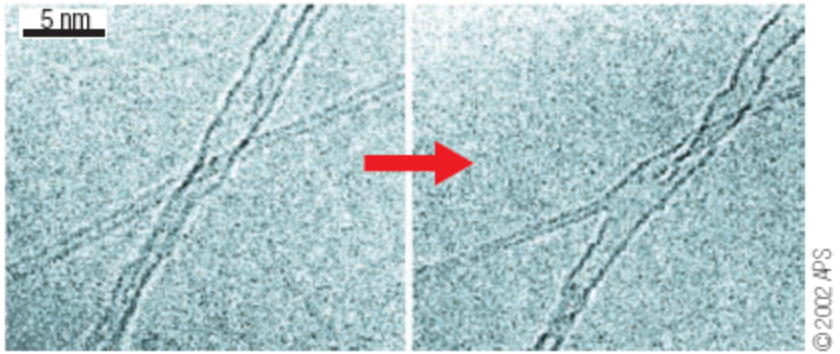

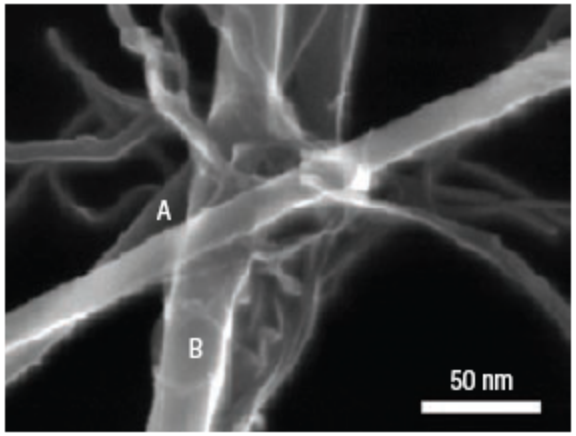

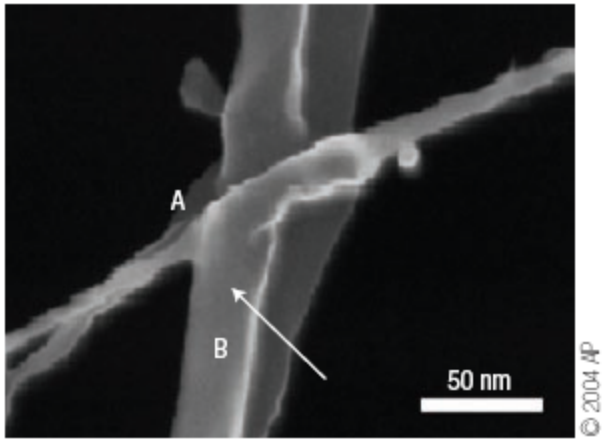

Welding using dopants: Boron crosslinks DWNTs

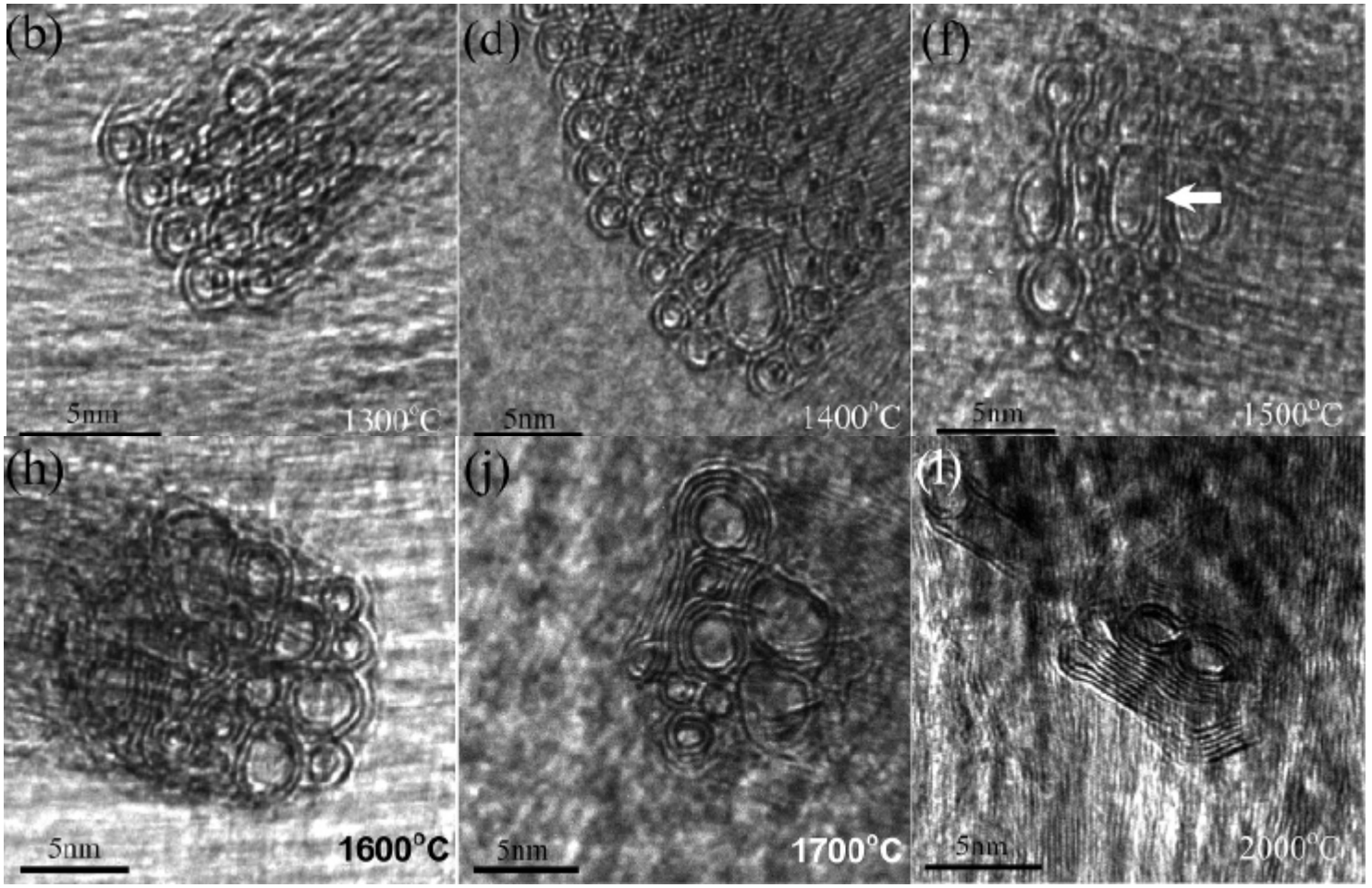

B is an electron acceptor, lowers Fermi level (highest occupied level)

Crosslinking creates C-B-C and BC_3 bridges

M. Endo et al., *Nano Letters* 5(6):1099-1105, 2005.

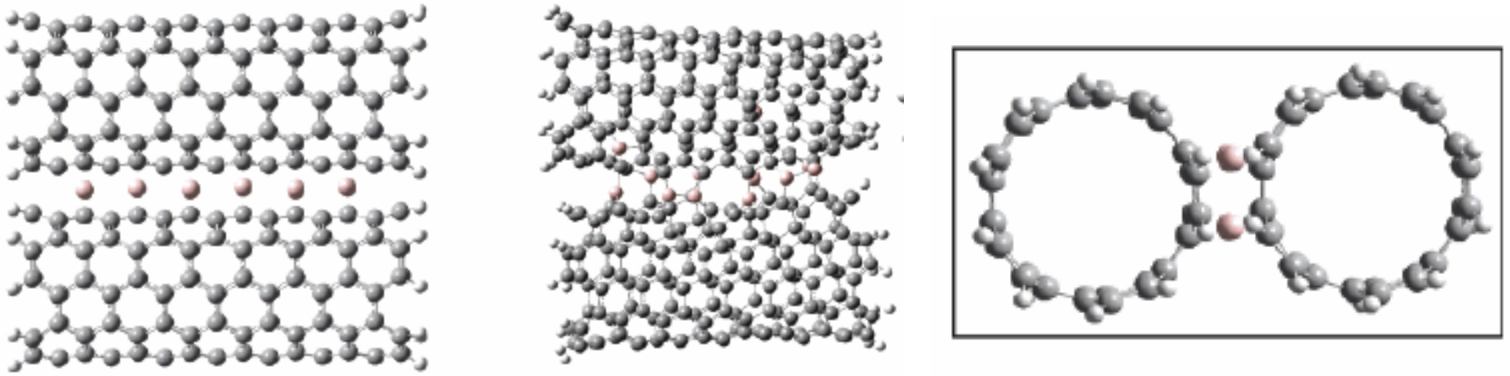

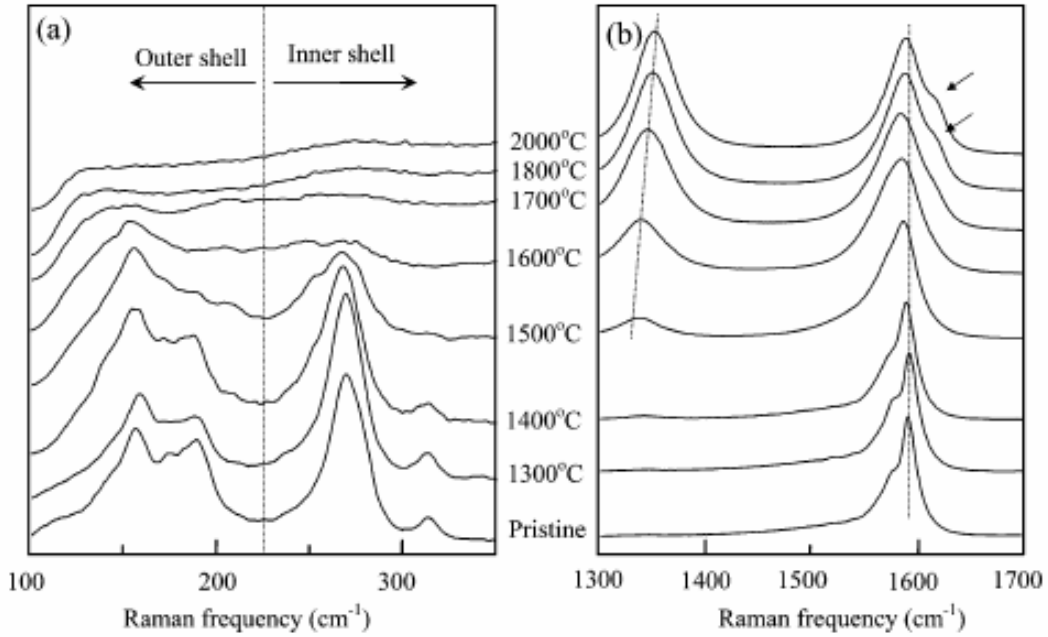

Figure 6. (a) Low-frequency and (b) high-frequency Raman spectra of B-DWNTs pristine and heat treated at temperatures ranging from 1300 to 2000 °C. The disappearance of the RBM frequency is a direct indicator of the destruction of the original DWNTs and the formation of diameter-enlarged DWNTs, MWNTs and graphitic material (see text).

M. Endo et al., *Nano Letters* 5(6):1099-1105, 2005.

Aligning networks by stretching

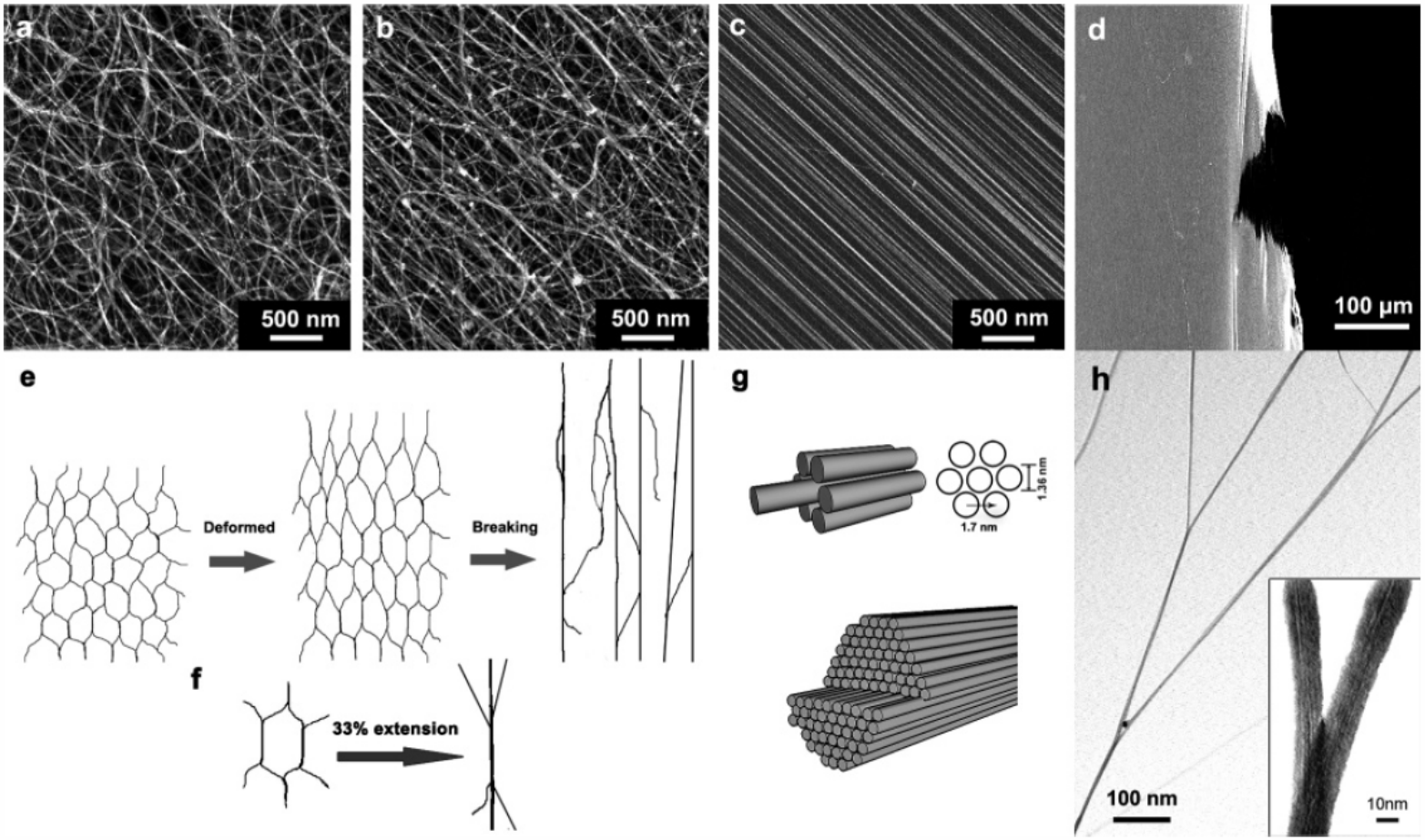

Figure 3. (a) SEM image of an unstrained film. (b) Typical SEM image of the film after 8−10% strain before broken. (c) SEM image at the breaking point. (d) Macroscopic SEM image near the breaking point. The film is going to be split. (e) Schematic diagram of the structure deformation process during extension. (f) Schematic diagram of one simplified mesh and its morphology after 33% extension. (g) Drawing a (10,10) SWNT from a (10,10) bundle (upper two images), and the interbundle slipping within a 17 nm wide (10, 10) shared bundle. It is easy to count out that the area of the slipping surface is about 10% of the total outer surface for the SWNTs in a semibundle. (h) Low-magnification TEM image for some typical stretched SWNT meshes.

Ma et al., *Nano Letters* 7(8):2307-2311, 2007.

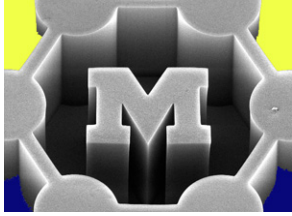

Extras

2D resistor model used to predict critical exponent

- Place sticks randomly in 2D field
- Percolation occurs when both contact electrodes are in the same cluster
- Create geometric model and then reduce lengths to find threshold length

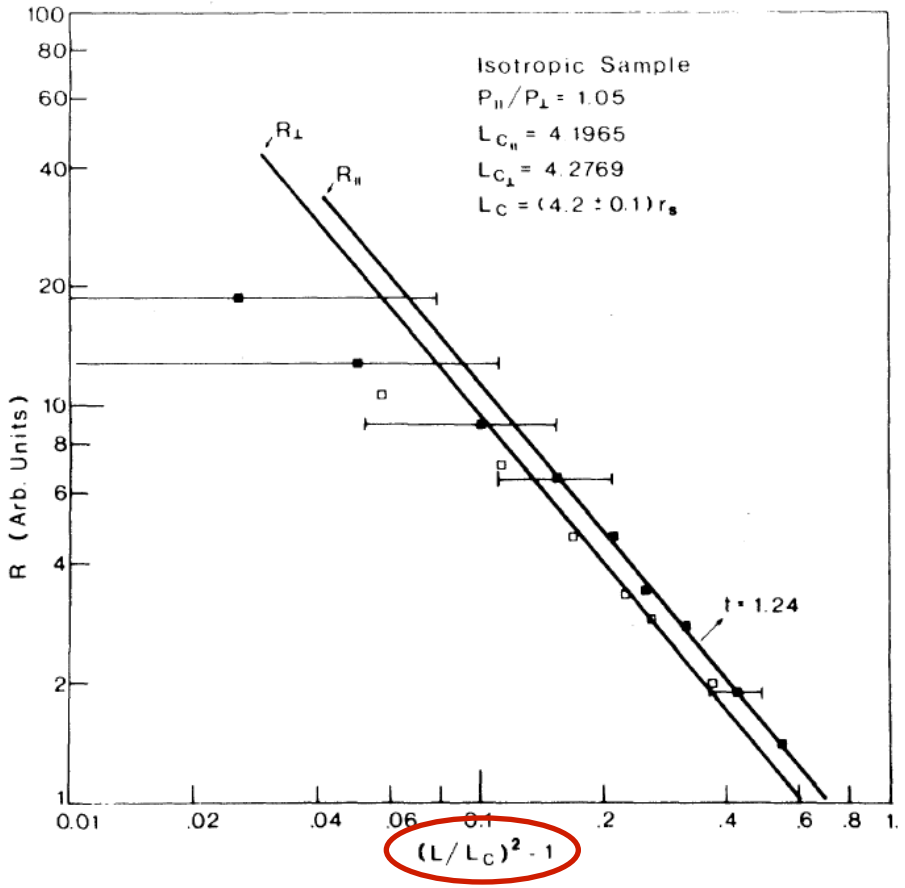

FIG. 2. The longitudinal and transverse resistance of a two-dimensional system of 1000 sticks as a function of the stick-length variable parameter $(L/L_c)^2 - 1$. These results have been found for one of the seeds. The horizontal "error bars" indicate the regions of the graph to which the results of three other seed (samples) are confined.

Balberg et al., *Physical Review Letters* 51(18):1605, 1983.

Excluded volume method of calculating the percolation threshold

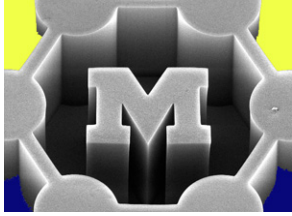

- **Excluded volume:** Area that another object cannot enter if overlapping of objects is avoided

- "Universal" percolation for circles and spheres

$$N_c a = const$$
$$N_c v = const$$

What are values for circles and spheres?

…but orientation effects must be considered for non-round (high aspect ratio) objects

Balberg et al., *Phys Rev B* 30(7):3933, 1984.

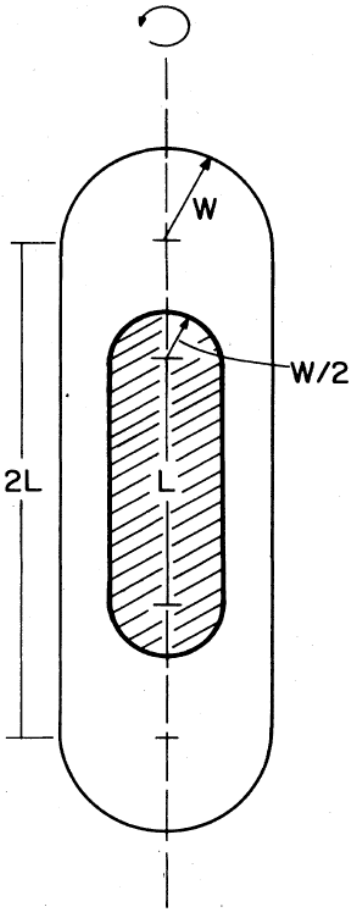

FIG. 4. Capped rectangle and the corresponding excluded area which is obtained with $\theta=0$. In three dimensions the stick is a capped cylinder and so is the excluded volume. Both the stick and the excluded volume are obtained by rotating the two-dimensional figure around the axis shown.

$$\langle V\rangle=(4\pi/3)W^3+2\pi W^2L+2WL^2\langle\sin\gamma\rangle_\mu\,, \qquad (24)$$

- Average over angular distribution
- If aligned, behave like spheres
- For random orientation,

$\langle\sin\gamma\rangle_\mu$ = pi/4

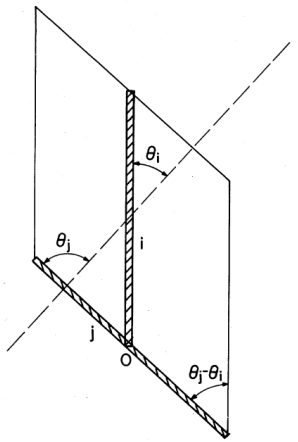

FIG. 1. Two "widthless" sticks (shaded area) and their corresponding excluded area. This area is the parallelogram which is obtained by following the center 0 of the stick j as it travels around the stick i while being parallel to itself and touching stick i at a single point.

Balberg et al., *Phys Rev B* 30(7):3933, 1984.

Comparison of excluded volume theory to experiments

Exfoliated graphite in polymer matrix; model as discs; oriented

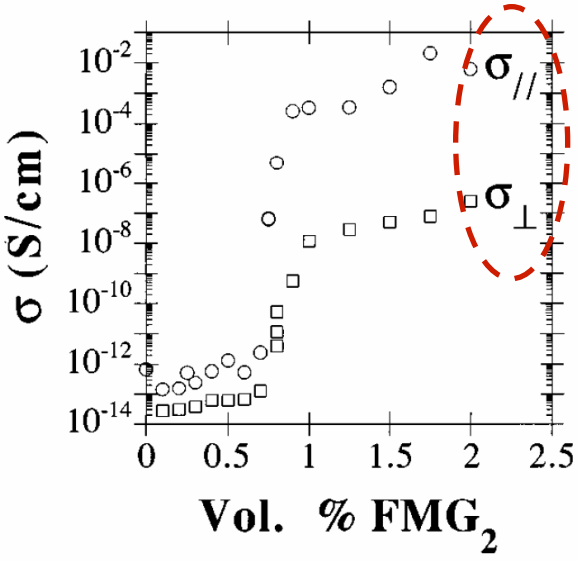

FIG. 1. Experimentally determined curves of conductivity $\sigma(\phi)$ for a polyurethane-FMG_2 composite.

Critical concentration $\phi_c \propto \frac{t}{r}$.

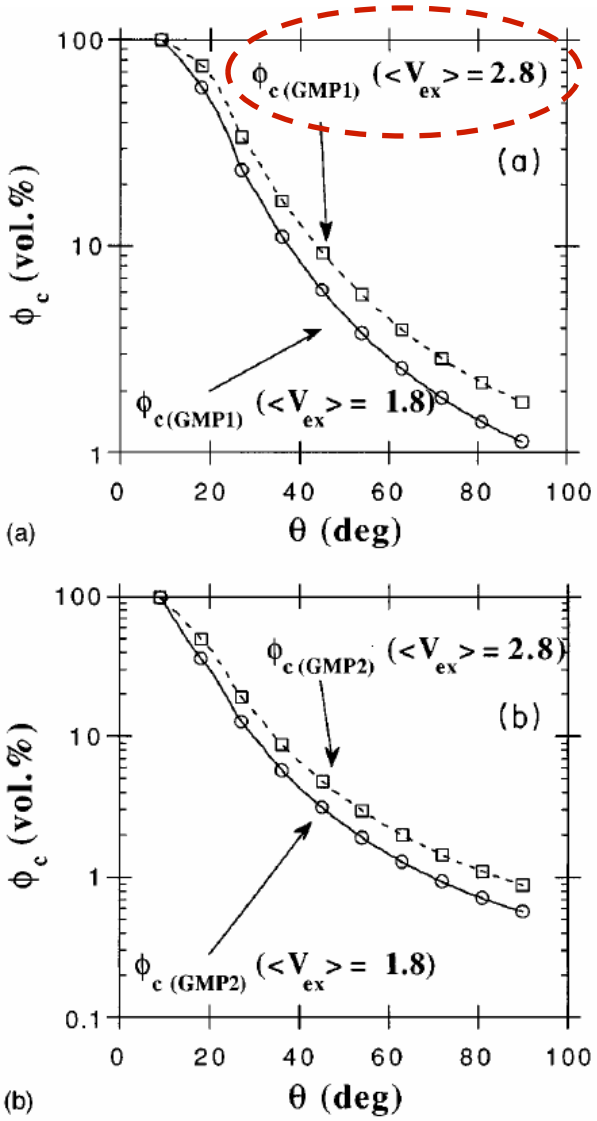

Maximum angle between disks

FIG. 2. Critical concentration calculated for a system of disk-shaped particles of 10 μm diameter and thickness (a) 0.1 μm and (b) 0.05 μm (corresponding, respectively, to fillers FMG_1 and FMG_2) as a function of θ, the maximum angular orientation between the disks. The calculation uses the two extreme values of 1.8 and 2.8 for the total excluded volume $\langle V_{ex} \rangle$.

Celzard et al., *Phys Rev B* 53(10):6209 1996.

Carbon fibers (long cylinders) in polymer matrix

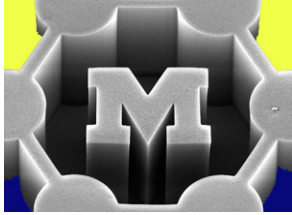

TABLE III. Critical concentrations for indicated particles dispersed in a polymer matrix determined experimentally (indicated reference) and calculated here based on concept of excluded volume.

Case	Particles	Diameter	Length	ϕ_c (vol %)	Calculated ϕ_c	Reference
1	Elongated carbon black aggregates	≈800 Å	≈5000 Å	7.2	$7.00 \leqslant \phi_c \leqslant 13.51$	17
2	Carbon fibers	10 μm	1 mm	0.52; 0.69; 0.72; 0.71; 0.86; 0.93; 1.1	$0.67 \leqslant \phi_c \leqslant 1.35$	18
3	Carbon fibers	10 μm	1.15 mm	1.4; 1.47; 1.55	$0.59 \leqslant \phi_c \leqslant 1.18$	19
4	Carbon fibers	10 μm	2.85 mm	0.24; 0.25; 0.265	$0.24 \leqslant \phi_c \leqslant 0.48$	19
5	Carbon fibers	8 μm	1 mm	0.98	$0.54 \leqslant \phi_c \leqslant 1.08$	20
6	Carbon fibers	10 μm	1.1 mm	3	$0.62 \leqslant \phi_c \leqslant 1.23$	21
7	Carbon fibers	8 μm	1 mm	0.90	$0.54 \leqslant \phi_c \leqslant 1.08$	22

Celzard et al., *Phys Rev B* 53(10):6209 1996.

Vacuum-filtered CNT films at different densities

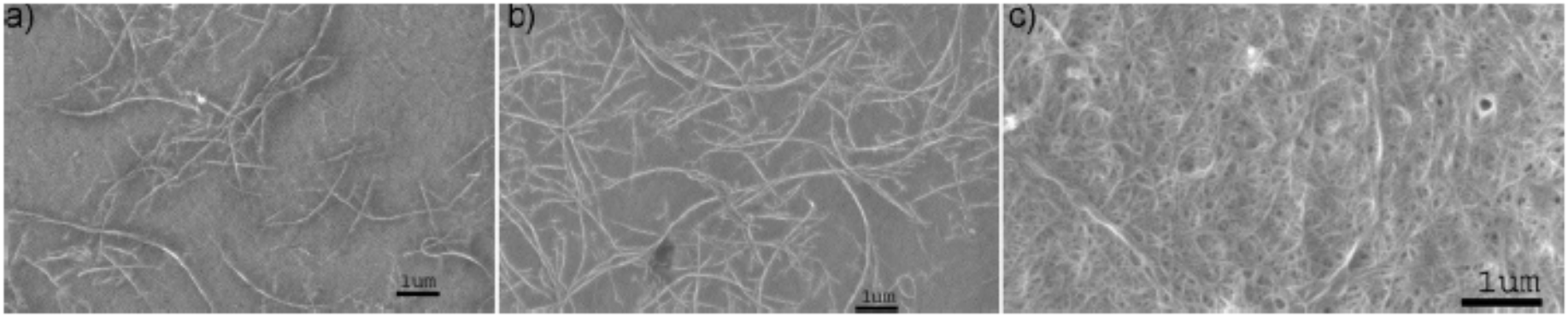

Figure 1. SEM images of the NTNs on alumina substrates, taken at 1.5 kV and 5 μA emission current. (a) Network resulting from filtering 7 mL of NT solution through the membrane. The filter pores are not visible in the scale shown. The network is near the percolation threshold and has few or no percolative paths through the sample. (b) 10 mL of NT solution for this sample. The network is above the percolation threshold and has several parallel pathways, allowing conduction across the film. (c) Film resulting from 400 mL of solution. Film is several layers thick.

Hu et al., *Nano Letters* 4(12);2513, 2004.

Conductivity

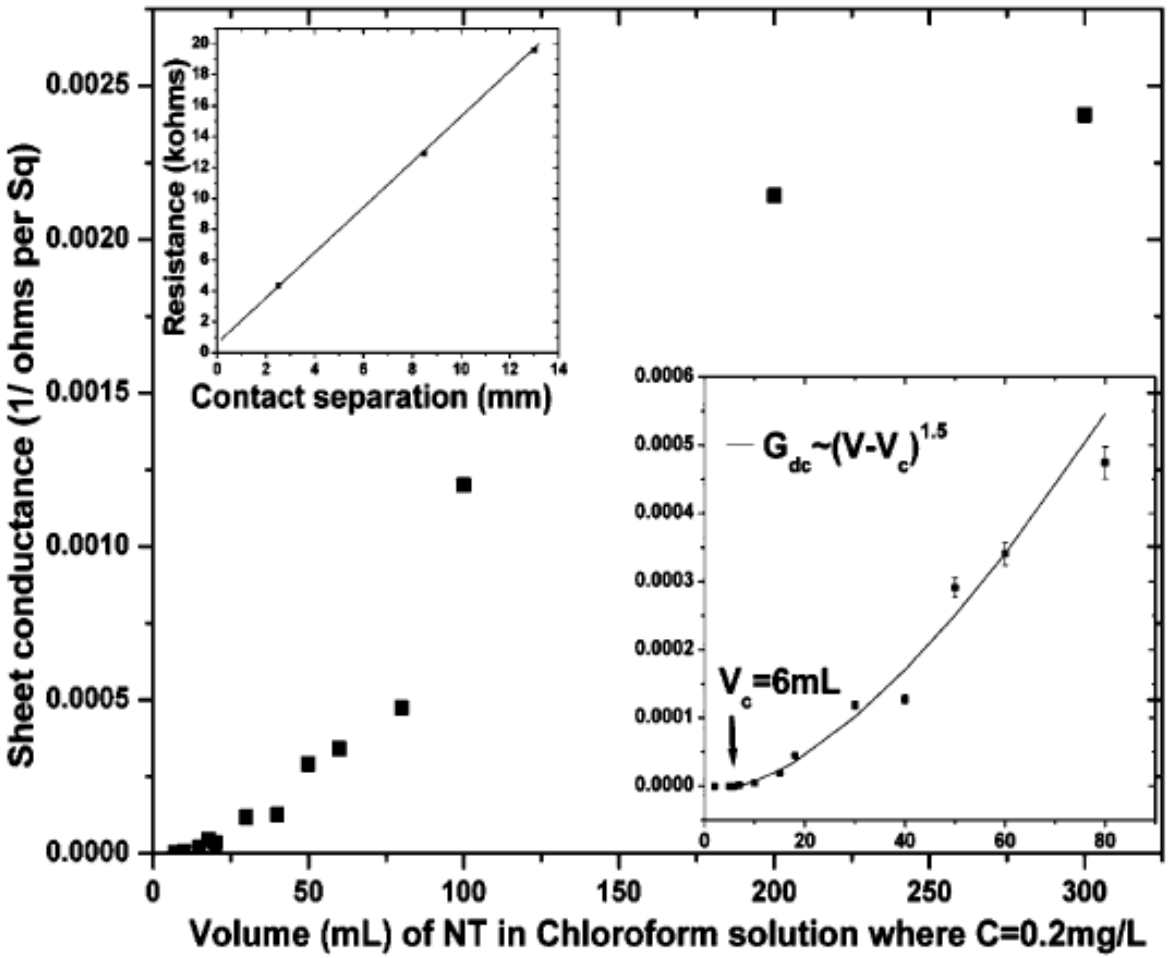

Dimensionality and nature of contacts within network (M/M vs. M/SC → schottky barrier) determine how fast conductivity increases with density

("critical exponent")

Figure 2. Sheet conductance vs volume of NT in chloroform solution. Notice the onset of conduction when the first percolative path across the sample is formed, indicated by $V_c = 6$ mL on the lower right inset. This inset shows the power fit in the percolation region, where the critical exponent $\alpha = 1.5$. Outside of the percolation region one starts to enter a linear regime. The inset in the upper left is the measured network resistance versus the source–drain distance, for networks of the same density.

Hu et al., *Nano Letters* 4(12);2513, 2004.

Co-filter SWNT & ***sacrificial*** **nano-particles** to membrane surface forming, **intimately mixed**, nanotube/nano-particle **composite** film.

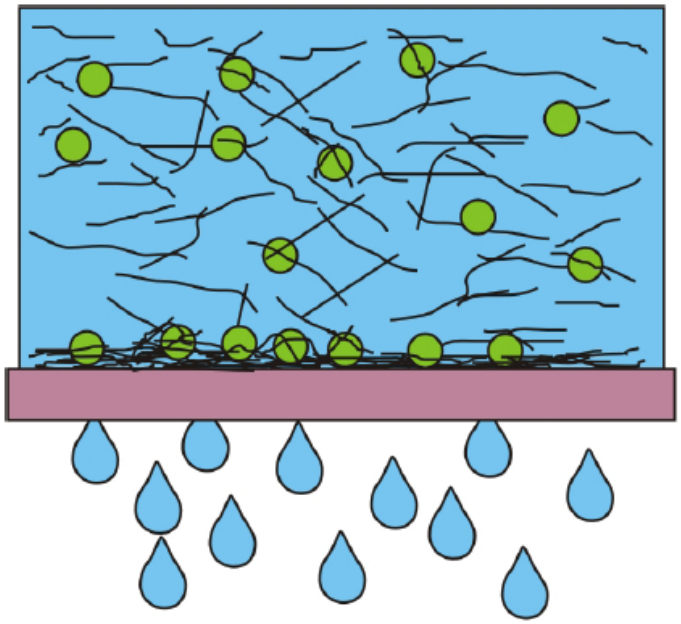

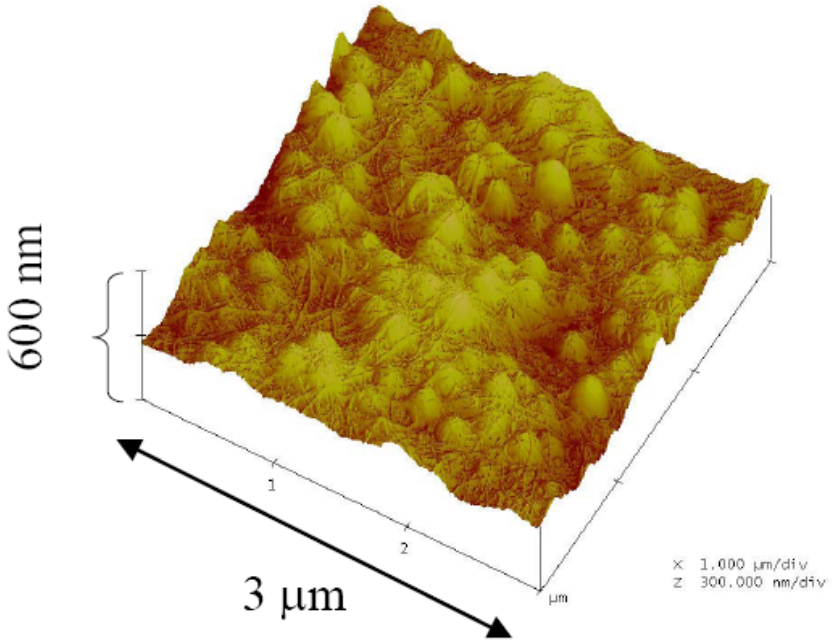

Subsequently **remove** sacrificial nano-particles.

A. Rinzler.

Nano-sphere removal is **easy**.

Polystyrene dissolves in acetone, the same solvent used to dissolve the MCE filtration membrane.

Nano-sphere dissolution occurs **during** film **transfer** to **substrate**.

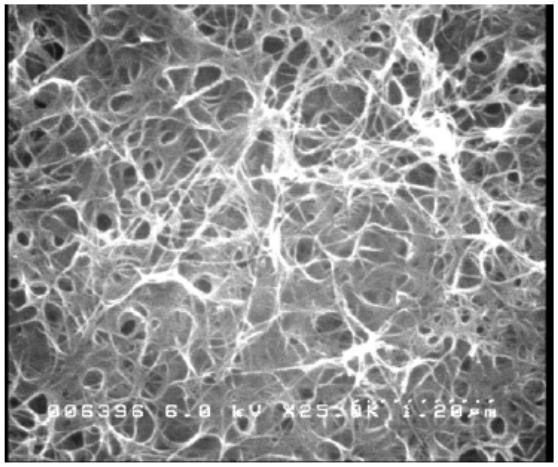

Standard

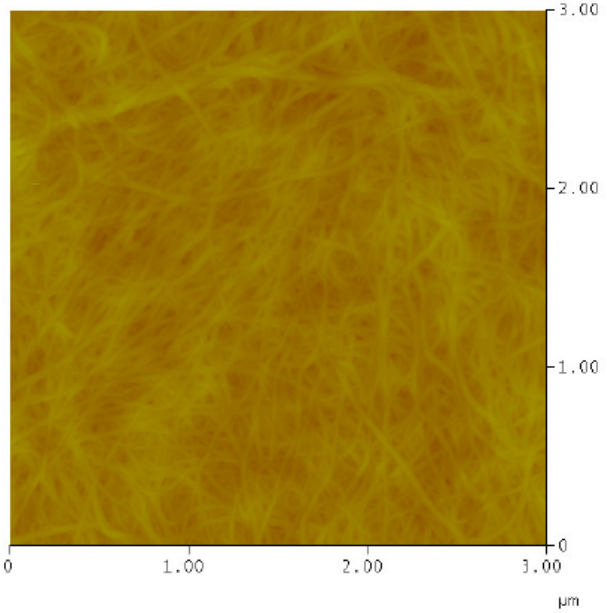

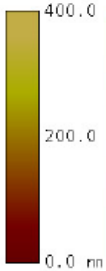

Porous

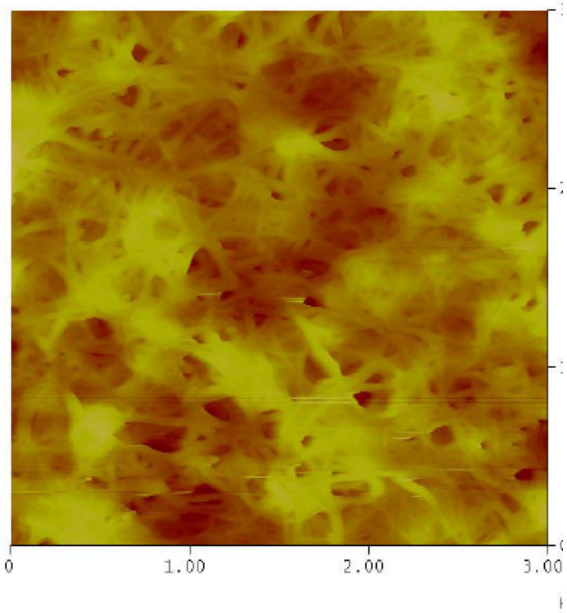

A. Rinzler.

CNT-based memory (Nantero, Inc.)

The concept (1998)

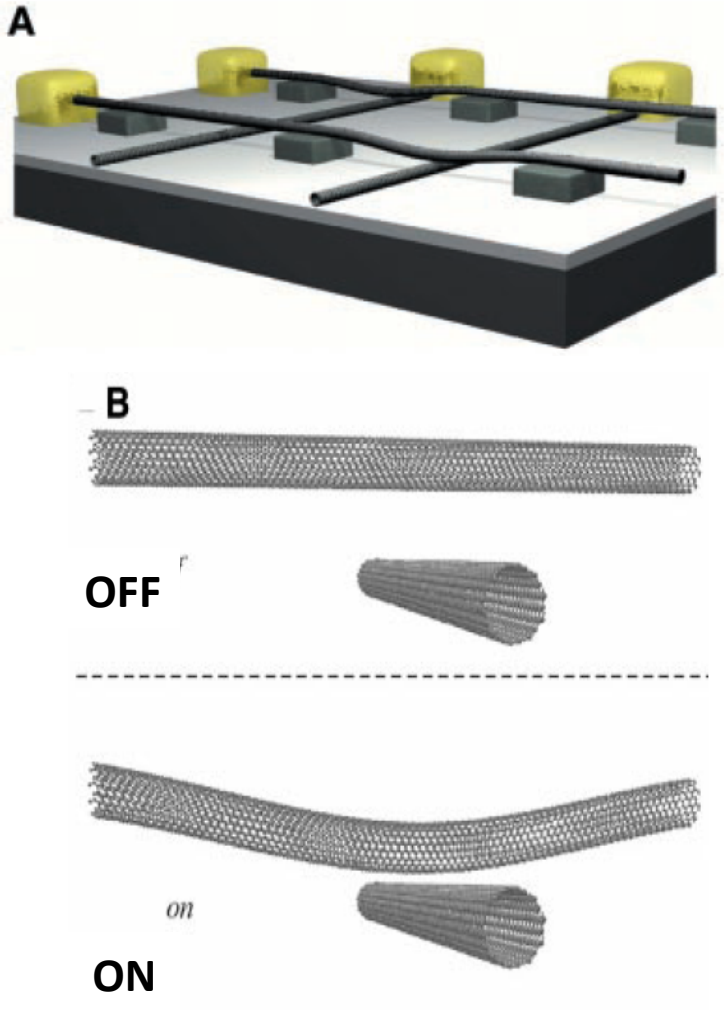

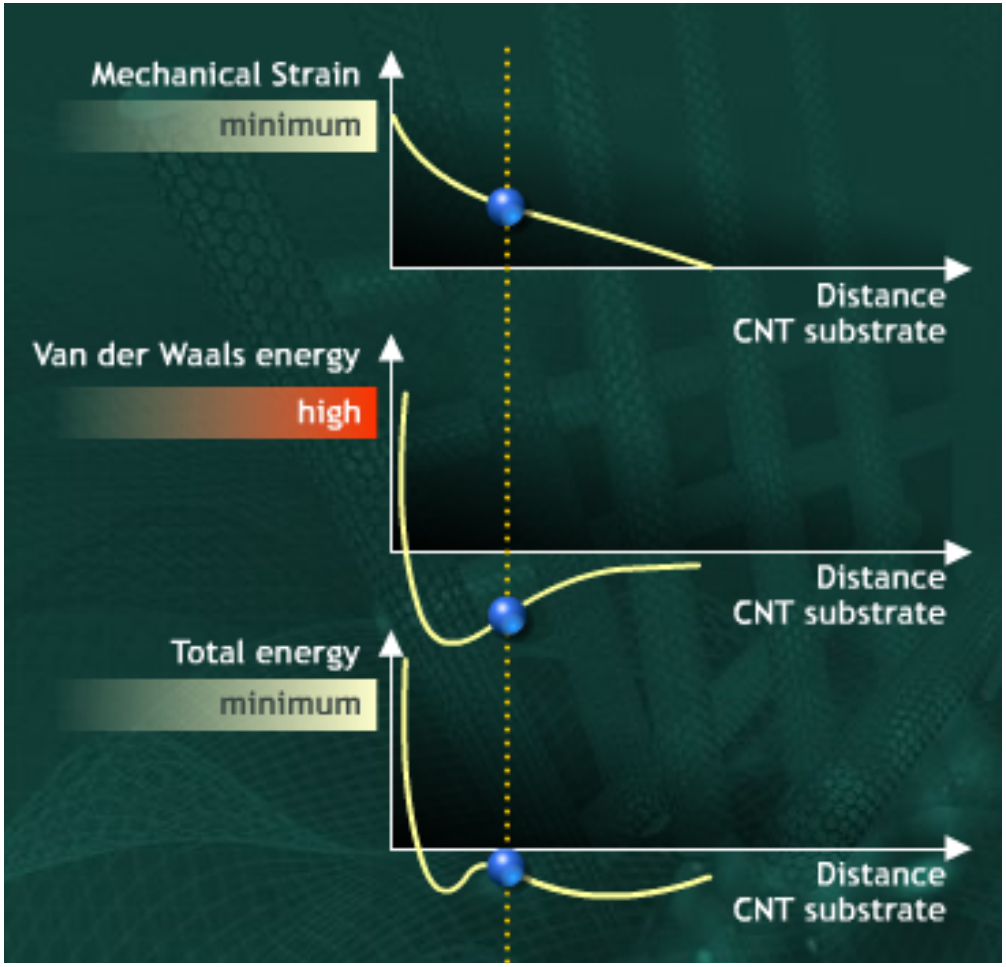

Reversible electromechanical junction

Rueckes et al, *Science* 289, 2000; http://www.nantero.com

Percolation in dye-sensitized solar cells

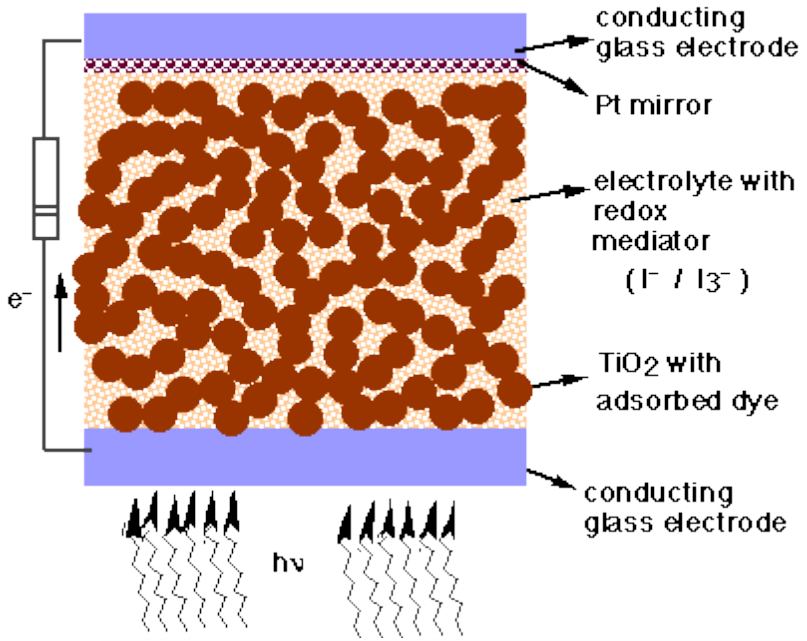

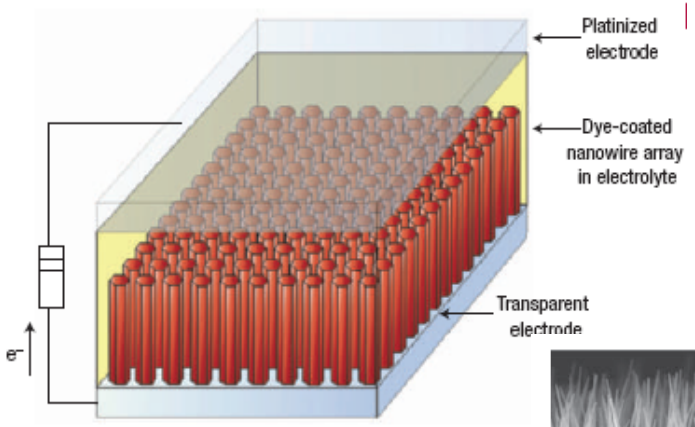

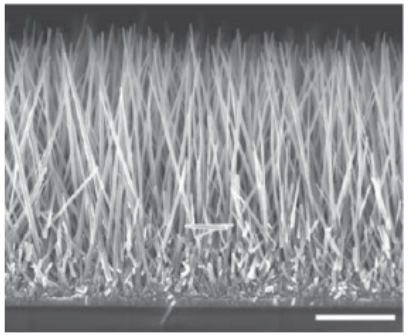

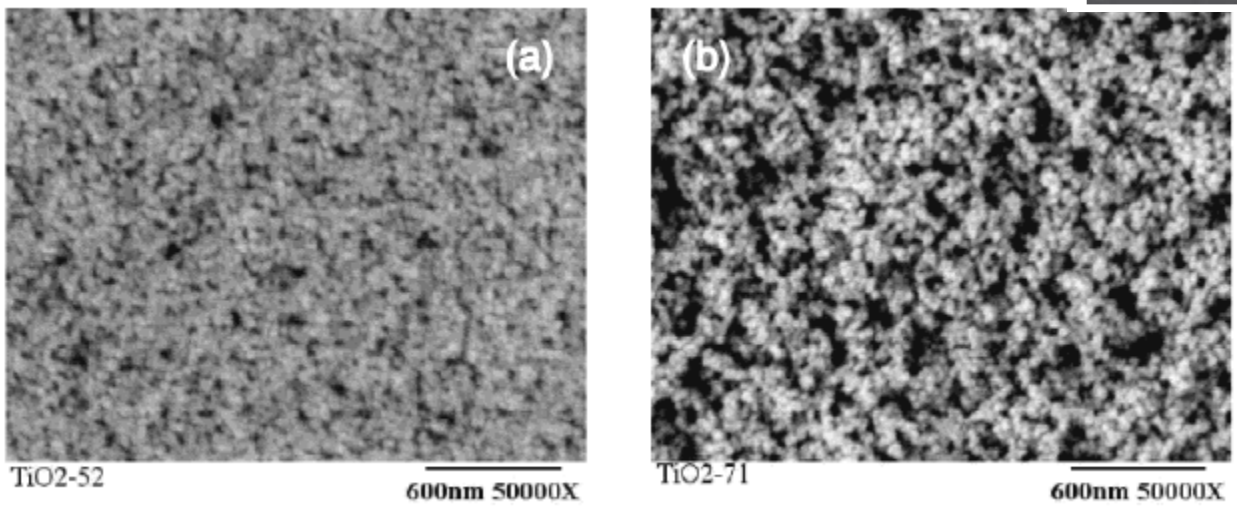

Figure 1. Plain-view SEM micrographs of (a) 52% and (b) 71% porous TiO_2 films.

Benkstein et al., JPCB 107:7759-7767, 2003.

Percolation in dye-sensitized solar cells

Simulation

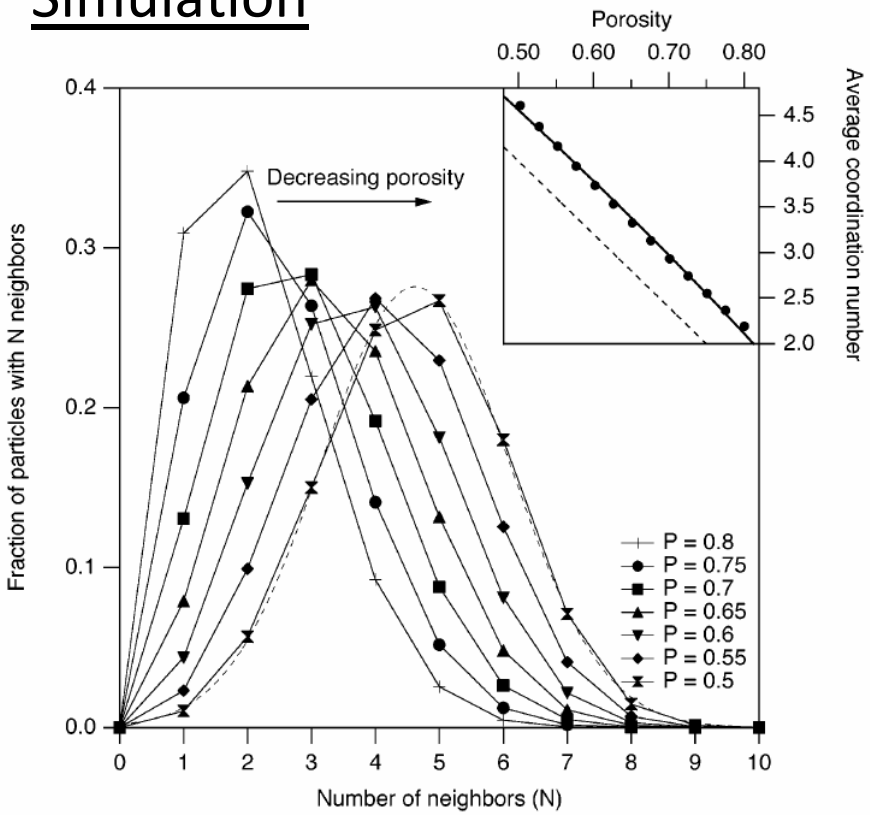

Figure 2. Dependence of the distribution of particle coordination numbers of simulated TiO_2 films on porosity. The dashed line represents a Gaussian fit of the data at $P = 0.5$. The inset shows the average coordination number as a function of film porosity. The dashed line in the inset depicts the predicted plot for a homogeneous distribution of particles based on the relation: $(CN = 8\ (1 - P))$. The solid line is a fit to a power-law variation of this relation: $CN = A\ (1 - P)^y$, where the values of the fit parameters are $A = 8.16$ and $y = 0.839$.

Simulation vs. experiment

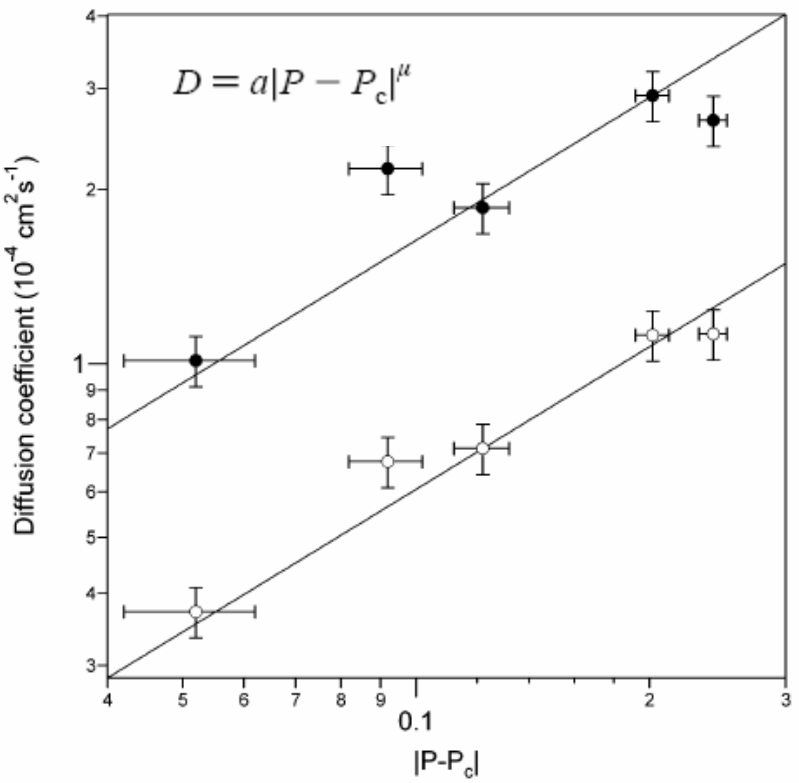

Figure 5. Comparison of the porosity dependence of the diffusion coefficient between the simulations and the measurements for a photocharge density of 10^{17} cm^{-3} for two redox electrolytes in methoxypropionitrile: ● 0.8 M tetrabutylammonium iodide (TBAI) and 0.05 M I_2 and ○ = 0.8 M 1-hexyl-2,3-dimethylimidazolium iodide (C6DMII) and 0.05 M I_2. P_c was taken equal to the value obtained from the fits of eq 5 to the simulation data (Figure 3). Solid lines are fits to eq 5 for fixed values of $P_c = 0.76$ and $\gamma = 0.81$ as determined from Figure 3 but with different prefactors for the redox electrolytes.

Benkstein et al., JPCB 107:7759-7767, 2003.

Percolation in dye-sensitized solar cells

Statistical spread of cluster radii

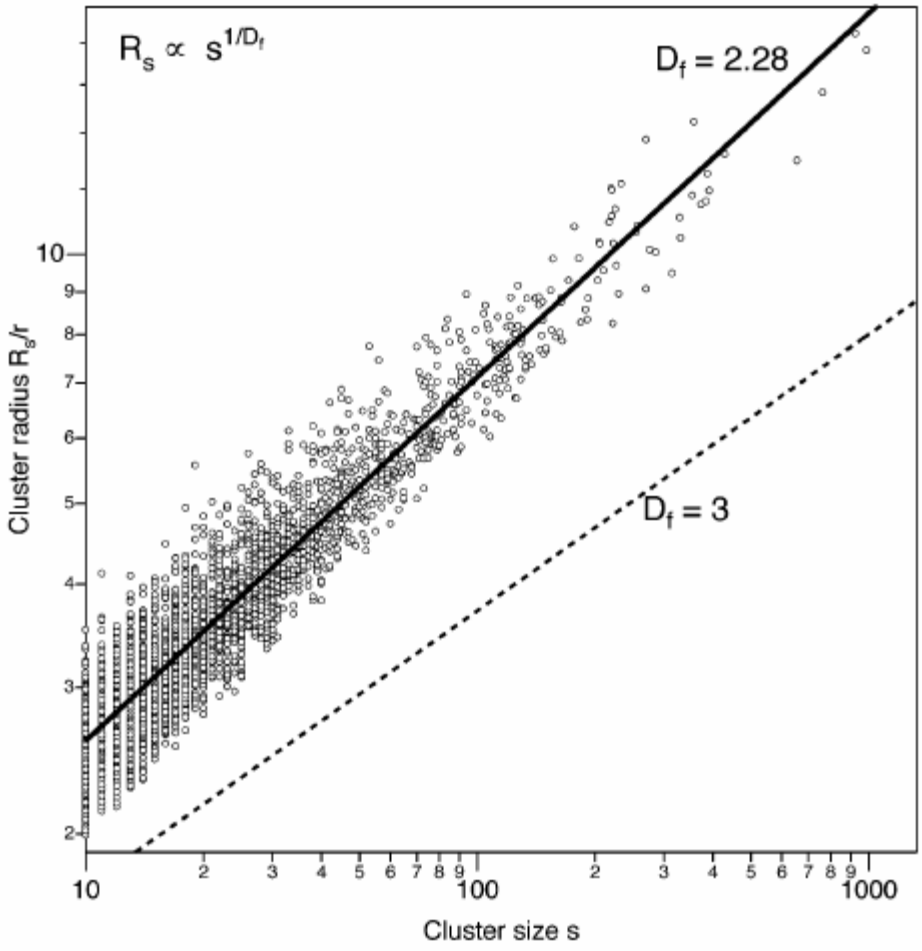

Figure 7. Dependence of cluster radius R_s on cluster size s for a simulated film of porosity $P = 0.775$ and $l = 200$. The solid line is a fit to eq 7. The dashed line shows eq 7 for $D_f = 3$.

The cluster size refers to the number of particles in a cluster. Percolation theory predicts that R_s scales with s according to the relation[39]

$$R_s \propto s^{1/D_f} \qquad (7)$$

$D_f = 3$ for 3D network with no fractal characteristics

Benkstein et al., JPCB 107:7759-7767, 2003.

Thermal contact resistance

molecular formulation

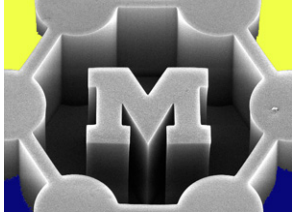

Relate interatomic potential to thermal contact resistance

k = thermal conductivity

k* = nondimensional thermal conductivity

k_{char} = characteristic thermal conductivity

d = separation distance

$$k^* = \frac{k}{k_{char}} \qquad k_{char} = \frac{k_b}{\sigma^2}\sqrt{\frac{\varepsilon}{m}}$$

$$\frac{R_c}{A} = \frac{d}{k} = \frac{d}{k_{char}k^*} = \frac{d\sigma^2}{k_{char}k_b}\sqrt{\frac{m}{\varepsilon}} \rightarrow R = \left[\frac{\sigma^2}{{\sigma_o}^2}\sqrt{\frac{\varepsilon_o}{\varepsilon}}\right]R_o$$

→Now we can generalize results from a molecular dynamics simulation to a continuum finite difference model, with varying separation and LJ parameters

Zhong and Lukes, *Phys Rev B* 74:125403, 2006.

CNT-CNT contact resistance

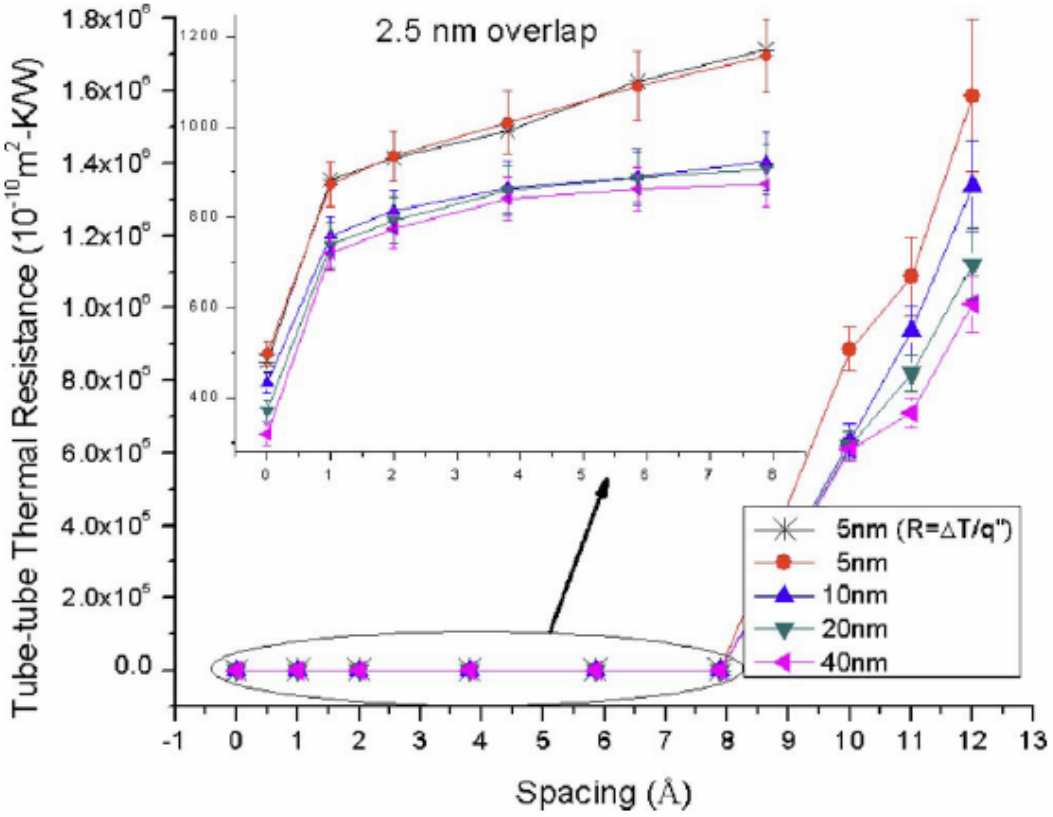

FIG. 5. (Color online) Tube-tube thermal resistance vs spacing and length for 5, 10, 20, and 40 nm nanotubes with 2.5 nm overlap. Asterisks are from steady-state MD simulations for 5 nm tubes; filled symbols are from finite difference fit to transient MD simulations. A four order of magnitude decrease in R is found as nanotube spacing decreases.

Loss of contact gives significant resistance increase

Zhong and Lukes, *Phys Rev B* 74:125403, 2006.

Effect of contact length

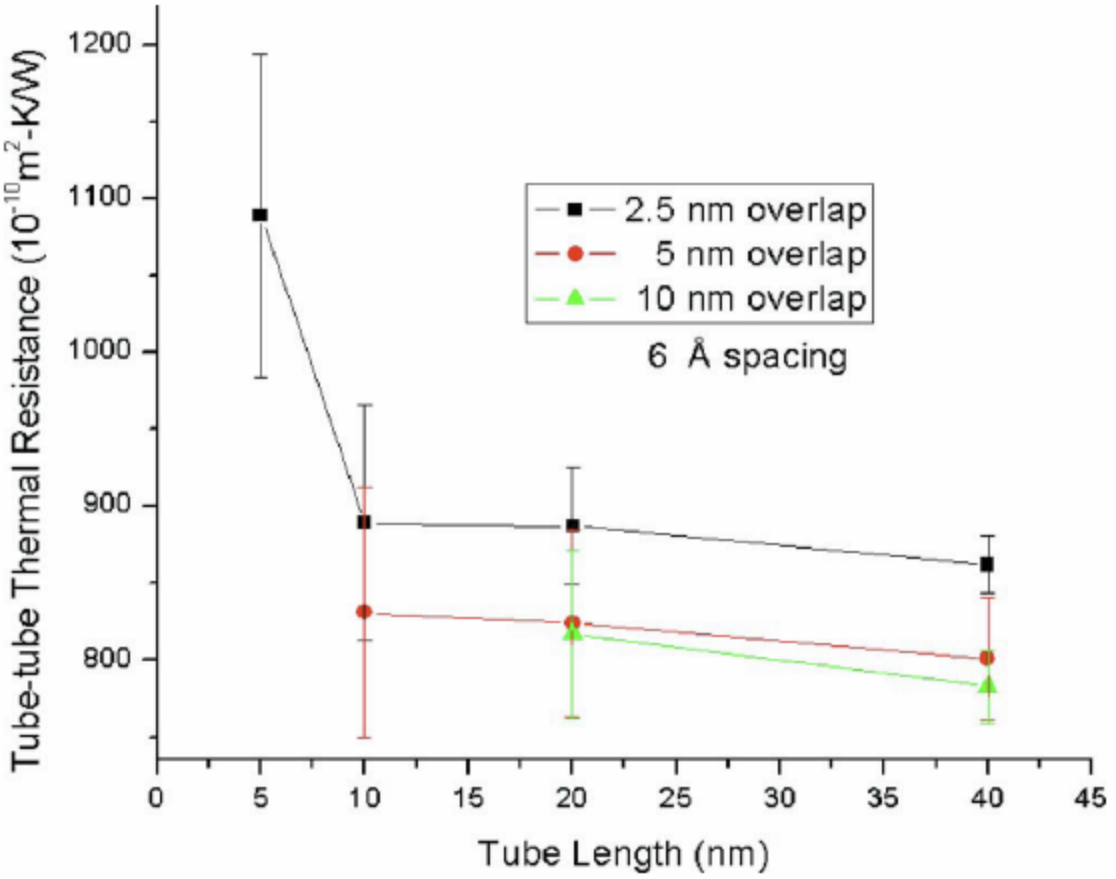

FIG. 7. (Color online) Tube-tube thermal resistance vs tube length for 5, 10, 20, and 40 nm tubes with 2.5 nm overlap and 6 Å spacing. Resistance decreases as tube length increases.

Zhong and Lukes, *Phys Rev B* 74:125403, 2006.

Thermal contact resistance dominates over CNT thermal resistance

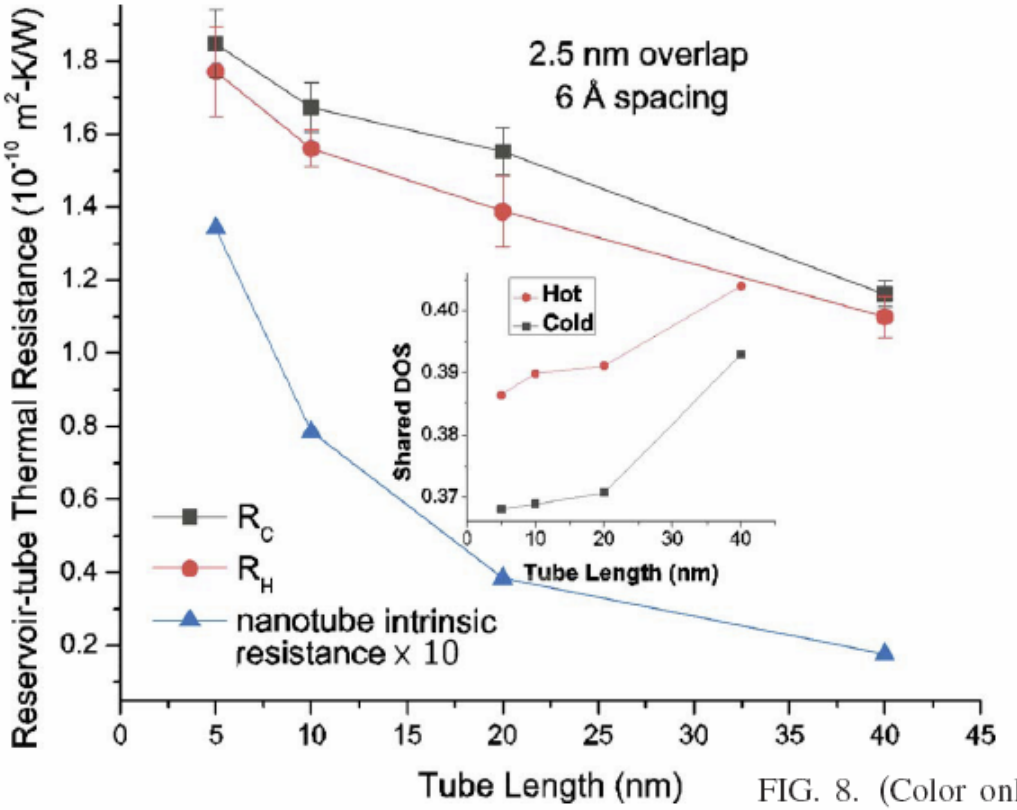

FIG. 8. (Color online) Hot reservoir-tube, cold reservoir-tube, and nanotube intrinsic thermal resistances vs tube length for 5, 10, 20, and 40 nm tubes with 2.5 nm overlap and 6 Å spacing. Nanotube intrinsic resistance is multiplied by ten for plotting purposes. Shared density of states is in arbitrary units. Resistances decrease as tube length increases. The cold reservoir-tube resistance is higher than the hot reservoir-tube resistance; the shared density of states is higher at the hot end. Reservoir-tube resistances are higher than intrinsic resistance.

Zhong and Lukes, *Phys Rev B* 74:125403, 2006.

Beyond contact: near-field heat transfer (between NPs)

Fluctuating dipoles transfer heat by electromagnetic radiation and induce vibrations

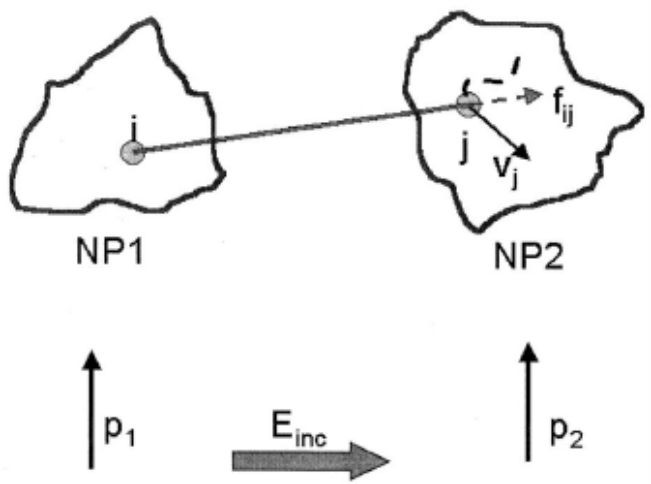

FIG. 2. Explanation schemes of the calculation of the power dissipated in the NP2 due to the field emitted by the NP1. In the MD computation (above), the power is computed as the work produced by the atomic motions of the NP2 atoms in the potential field generated by the NP1. In the electrostatic calculation (below), each NP is assimilated to one dipole (vectors $\mathbf{p}_1$ and $\mathbf{p}_2$) situated at the NP centers.

Compare to macroscopic #s

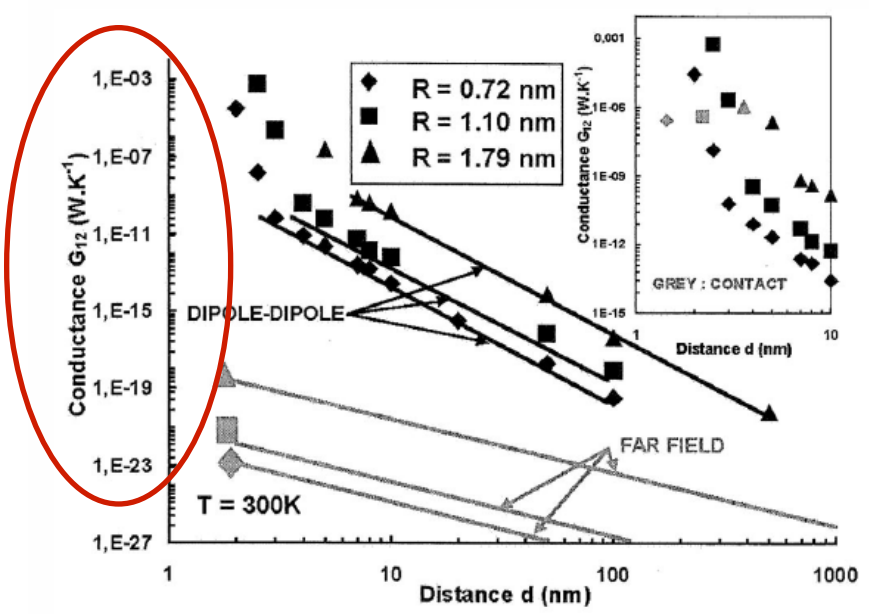

FIG. 3. Thermal conductance G_{12} vs distance d between the centers of mass. R corresponds to the nanoparticle radius and N is the number of atoms in each particle. While the MD (data points) and the analytical (thick lines) predictions agree very well when the interparticle distance is larger than the nanoparticle diameter, a deviation appears when $d < 4R$. The far-field conductance due to emission and absorption is reported for comparison. The inset highlights the conductance values when the NPs are in contact (gray data points). Their abscissa correspond to $2R$. The contact conductance is 2 to 3 orders of magnitude lower than the conductance just before contact.

→ **Nanofluids**

Domingues et al., *Phys Rev Lett* 94:085901, 2005.

Mechanical network model

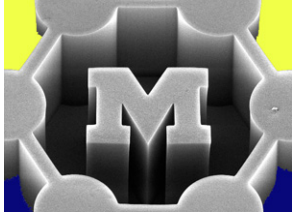

Segment length decreases as network "density" increases

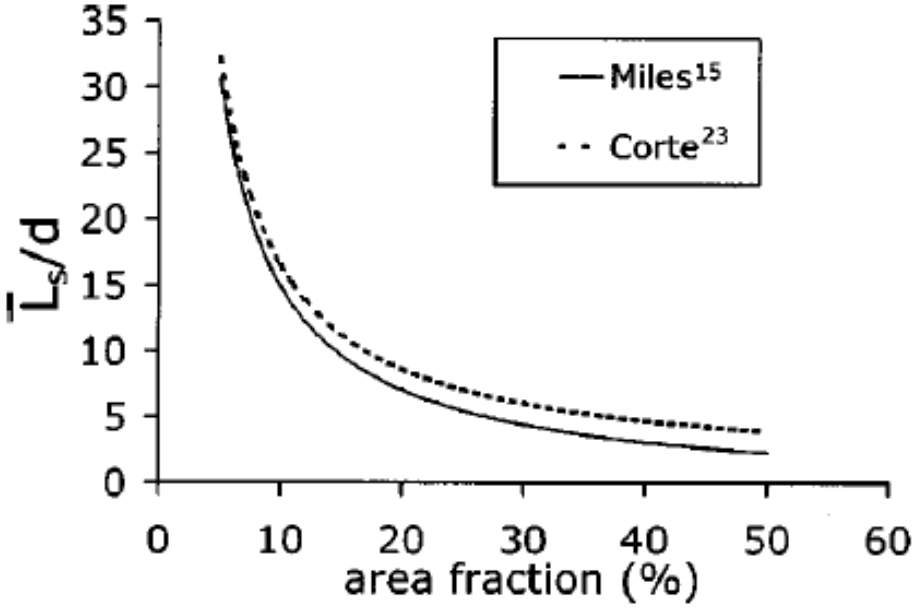

Shell models should be used at smaller aspect ratios

"Waviness" affects interconnect density

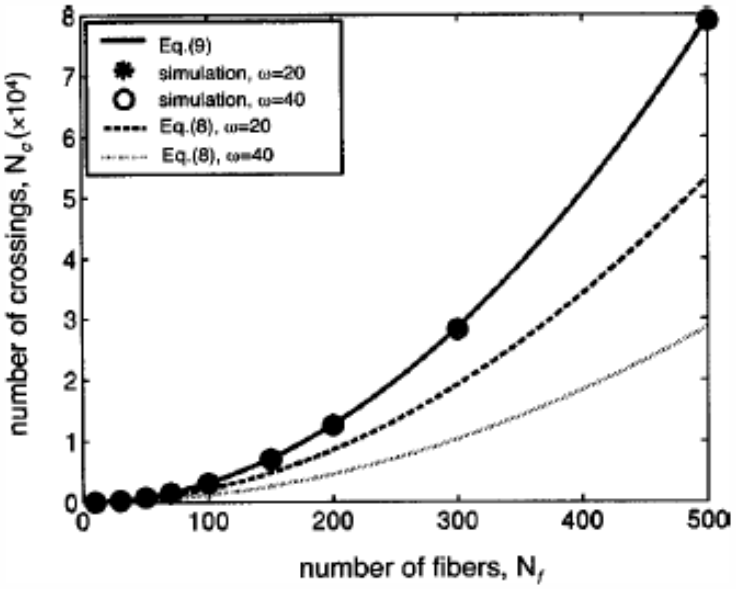

FIG. 6. Simulations, and present and prior analytical results for the number of fiber crossings vs number of fibers, for systems of varying fiber waviness.

$$y = a\sin(\omega x)$$

Berhan et al., *J. App. Phys.* 95(8):4335, 2004.

Mechanical stiffness of CNT mats

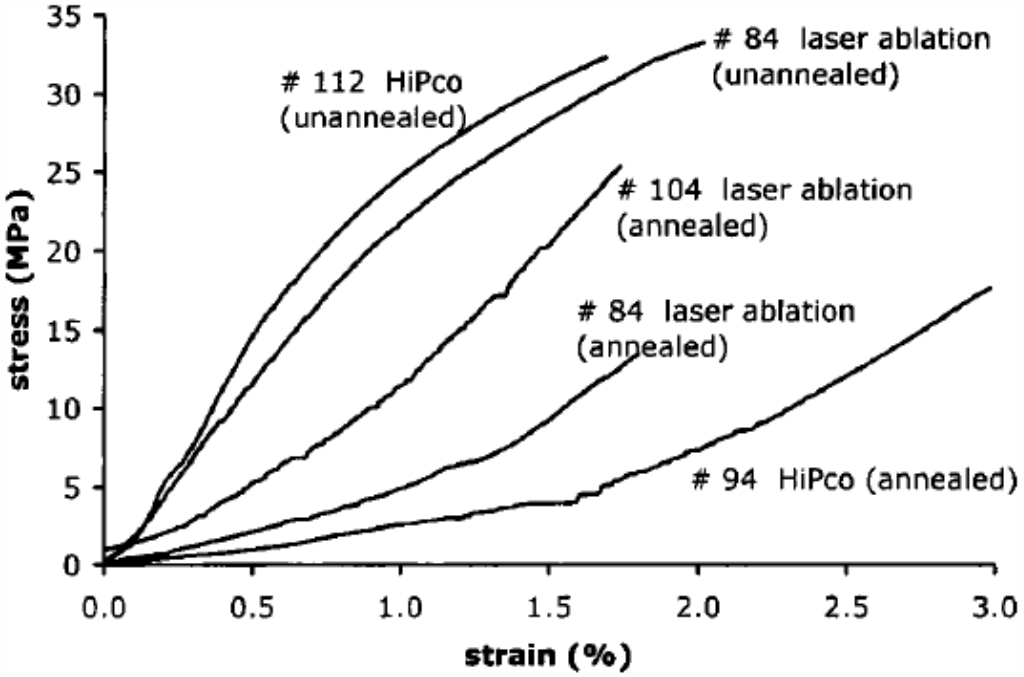

FIG. 12. Stress vs strain results of mechanical tests on nanotube sheet samples.

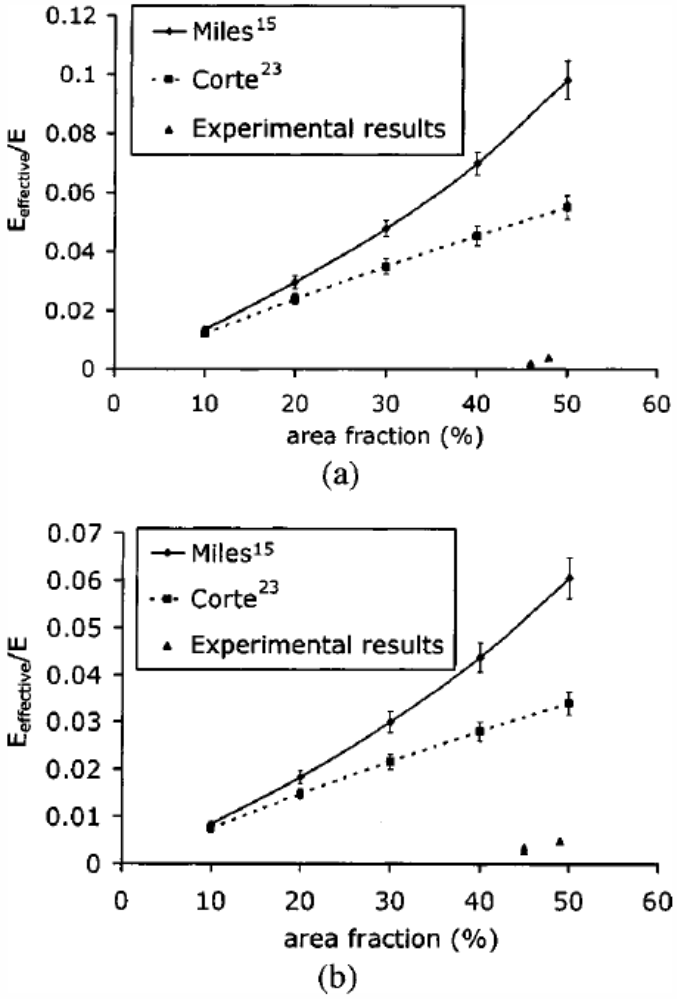

FIG. 13. Comparison of experimental and simulation results for normalized effective modulus, for nanotube sheets containing nanotubes synthesized by the (a) HiPco and (b) laser ablation processes. Simulation results derived using both Miles (see Ref. 15) and Corte (see Ref. 23) are shown. An average rope diameter 10 nm was assumed in all cases.

→ Add polymer to stiffen/ strengthen

Berhan et al., *J. App. Phys.* 95(8):4335, 2004.

3D covalently-bonded networks

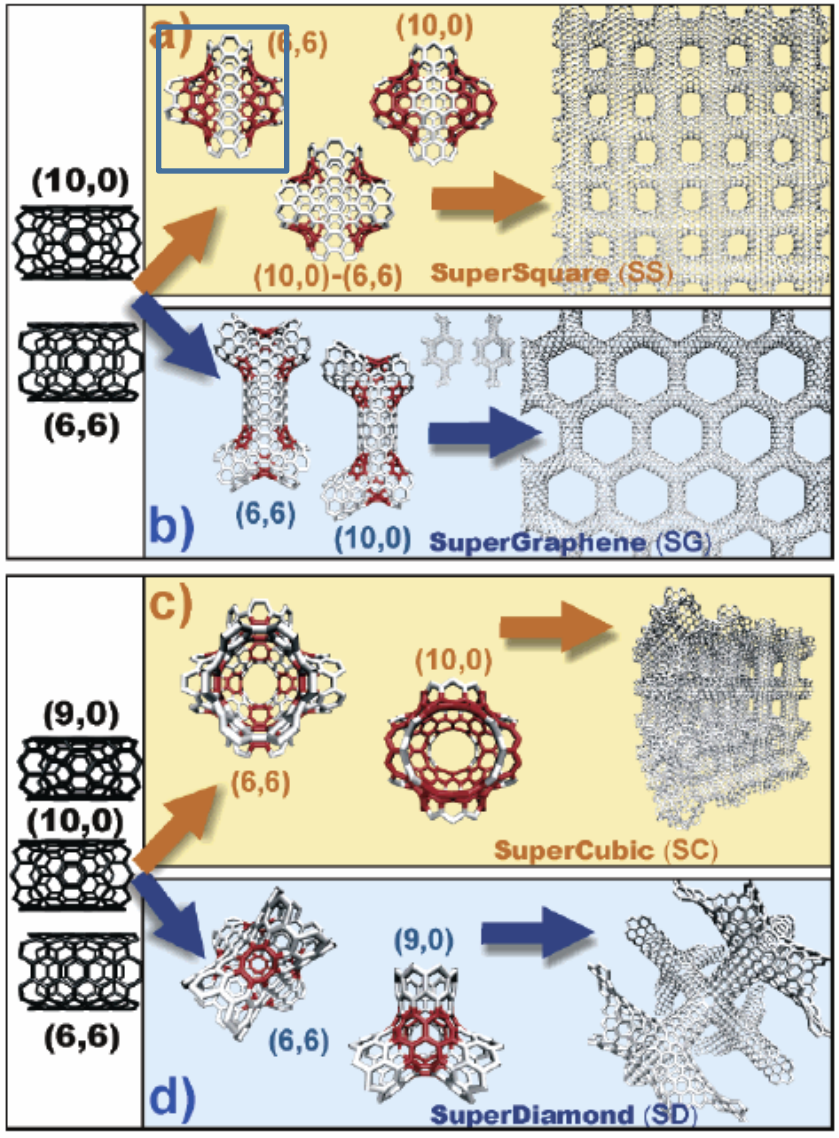

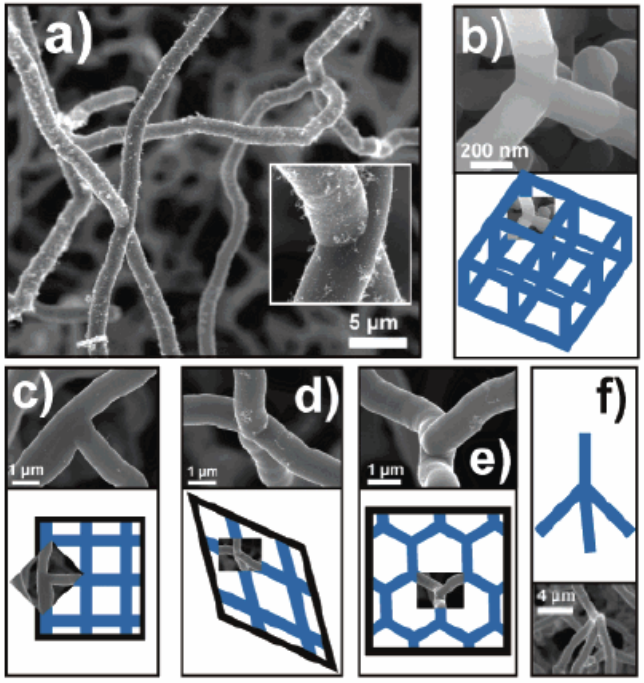

Figure 2. SEM images showing covalent carbon junctions of 1D blocks, illustrating branching geometries obtained experimentally with the geometry necessary for complex networks. (Even when the 1D blocks are thicker than CNTs, they show evidence of specific branching geometries as a starting point to the theoretical design of models.) The material was produced using a CVD approach involving the thermolysis of nickelocene ($NiCp_2$) powder in conjunction with thiophene (C_4H_4S) in an argon atmosphere at 1000 °C.[30] From these images, we observe that the junctions are covalently connected in a variety of stable ways, such as (b) a junction with the geometry of 3D cubic network node, (c and d) a T-junction and a cross-junction, with the correct geometry needed in a 2D square network, (e) a 3-terminal junction with the necessary angles in a 2D hexagonal network, and (f) a 4-terminal junction with a tetrahedral-like architecture.

Romo-Herrera et al., Nano Letters 7(3):570-576, 2007.

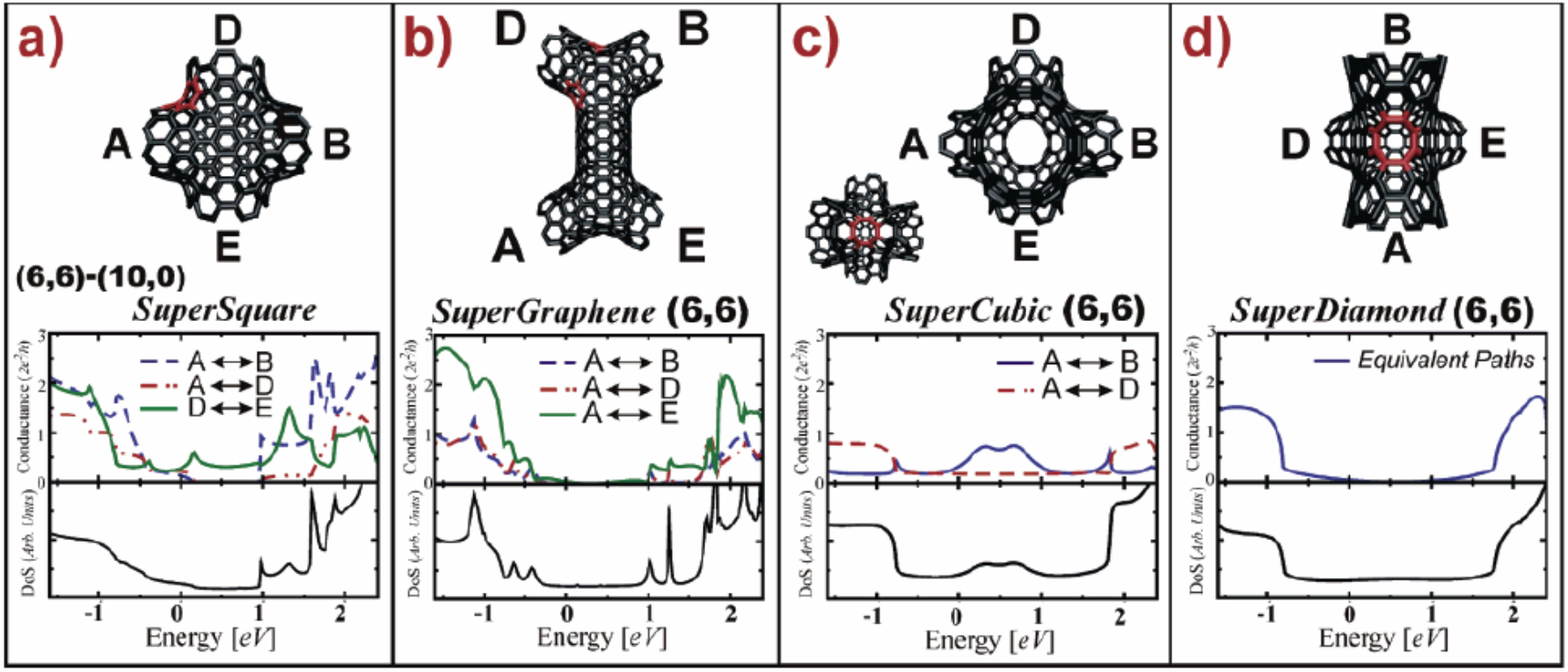

Figure 3. Electronic properties of four different network building units. The architecture plays a determinant role in dictating the DOS spectra and conductance properties. Preferred conductance paths are observed to cross the node. In each panel is shown the geometry, inequivalent defects (red sites), and terminal labels; conductance spectra for the inequivalent electronic paths through terminals; and electronic DOS for each node presented, based on extended tight-binding Hamiltonian. In part a, the SS block presents only one conducting path along the armchair channel. The SG block presented in part b shows how, even without a band gap in the DOS spectra, the architecture restricts to zero conductance around the Fermi energy. Part c reveals an increase in conductance for the A ↔ B electronic path around the Fermi level, making it the most favorable one to cross this SC block. Finally, part d presents the SD bock, which presents zero conductance for all of its equivalent paths, even with the existence of states in the DOS spectra.

Romo-Herrera et al., Nano Letters 7(3):570-576, 2007.

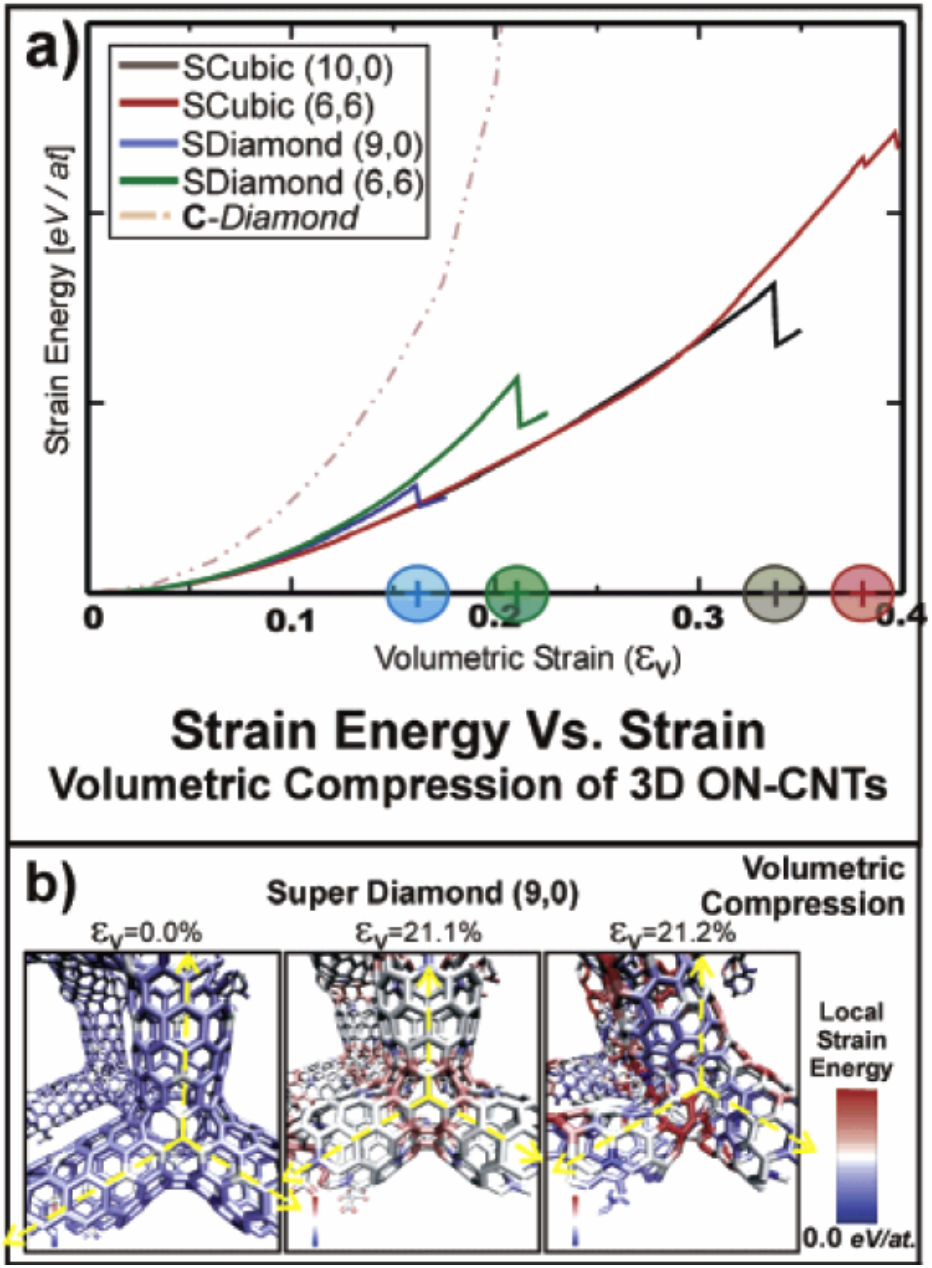

Romo-Herrera et al., Nano Letters 7(3):570-576, 2007.

Videos

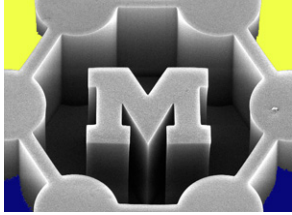

http://pubs.acs.org/subscribe/journals/nalefd/suppinfo/nl0622202/nl0622202si20060920_063532.mpg

http://pubs.acs.org/subscribe/journals/nalefd/suppinfo/nl0622202/nl0622202si20060920_065202.mpg

Joints dominate flexibility

Romo-Herrera et al., Nano Letters 7(3):570-576, 2007.

Interfacial toughening using a monolayer

Interconnect structure
tested in 4-point bending

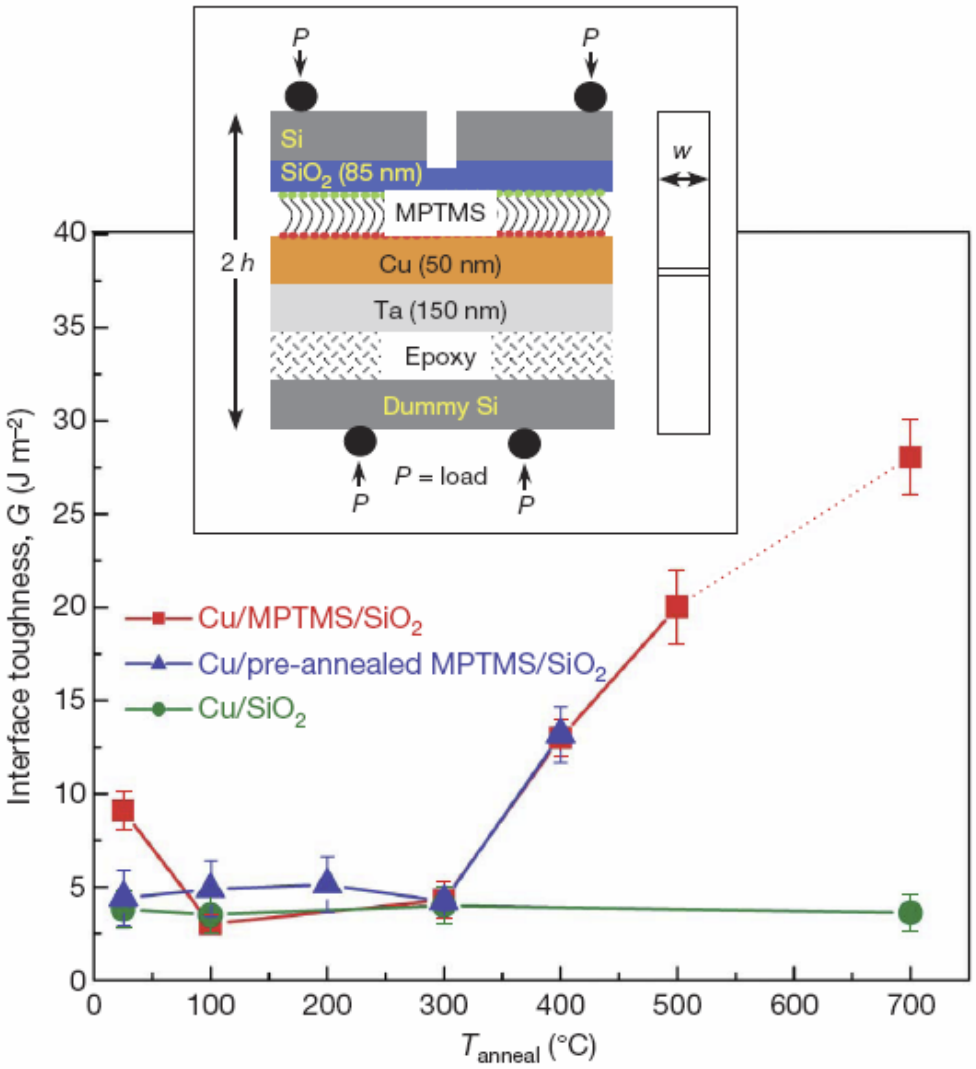

Quick calculation based on bond breakage confirms measured result

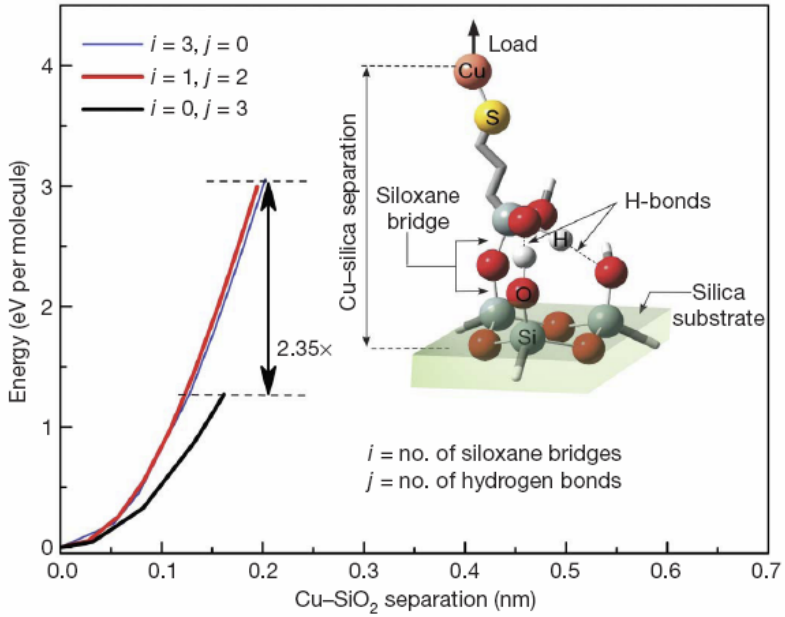

Figure 4 | Calculated system energy as a function of molecular stretching for different combinations of siloxane and hydrogen bonds at the MPTMS/SiO_2 interface. System energy was determined by first-principles density functional theory calculations. Inset, schematic depiction of an MPTMS molecule bonded to the silica underlayer by one siloxane bridge ($i = 1$, 33% irreversible dehydration) and two hydrogen bonds ($j = 2$). The arrow indicates the direction of stretching. The graph shows system energy plotted as a function of Cu overlayer/SiO_2 underlayer separation for three different interface bonding chemistries; each curve is plotted up to the fracture point.

Gandhi et al., *Nature* 447:299 2007.

XPS reveals Cu-S still bonded post-fracture

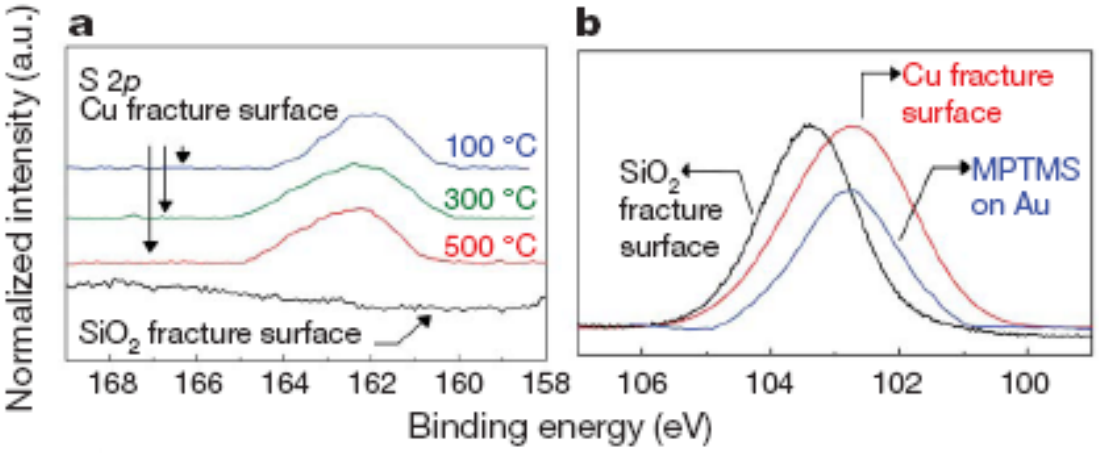

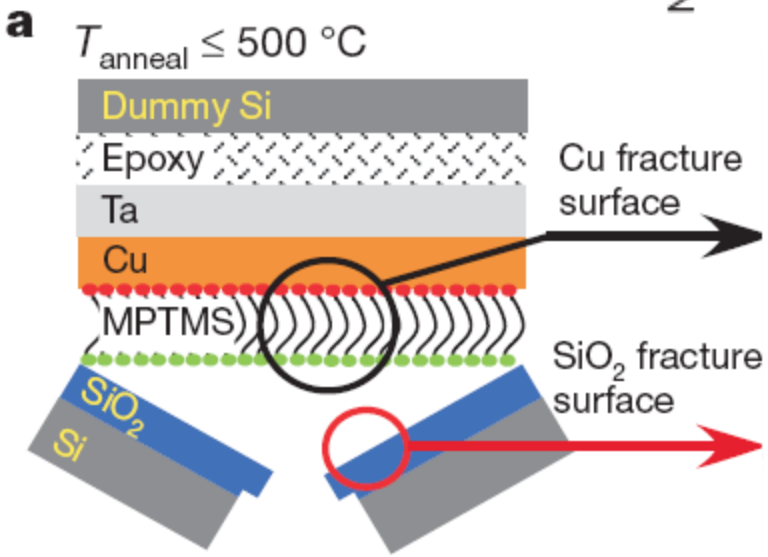

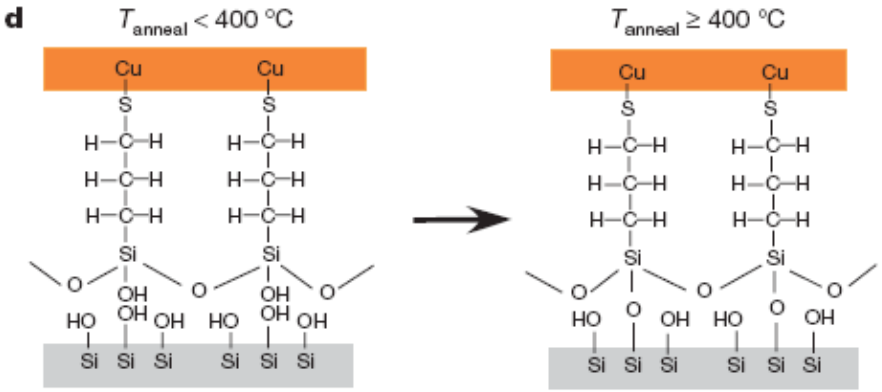

Figure 3 | High-resolution core-level spectra from fracture surfaces, and a schematic illustration of the primary toughening mechanism. **a**, S 2*p* bands from Cu fracture surfaces of samples for $T_{anneal} \leq 500$ °C, shown with a reference spectrum from the silica fracture surface. **b**, Si 2*p* bands from Cu and silica fracture surfaces, respectively, shown with a reference spectrum from an MPTMS MNL on Au. **c**, S 2*p* intensity, normalized to the Cu 2*p* peak, plotted as a function of T_{anneal}. Data points, mean from four data sets; error bars, ±s.d. **d**, Schematic illustration of the temperature-assisted interfacial toughening mechanism. See text for details.

Annealing creates Si-O bonds (strong)

Cu layer prevents detachment

Gandhi et al., *Nature* 447:299 2007.

Welding CNT-metal junctions

- Metal-filled CNTs made by floating catalyst method
- Focused electron beam gives 10^3-10^5 A/cm^2
- 11 minutes to form junction shown below

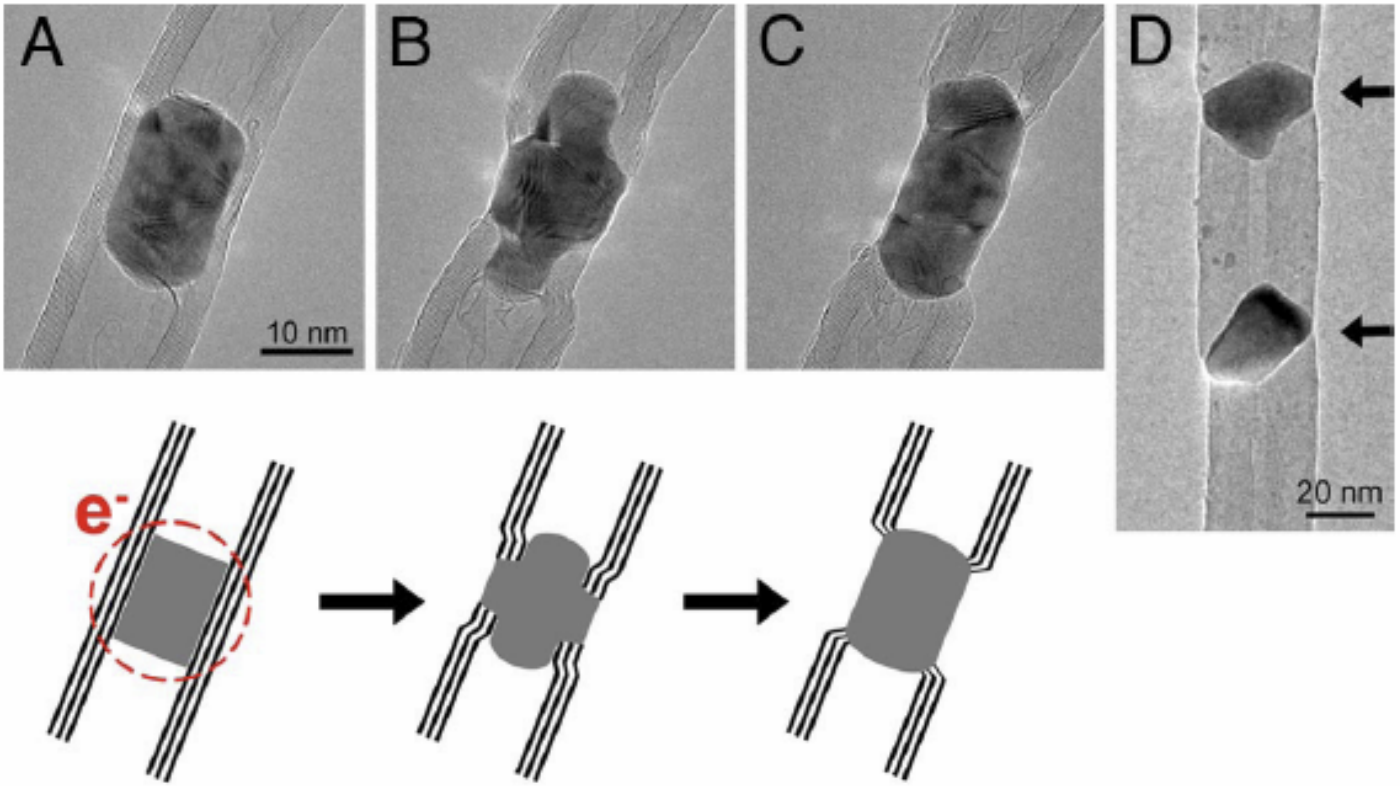

Fig. 1. Formation of a MWNT–Co–MWNT junction from a Co-filled MWNT subjected to electron irradiation (200 keV) at 700 °C. (*A*) The Co-filled MWNT at the beginning of the experiment. (*B*) The focused electron beam damages the tube, and the Co nanowire is expelled to the surface, experiencing shape changes after 6 min of irradiation. (*C*) Finally, the Co particle acts as a link between the 2 MWNT segments. The time required to obtain the final shape was 11 min. The sketch at the bottom shows the mechanism of the process. The circle indicates the zone subjected to electron irradiation. (*D*) Periodic FeCo–MWNT heterojunction, formed by repeated irradiation at different positions of a FeCo-filled nanotube. Arrows indicate metal particles.

Rodriguez-Manzo et al., *PNAS* (early edition) 2009.

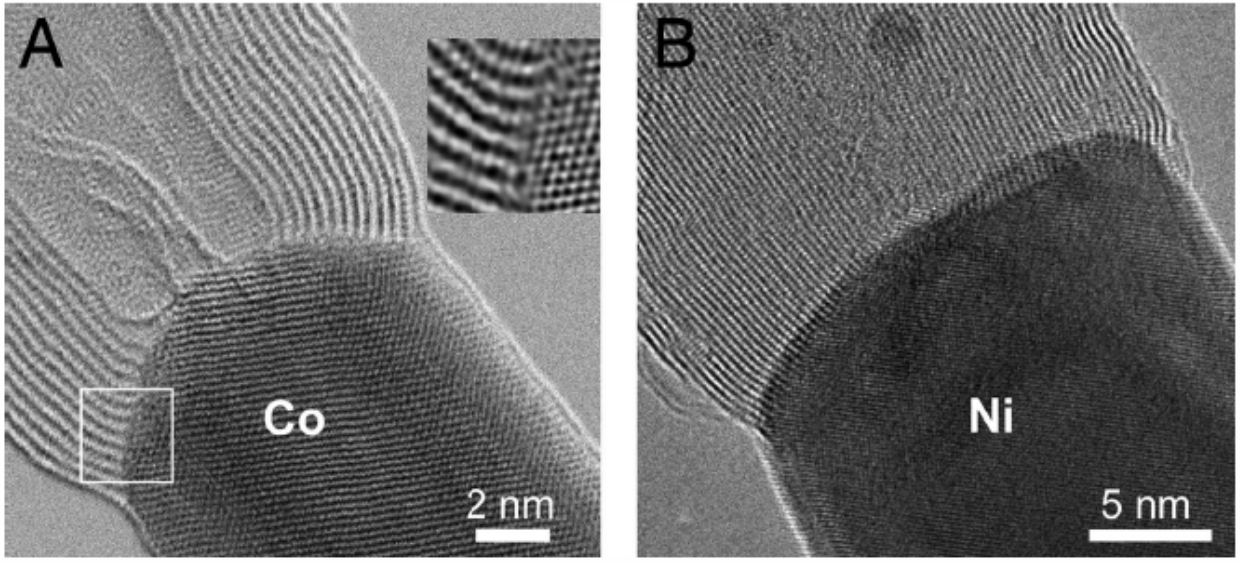

Fig. 2. High-resolution images from metal–MWNT junctions. (*A*) Bright-field STEM image (C_s-corrected) of a MWNT–Co interface. The Co particle has an fcc structure (the image shows an alignment close to the [110] zone axis projection of the Co fcc lattice). Strain is introduced at the interface as can be seen by the local bending of the graphitic layers at the interface. The *Inset* shows a detail of the interface (white square) after noise filtering, where the bending of the nanotube layers to match the metal lattice is visible. (*B*) HRTEM image of a MWNT–Ni interface. The Ni particle has an fcc structure.

Rodriguez-Manzo et al., *PNAS* (early edition) 2009.

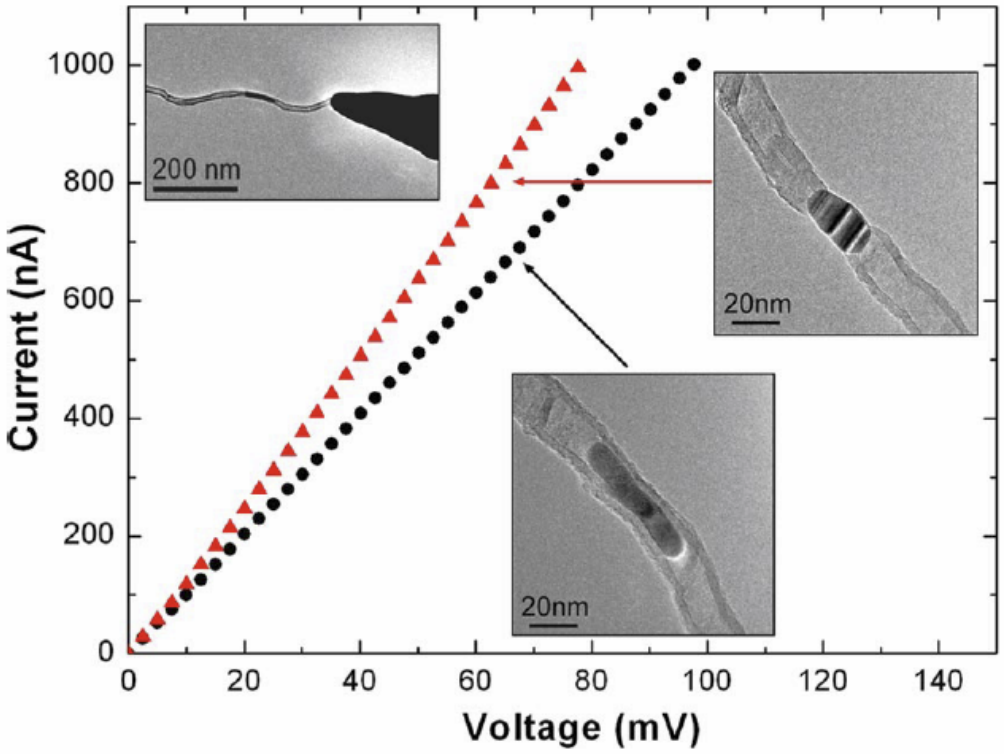

Fig. 3. Representative I–V curves taken from a Co-filled MWNT (black dots) and from the same tube subjected to e-beam irradiation and with a MWNT–Co–MWNT joint (red triangles) measured by using the STM-TEM ''Nanofactory'' setup. The current range was limited $<1\ \mu$A to avoid overheating of the structure. The *Insets* display the corresponding TEM images. (*Upper Left*) A Co-filled MWNT attached to a gold wire (biased far to the left) connected to the Au STM tip inside the electron microscope. ((*Lower Center*) the appearance of the starting nanotube in the ''filled'' state. (*Upper Right*) The same tube after biasing (to induce Joule heating) and irradiation resulted in the Co-joint formation.

Rodriguez-Manzo et al., *PNAS* (early edition) 2009.